2005

Arc-discharge In Solution: A Novel Synthesis Method For Carbon Nanotubes And In Situ Decoration Of Carbon Nanotubes With Nanoparticles

Debasis Bera
University of Central Florida

STARS Citation

Bera, Debasis, "Arc-discharge In Solution: A Novel Synthesis Method For Carbon Nanotubes And In Situ Decoration Of Carbon Nanotubes With Nanoparticles" (2005). *Electronic Theses and Dissertations, 2004-2019*. 282.
https://stars.library.ucf.edu/etd/282

ARC-DISCHARGE IN SOLUTION: A NOVEL SYNTHESIS METHOD FOR CARBON NANOTUBES AND IN SITU DECORATION OF CARBON NANOTUBES WITH NANOPARTICLES

by

DEBASIS BERA

M.Tech. Indian Institute of Technology Bombay; India, 2002
M.Sc. Jadavpur University; Calcutta, India, 1999
B.Sc. (Honors) Vidyasagar University; Medinipur, India, 1995

A dissertation submitted in partial fulfillment of the requirements
for the degree of Doctor of Philosophy
in the department of Mechanical, Materials and Aerospace Engineering
in the College of Engineering and Computer Science
at the University of Central Florida
Orlando, Florida

Spring Term
2005

Major Professor: Sudipta Seal

ABSTRACT

Nanotechnology has reached the status of the 21st century's leading science and technology based on fundamental and applied research during the last two decades. An important feature of nanotechnology is to bridge the crucial dimensional gap between the atomic and molecular fundamental sciences and microstructural scale of engineering. Accordingly, it is very important to have an in-depth understanding of the synthesis of nanomaterials for the use of state-of-the-art high technological devices with enhanced properties. Recently, the 'bottom-up' approach for the fabrication of nanomaterials has received a great deal of attention for its simplicity and cost effectiveness. Tailoring the various parameters during synthesis of selected nanoparticles can be used to fabricate technologically important components.

During the last decade, carbon nanotubes (CNTs) have been envisioned for a host of different new applications. Although carbon nanotubes can be synthesized using a variety of techniques, large-scale synthesis is still a great challenge to the researchers. Three methods are commonly used for commercial and bulk productions of carbon nanotubes: arc-discharge, chemical vapor deposition and laser ablation. However, low-cost, large-scale production of high-quality carbon nanotubes is yet to be reported. One of the objectives of the present research is to develop a simplified

synthesis method for the production of large-scale, low-cost carbon nanotubes with functionality.

Herein, a unique, simple, inexpensive and one-step synthesis route of CNTs and CNTs decorated with nanoparticles is reported. The method is simple arc-discharge in solution (ADS). For this new method, a full-fledged optoelectronically controlled instrumen is reported here to achieve high efficiency and continuous bulk production of CNTs. In this system, a constant gap between the two electrodes is maintained using a photosensor which allows a continuous synthesis of the carbon nanostructures. The system operates in a feedback loop consisting of an electrode-gap detector and an analogue electronic unit, as controller. This computerized feed system was also used in single process step to produce in situ-decorated CNTs with a variety of industrially important nanoparticles. To name a few, we have successfully synthesized CNTs decorated with 3-4 nm ceria, silica and palladium nanoparticles for many industrially relevant applications. This process can be extended to synthesize decorated CNTs with other oxide and metallic nanoparticles.

Sixty experimental runs were carried out for parametric analysis varying process parameters including voltage, current and precursors. The amount of yield with time, rate of erosion of the anode, and rate of deposition of carbonaceous materials on the cathode electrode were investigated. Normalized kinetic parameters were evaluated for different amperes from the sets of runs. The production rate of pristine CNT at 75 A is as high as 5.89 ± 0.28 $g.min^{-1}$.

In this study, major emphasis was given on the characterizations of CNTs with and without nanoparticles using various techniques for surface and bulk analysis of the

nanostructures. The nanostructures were characterized using transmission electron microscopy, high resolution transmission electron microscopy, scanning transmission electron microscopy, energy dispersive spectroscopy and scanning electron microscopy, x-ray photo electron spectroscopy, x-ray diffraction studies, and surface area analysis.

Electron microscopy investigations show that the CNTs, collected from the water and solutions, are highly pure except the presence of some amorphous carbon. Thermogravimetric analysis and chemical oxidation data of CNTs show the good agreement with electron microscopy analysis. The surface area analysis depicts very high surface area. For pristine multi-walled carbon nanotubes, the BET surface area is approximately 80 $m^2.g^{-1}$. X-ray diffraction studies on carbon nanotubes shows that the products are clean.

Nano-sized palladium decorated carbon nanotubes are supposed to be very efficient for hydrogen storage. The synthesis for in-situ decoration of palladium nanoparticles on carbon nanotubes using the arc discharge in solution process has been extensively carried out for possible hydrogen storage applications and electronic device fabrication. Palladium nanoparticles were found to form during the reduction of palladium tetra-chloro-square planar complex. The formation of such a complex was investigated using ultraviolet-visible spectroscopic method. Pd-nanoparticles were simultaneously decorated on carbon nanotubes during the rolling of graphene sheets in the arc-discharge process. Zero-loss energy filtered transmission electron microscopy and scanning transmission electron microscopy confirm the presence of 3 nm palladium nanoparticles. The deconvoluted X-ray photoelectron spectroscopy envelope shows the

presence of palladium. Surface area measurements using BET method show a surface area of 28 $m^2.g^{-1}$. The discrepancy with pristine CNTs can be explained considering the density of palladium (12023 $kg.m^{-3}$). Energy dispersive spectroscopy suggests no functionalization of chlorine to the sidewall of carbon nanotubes. The presence of dislodged graphene sheets with wavy morphology as observed with high-resolution transmission electron microscopy supports the formation of CNTs through the ‘scroll mechanism’.

Dedicated to my Parents

ACKNOWLEDGMENTS

I would like to acknowledge the support of my entire committee members who have contributed to my research drawing on their unique individual talents. I would like to thank specially Professor H. Heinrich, Advanced Materials Processing and Analysis Center (AMPAC) and Department of Physics, for his generous support on transmission electron microscopy investigations.

I am extremely grateful to my lab-mate for their untiring support with characterization techniques, including the use and training on equipments which greatly helped to improve the quality of my work. I, especially, would like to thank Matthew, Greg and Erik who voluntarily extended their helping hands to me whenever needed. I am thankful to Dr. S.C. Kuiry for his constant support, taking pain going through and correcting the manuscripts for journal papers.

This work was made possible through the financial support of NSF-REU project and Pacific Northwest National Laboratory (PNNL) for the fellowship of Summer Research Institute. I would like to acknowledge Dr. D. R. Baer, Dr. S. Thevuthasan and scientists of PNNL for their supports, valuable helps and encouragements. I would like to thank engineers of Materials Characterization Facility (MCF), AMPAC, for equipment support.

I am highly indebted to my parents, brother and sister for their constant moral supports and encouragements.

At last, but certainly not least, I wish to express my deep sense of gratitude to my advisor Professor S. Seal for his constant encouragement and invaluable guidance throughout the course of this investigation. It has been a pleasure being associated with him. His endless support, patience and persistence made me complete this dissertation.

TABLE OF CONTENTS

LIST OF FIGURES

LIST OF TABLES

LIST OF ABBREVIATIONS

ADS:	Arc-discharge in Solution
AFM:	Atomic Force Microscope
BET:	Brunauer Emmett Teller
CNTs:	Carbon Nanotubes
CVD:	Chemical Vapor Deposition
DC:	Direct Current
DFT:	Density Functional Theory
EDS:	Energy Dispersive Spectroscopy
FIB:	Focused Ion Beam
GNF:	Graphite Nanofiber
HRTEM:	High Resolution Transmission Electron Spectroscopy
LED:	Light Emitting Diode
MD:	Molecular Dynamics
MEMS:	Microelectromechanical System
MWCNTs:	Multi-walled Carbon Nanotubes
NEMS:	Nanoelectromechnaical System
NPC:	Nanoporous Carbon
PECVD:	Plasma Assisted Chemical Vapor Deposition

PVD: Physical Vapor Deposition

SAED: Selected Area Electron Diffraction

STEM: Scanning Transmission Electron Spectroscopy

STM: Scanning Tunneling Microscope

SWCNTs: Single-walled Carbon Nanotubes

TEM: Transmission Electron Microscopy

UV VIS: Ultraviolet Visible

XPS: X-ray Photoelectron Spectroscopy

XRD: X-ray Diffraction

CHAPTER 1: INTRODUCTION

The manifestation of quantum phenomena in the electron transport of metallic nanowires and anomalous magnetic properties of nanoparticles of transition metals due to spin-polarized transport are a few examples of the unusual behavior of metals at the nanometer dimension compared to their bulk counterparts. Such unusual properties have aroused a great deal of interest in nanostructured materials for potential applications[1-5] in biomedical sciences, electronics, optics, magnetism, and energy storage. In addition to these physical properties, nanostructured materials exhibit a broad range of fascinating anomalous mechanical properties[5-15], such as:

1. Lower observed elastic modulus than materials with conventional grain size,
2. Ultrahigh hardness values for nanostructured pure metals (~10 *nm* grain size) they are 2 to 7 times higher than those of larger grained (>1 μm) metals,
3. A negative *Hall-Petch* slope, i.e., decreasing hardness with decreasing grain size for materials with nano-scale grain size,
4. Superplastic behavior at low homologous temperatures in brittle ceramics or intermetallics with nano-scale grain sizes, due to diffusional deformation mechanisms, and
5. Tensile and compressive strengths with anomalously high values at the nanometer-length scale.

Such examples prove the potential of nano-scale materials to revolutionize new applications unthinkable considering traditional properties of conventional materials.

1.1. Nanotechnology

During the last two decades, the development of nanomaterials and its incorporation into devices led the progress in Materials Science and Engineering to a new dimension of engineering, called nanotechnology. Applying nanotechnology, researchers have engineered the materials at the nanometer-scale to develop devices, such as probes for the manipulation and imaging of nano-scale materials. Sensors, actuators, transistors, memories, logic devices, and other nanoelectronics have been functionalized to fabricate micro-electro mechanical devices (MEMS) and nano-electro mechanical devices (NEMS). Prefix ‘nano’ can be defined as one *nanometer* is equal to 10^{-9} *meters*. Field emission devices for x-ray instruments, flat panel displays and other vacuum nanoelectronic applications, are some examples where nanotechnology has already been introduced. Nanotechnology has become indispensable for applications to produce probes for biological and chemical separation, sensors and their purification, catalysis, energy storage and composites for structural materials, filling materials and coatings.

1.2. Progress in Nanotechnology

The real progress in research and development of nanotechnology has been spurred by the discovery of fullerene in the mid-1980s, although, the impetus to the scientific and technological possibility of coaxing individual atoms and molecular building blocks into technological applications was given in 1959 by Nobel-laureat *Richard Feynman*[17] in his landmark lecture "*There's plenty of room at the bottom*". During the last two decades, a tremendous amount of research efforts has been given for a thorough understanding of the properties of nanomaterials, which is of utmost importance for advanced applications. With advances in understanding and technology, the properties of nanomaterials can be tailored to numerous engineering applications via atomic-level structural control of materials.

1.3. Classification

In general, two approaches are being used to engineer such materials in nanotechnology:

I. Top-down approach: Lithography using ultraviolet (UV), optical and focused ion beam (FIB) for micron-scale design and electron beam for nano-scale design

II. Bottom-up approach: This includes (a) chemical self assembly tailoring synthesis routes and steps for materials like carbon nanotubes (CNTs), (b) biological self assembly of, e.g., DNA or proteins, and (c) mechanical manipulation of atoms using instruments such as atomic force microscope (AFM), scanning tunneling microscopes (STM) and the like.

1.4. Bottom-up Approach

Via the bottom-up approach, the fabrication of nanostructured materials can be achieved by a number of synthesis techniques, such as arc-discharge, inert gas condensation, plasma processing, physical vapor deposition (PVD) and chemical vapor deposition (CVD), electrodeposition, mechanical alloying, rapid solidification, sol-gel, micro-emulsion, spark erosion, and severe plastic deformation. *Fig. 1.1* shows numerous different nanomaterials synthesized by the bottom-up approach using a variety of techniques[18-25]. However, most of the synthesis techniques are limited to laboratory scale. Arc-discharge, CVD, inert gas condensation, mechanical alloying and electrodeposition are only a few methods that are available for commercial use to synthesize nanostructured materials. The arc discharge method is one of the most important procedures, which has been used widely to synthesize carbon nanostructures in bulk quantities.

Carbon nanostructures are perhaps the most important discovery in the twenty first century, which has already spun off the augmentation of the nanotechnology research in a new dimension. A brief discussion on the carbon nanostructures is given in the following chapter. An overview of various carbon nanostructured materials, their chemical structures and bonding, synthesis methods, several important properties and various technological applications related to the present research is presented following.

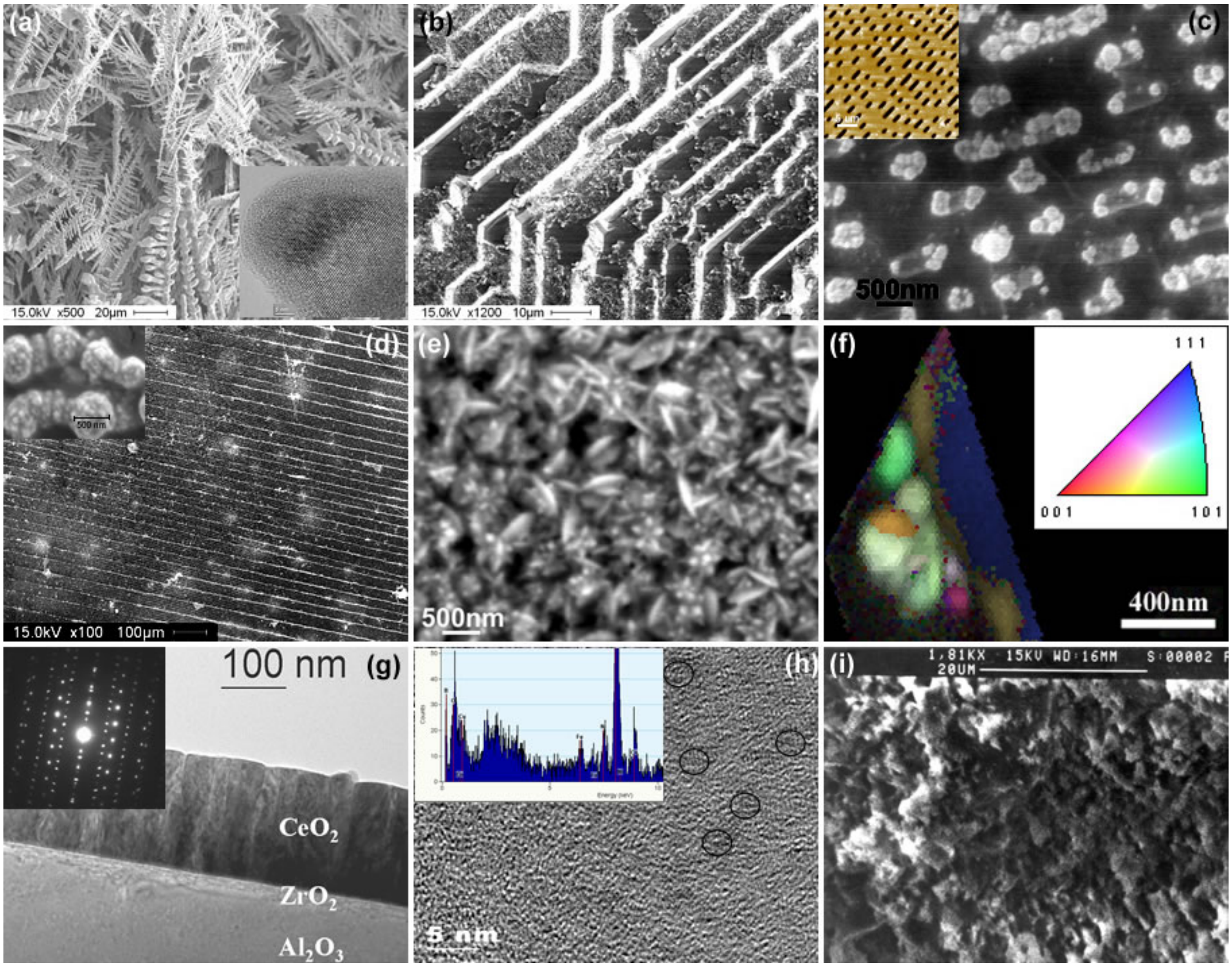

Fig. 1.1: (a) Scanning electron microscopy (SEM) image of as-deposited tin fractals collected from Pt-cathode after anodization[18]*; Inset: high-resolution transmission electron microscopy (HRTEM) image of a 'finger' of tin fractals showing a 3-4nm thick amorphous layer of fluorine doped tin oxide, (b) SEM Micrograph of the morphology of an as-synthesized tin (anode) surface after anodization*[18]*, (c) SEM image of an array of Pd-nanoparticle clusters after electrodeposition on a polymer template*[19]*; inset: atomic force microscopy (AFM) micrograph of the template prior to Pd-deposition, (d) SEM image of a template surface after electrodeposition showing the formation of long arrays of closely spaced Pd-nanoparticles*[20]*; Inset: high-resolution SEM micrograph of a portion of nano-spaced hillocks of Pd-nanoparticles, (e) SEM image of different shaped Pd-nanoparticles on carbon tape template*[21]*, (f) Orientation imaging microscopy (OIM) micrograph of Pd crystallites electrodeposited on a stainless steel template along with the single stereographic triangle*[22]*, (g) HRTEM micrograph of epitaxially grown ceria (111) on top of a zirconia-(111) buffered alumina (0001) substrate through molecular beam epitaxy (MBE); inset: selected area diffraction pattern (SAED) of ceria showing the highly crystalline nature of ceria (111)*[23]*, (h) HRTEM image of 3-4nm particles of Fe-Ni alloy synthesized through microemulsion, inset: energy dispersive spectroscopy (EDS) spectrum of nanoparticles*[24]*, and (i) SEM image of 45S5 Bioglass-polymer composites. The Bioglass was synthesized by the sol-gel method*[25]

CHAPTER 2: LITERATURE SURVEY

As mentioned earlier, a significant amount of research has been devoted on the synthesis, characterization and application of nanomaterials during the last two decades. Since the mid-90's, research on carbon nanostructures has fascinated physicists, chemists and materials scientists alike. In this chapter, the most important areas of research on carbon nanotubes (CNTs), related to the present investigation, are reviewed in detail.

2.1. Carbon Nanostructures

Carbon, (atomic weight=12.0) is one of the most abundant elements in the universe. It has four valence electrons. Carbon can form different structures with entirely different properties using these valence electrons. Until last the decade, two bulk solid phases of carbon were known: graphite and diamond. Graphite, a soft material, is based on sp^2 hybridization of carbon electrons, whereas carbon in isotropically strong diamond has sp^3 hybridization. The structure of fullerenes and carbon nanotubes (CNTs) was discovered in late 90's. These structures are recognized as a different phase from the graphite, even though such structures maintain the architecture of sp^2. *Fig. 2.1* represents the architecture of three different bulk solid phases of carbon. After discovery of fullerene, scientists found a number of different carbon nanostructures with similar architecture as fullerenes. Carbon onions, carbon nanohorns (CNHs), carbon nanorods and CNTs are few of them. These nanostructures can be synthesized by several methods such as: arc-discharge, laser ablation, chemical vapor deposition (CVD) and electrochemical deposition. The manipulation of the process variables, such as electrode materials, catalyst and other experimental parameters including pressure and temperature, leads to a particular shape and the size of the carbon nanostructure. Few of the important carbon nanostructures are discussed in following section.

2.1.1. Fullerene

In 1985, *Kroto*, *Curl, Smalley* and co-workers[26] discovered the fullerene. In general, the structure of the fullerene (C_{60}) is the form of a common soccer ball. The diameter of the fullerene is 0.7 *nm*. This structure is formed with the combinations of 12 pentagonal (five-) and 20 hexagonal (six membered) carbon rings. The bonding is also sp^2, although it is mixed with to an extent of sp^3 character because of its high curvature. The special bonded structures in fullerene molecules have provided several surprises such as metal-insulator transition, unusual magnetic correlation, very rich electronic and optical band structures and properties, and molecular packaging[17]. Because of these properties, fullerenes have been widely exploited for electronic, magnetic, optical, chemical, biological and medical applications.

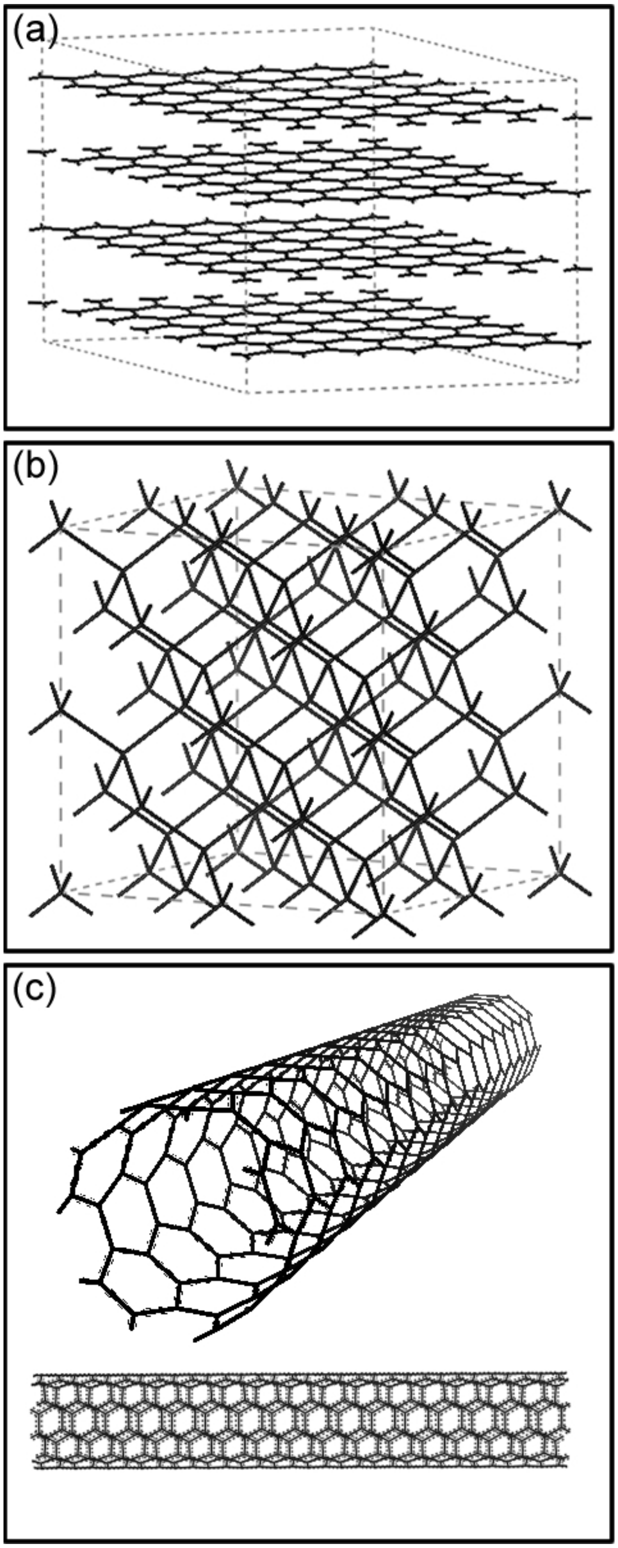

Fig. 2.1: The architecture of three different forms of carbon: (a) graphite, (b) diamond and (c) carbon nanotubes (figures drawn using Material Studio® software)

2.1.2. Carbon Onions

Carbon onions are spherical nanoparticles with C_{60} core surrounded by onion-like nested carbon structures. At 300 *kV*, under electric beam irradiation on nanotubes and nanoparticles in transmission electron microscope (TEM), *Ugarte*[27,28] first found almost perfect spheres apparently made up of concentric fullerenes. These carbon structures are composed of pentagonal, hexagonal and heptagonal (seven membered) carbon rings. The size of carbon onions is as small as 5 *nm* with the core diameter at the range of 7-8 *Å*. Recently, *Sano et al*[29,30] synthesized carbon onions using arc-discharge in water at the potential of 16-17 *V* and 30 *A*. Using an arc-discharge in water process[30], researchers were able to synthesize carbon onions with a large surface area of 984.3 $m^2.g^{-1}$.

2.1.3. Carbon Nanotubes

Carbon nanotubes (CNTs) are seamless cylinders derived from a honey comb lattice representing a single atomic layer or multiple atomic layers of crystalline graphite, called graphene sheets[4]. The nanometer-scale size, and hollow cylindrical shape of carbon nanotubes suggests that they may have many potential applications as molecular sieves, nano-test-tubes, and hydraulic actuators. After the discovery of fullerenes, *Iijima*[31] was fascinated by the *Krätschmer-Huffman* paper[32], and decided to embark[33] on detailed TEM study of the soot produced by their technique. His efforts were rewarded when he found the TEM micrograph of ‘*helical’* structures of CNTs. A detailed description of structures, synthesis aspects, properties and applications is discussed in the following sections.

2.1.4. Carbon Nanohorns

Carbon nanohorns (CNHs) are made of the same graphitic structure as CNTs. The significant characteristic of the CNHs is the formation of an aggregate of approximately 100 nm when many of the nanohorns group together. Such well-graphitized carbon species have free energy of formation so close to that of CNTs that they cannot be used as feedstock in CNT growth. Recently, *Sano et al.*[34] synthesized single walled CNHs by using arc-discharge in liquid method.

2.1.5. Carbon Nanorods

A carbon nanorod is a scrolled graphene sheet without any inner empty core. This solid cylindrical structure is regarded as a derivative of CNTs. The terminologies graphitic carbon fiber (GFCs) and vapor-grown carbon fibers (VGCFs) have been used to denote such solid cylinders.

2.2. Introduction to Carbon Nanotubes (CNTs)

Carbon nanotubes are molecular-scale fibers with structures related to fullerene. In this section, an attempt has been made to survey the brief history of CNTs, the structural overview of CNTs, as well as the most important physical attributes. The first section begins with a brief account of the discovery of CNTs and then a discussion describes the basic characteristics of CNTs.

2.2.1. History

In 1953, *Davis, Slawson* and *Rigby*[35] found a deposition of *an unusual form of carbon* from carbon monoxide at an optimized temperature of 450 º*C* on an iron oxide substrate. Their transmission electron microscopic work could not reveal the architectures of such an unusual form of carbon. In 1960, *Bacon*[36] found the growth of graphite whiskers in direct current (DC) arc under a pressure of 92 *Atm*. of argon at 3900 *K*. He explained the formation of graphite whiskers through a *scroll mechanism*. After few years, carbon filaments with hollow tubes of diameter were reported to be in the range of 2-50 *nm*. *Tibbetts*[37] reported tubular carbon filaments or carbon whiskers which are formed from the decomposition of hydrocarbon at 900 º*C* with submicron catalytic particles. *Speck et al.*[38] tried to correlate the growth mechanism with experimental parameters, but no detailed systematic studies of such nano-sized materials were carried out. Direct stimulus to study such filaments of nanometer dimension came more systematically from the discovery of fullerenes[32]. In 1991, a breakthrough in the research on

CNTs came when *Iijima*[31] reported the arc discharge synthesis and high-resolution electron microscopic characterization of such '*helical microtubules'*.

2.2.2. Structures of CNTs

CNTs have nanometer dimension. They are hollow, cylindrical tubes of graphitic carbon characterized by a single tube wall or a large amount of ordered tube walls. Their length can vary from a few hundred nanometers to several hundred microns. The diameter can be varied from 0.37 *nm* to 100 *nm*. The bonding in the nanotubes is essentially through sp^2 hybridization. The sp^2 hybrid orbital allows carbon atoms to form pentagon and hexagon units by in-plane σ-bonding and out-of-plane π-bonding. However, the circular curvature will cause quantum confinement and σ-π rehybridization in which three σ bonds are slightly out of plane. Consequently, the π orbital is more delocalized outside the tube, that is, the *p*-character in the hybridization is increased to some extent than that of the graphite. This makes nanotubes mechanically stronger, electrically and thermally more conductive and chemically and biologically more active than graphite.

CNTs can exist as single tubes (called single-walled nanotubes, SWCNT) or in the form of concentric tubes (termed multi-walled nanotubes, MWCNT). A SWCNT is a hollow cylinder of graphite sheet whereas a MWCNT is a group of coaxial SWCNTs. SWCNTs were discovered[39] in 1993, two years after the discovery of MWCNTs. Brief descriptions of these two are presented in the following subsections.

2.2.3. Single-walled Carbon Nanotubes (SWCNTs)

The discovery of SWCNTs was first reported by *Iijima* and *Ichihashi*[39] in 1993. Such '*single-shell'* CNTs can be visualized as a hollow cylinder, formed by rolling over a graphite sheet[31]. The structure is one dimensional with axial symmetry exhibiting a spiral conformation called chirality[40]. The body of the tubular shell is mainly made of a hexagonal ring of carbon atoms, whereas the ends are capped by dome-shaped half-fullerene molecules composed of hexagonal and pentagonal rings of carbon atoms. The role of the pentagonal ring is to give positive curvature to the surface which helps in closing of the tube at the two ends and also makes the end caps chemically more reactive compared to cylindrical walls of CNTs.

A nomenclature (*n,m*) used to identify each SWCNT, in the literature, refers to the integer indices of two graphene unit lattice vectors corresponding to the chiral vector of the nanotubes[40]. The chirality is given by a single vector called the chiral vector. The chiral vector determines the direction along which the graphene sheets are rolled up to form tubular shell structures perpendicular to the axis vectors[17,40]. The primary symmetry classification of a SWCNT is as either being achiral (symmorphic) or chiral (asymmorphic). An achiral CNT is defined by a CNT whose mirror image has an identical structure to the original one. There are two cases where CNT can be achiral: armchair and zig-zag nanotubes. Chiral nanotubes exhibit a spiral symmetry whose mirror image cannot be superposed on to the original one. Thus, depending on chirality a variety of geometries in SWCNTs, can be obtained. The cross-sections of two different types of CNTs are shown in the *Fig. 2.2(a) and (b)*. A classification of SWCNT is given in the *Table 2.1*.

Table 2.1: Classification of SWCNTs[40]

Type	Chiral Angle (θ)	Chiral vector/ Nomenclature	Shape of cross section
Armchair	30º	(n, n)	*cis*-type ____/
Zigzag	0º	(n, 0)	*trans*-type /\/\/\/\
Chiral	$0^{\circ} < \lvert\theta\rvert < 30^{\circ}$	(n, m)	Mixture of *cis* and *trans*

2.2.4. Multi-walled Carbon Nanotubes (MWCNTs)

A MWCNT is also a rolled up stack of graphene sheets into concentric SWCNTs, with the ends again either capped by half-fullerene or kept open. The walls of each layer of the MWCNT, the graphite basal plane, are parallel to the central axis ($\theta = 0^{\circ}$). Cross-section of a MWCNT is shown in *Fig. 2.2(c)*. In contrast, a stacked-cone arrangement is also seen where the angle between the graphite basal planes and the tube axis is non-zero. The length of the MWCNTs is in the range from a few tens of nanometers to several microns, and the outer diameter is from as low as 2 *nm* to sometimes more than 100 *nm*. At high resolution in transmission electron microscopy (TEM), the individual layers making up the concentric tubes can be imaged directly. It is quite frequently observed that the central cavity of a nanotube is traversed by graphitic layers effectively capping one or more of the inner tubes and reducing the total number of layers in the tube. Virtually all of the tubes are closed at both ends with caps which contain pentagonal and hexagonal carbon rings. The caps can have a variety of shapes along with hemispherical shape. A detailed discussion of the structural aspects of MWCNTs is presented in the results and discussion chapter.

A CNT is called MWCNT if it has at least two concentric walls. The distance between the two concentric walls is approximately 0.334 *nm*. So the successive tubes should differ in the circumference by (2π × 0.334) *nm* ≈ 2.1 *nm*. It is assumed that the walls are not created from scrolling of the graphene sheets. It can readily be seen that this is not possible for zig-zag nanotubes, since 2.1 *nm* is not a precise multiple of 0.246 *nm*, the width of one hexagon[33]. In the case of armchair tubes, multi-walled structures can be arranged in such a way that the interlayer distances is 0.34 *nm*. This is because 2.1 *nm* is close to 5 × 0.426 *nm*, the length of the repeat unit from which armchair tubes are constructed. For chiral nanotubes, the situation is complicated, but it is not possible to have two tubes with exactly the same chiral angle separated by the interlayer distance[33] of 0.34 *nm*. A MWCNT may contain achiral as well as chiral and also exhibit several chiral angles.

The energetics of MWCNTs have been considered by *Charlier* and *Michenaud*[41]. They found that the energy gained by adding a new cylindrical layer to a central one was of the same order as the one in graphite bilayering. The optimum interlayer distance between an inner nanotubes (5,5) and outer (10,10) tubes was found to be 0.339 *nm*. This is somewhat different than the spacing found for turbostratic graphite[33]. The estimated translational and rotational energy barriers for the two coaxial tubes were 0.23 *meV* per atom and 0.52 *meV* per atom respectively. These low values suggest that a significant translational and rotational mobility could be present in MWCNTs at room temperature, although in reality the presence of caps and defects in the cylindrical structures would limit this mobility[33].

The electronic conduction process in CNTs is unique since in the radial directions, the electrons are confined in the singular plane of the graphene sheet. The conduction occurs in the arm chair tubes through gapless modes as the valence and conduction bands always cross each other at the *Fermi* energy. In other types of SWCNTs, an opening of the energy gap at the *Fermi* energy leads to semiconducting properties. As the diameter increases the band gap tends to zero as it varies inversely with tube diameter. In a MWCNT, the electronic structure of the smallest inner tubes is super imposed by the outer one. Therefore, the band structure obtained from an individual MWCNT resembles that of graphite[42].

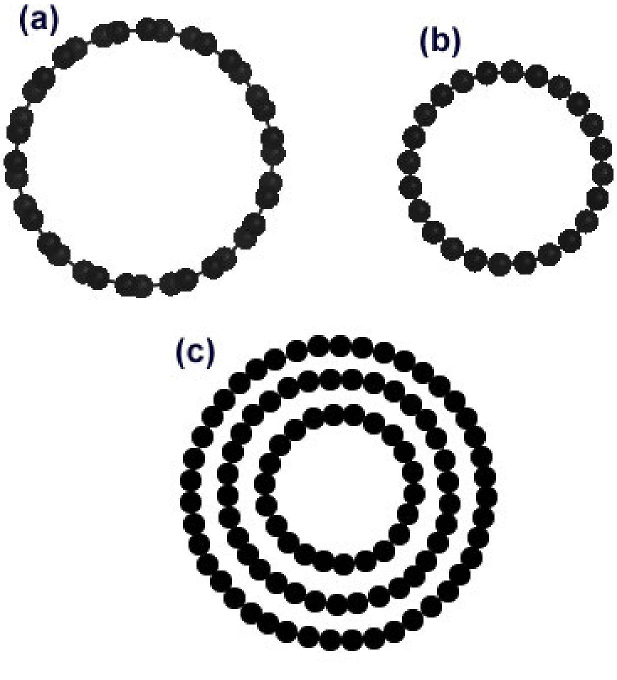

Fig. 2.2: Schematic cross-sections (not in scale) of (a) (9, 9) SWCNT; (b) (12,0) SWCNT and (c) MWCNT

2.2.5. Physical Attributes of CNTs

During the last few years, physicists, chemists, and materials scientists across the globe have been amazed by the fascinating properties of CNTs. Physicists have been attracted to their extraordinary electronic properties, chemists to their potential as nanotest-tubes and materials scientists to their amazing stiffness, strength and resilience. On a more speculative level, nanotechnologists have discussed possible nanotubes based gears and bearings[33]. The electronic structure of CNTs depends on the details of the microstructure. An analysis[43] shows that a nanotube is metallic at room temperature if $(n-m) = 3i$ is an integer. Otherwise, it is semiconductor with band gap $E_g = (0.9/d)\ eV$, where d is the diameter of nanotubes in nm. The diameter of a CNT can be expressed as $\sqrt{3}a_{c-c}\ (n^2 + nm + m^2)^{0.5}$, where a_{c-c} is the C-C bond length. This remarkable property[44,45] signals the possibility of band-gap engineering by control of the microstructure. Since its discovery, many outstanding physical attributes have been observed for CNTs. The most noteworthy are mentioned in the *Table 2.2*.

Table 2.2: Summary of physical attributes of CNTs[43,46]

Attributes	Comments
CNT: metallic, semiconductor and nonconductor (depending on microstructure)	No other known molecule has this property
Axial electrical conductivity: $10^{8}\ \Omega^{-1}.m^{-1}$	Comparable to that of copper
Axial thermal conductivity: $10^{4}\ W.m^{-1}.K^{-1}$	Greater than that of diamond
Carrier mobility: $10^{4}\ cm^{2}.V^{-1}.s^{-1}$	Greater than that of GaAs
Supports a current density of $10^{9}\ A.cm^{-2}$	Because of very weak electromigration
Optical-Optoelectronic application with wavelength: 300-3000 *nm*	Direct band gap and one-dimensional band structure
Nano-scale heterojunctions	Common defect that can create an on-tube heterojunction
Axial Young's modulus: 1 *TPa*	Stiffer than any other know material
Axial tensile strength: 150 *GPa*	600 times the strength/weight ratio of steel
CNT quantum electronic and low-dimensional transport phenomena	True quantum wire behavior, Room-temperature field effect transistor, Room-temperature single-electron transistor, *Luttinger*-liquid behavior, *Aharonov-Bohm* effect, *Fabry-Perot* interface

2.3. Methods for Synthesis of CNTs

Although CNTs can be synthesized using a variety of techniques, the following three methods are used for commercial and bulk production of carbon nanotubes: arc discharge, chemical vapor deposition and laser ablation. These processes along with other methods are discussed following in brief.

2.3.1. Arc-discharge

The arc discharge technique for synthesizing MWCNTs appears to be a simple and traditional tool, but obtaining high yield is difficult and requires careful control of experimental conditions. In the most common laboratory scale production scheme, the DC arc operates in a 1-4 *mm* wide gap between two graphite electrodes of diameter 6-12 *mm* that are vertically or horizontally installed in a water cooled chamber filled with helium gas at sub-atmospheric pressure. Helium gas and DC current are more important to maximize the yield. Typical conditions for operating a carbon arc for the synthesis of CNTs include the use of graphite rod with a voltage 20-25 *V* across the electrodes and a DC electric current of 50-120 *A* flowing between the electrodes. The arc is typically operated in ~500 *Torr* helium with a flow rate 5-15 $ml.s^{-1}$ for cooling purposes. As the CNTs form, the length of the positive electrode (anode) decreases.

SWCNTs are produced in the arc-discharge process utilizing covaporization of graphite and metal in a composite anode (positive electrode), commonly made by drilling an axial hole in the graphite rod and densely packing it with a mixture of metal and graphite powder. Although, almost all transition metal particles, some rare-earth metals, alkaline earth metal and some *p*-block metal particles and also their mixture are used for synthesizing SWCNTs, presently only *Ni/Y* and *Co/Ni* catalysts are commonly used for SWCNT production[17].

2.3.2. Laser Ablation

During fullerene production experiments using a laser vaporization apparatus with an ablated graphite sample positioned in an oven, it was found that closed-ended MWCNTs were produced in the gas phase through homogeneous carbon-vapor condensation in a hot argon atmosphere. The laser-produced MWCNTs are relatively short, approximately 300 *nm*, although the number of layers, ranging between 4-24, and the inner diameter, varying 1.5-3.5 *nm*, are similar to those of arc-produced MWCNTs. A prevalence of MWCNTs with an even number of layers was observed, but no SWCNTs were detected[17]. But evaporation of a carbon-metal composite target with laser light pulses, either separate or frequently repeated and with continuous illumination by laser and solar light, can bring about SWCNT formation. A 70-90 *%* conversion of graphite to SWCNTs was reported in the condensing vapor of the heated flow-tube operating[40] at 1200 º*C*. A *Co-Ni* /graphite composite laser vaporization target was used, consisting of ~1 *at% Co-Ni* alloy (equal percent) added to graphite. Two sequenced laser pulses were used to evaporate a target containing carbon mixed with a small amount of transition metals from the target. Flowing of argon gas sweeps the entrained nanotubes from the high-temperature zone to the water cooled *Cu*-collector downstream, just outside the furnace.

2.3.3. Chemical Vapor Deposition

Chemical vapor deposition (CVD) can be categorized depending on the energy sources: plasma-enhanced CVD (PECVD) and thermal CVD.

i. PECVD:

The plasma-enhanced CVD first emerged in microelectronics because some of the processes cannot tolerate elevated temperatures of the thermal CVD. It has emerged as a key growth technique to produce vertically aligned CNTs. In CNT growth, precursor dissociation in the gas phase is not necessary; however, dissociation at the catalytic particle surface appears to be the key for nanotube growth. The growth temperature is necessarily maintained below the pyrolysis temperature of the particular hydrocarbon to prevent excessive production of amorphous carbon.

ii. Thermal CVD

When a conventional heat source, such as a resistive or inductive heater, furnace or infra-red (IR) lamp, is used, the technique is called thermal CVD or simply CVD. The thermal CVD apparatus for CNT growth is very simple. It consists of a quartz tube of 1-2 *inch* diameter, inserted into a tubular furnace capable of maintaining a constant temperature over a 25-*cm* long zone. In thermal CVD, hydrocarbons or CO are used as precursor. A typical growth run would involve first purging the reactor with some inert gas. Then the gas flow is switched to the feedstock for the specified growth period. At the end, the gas flow is switched back to the inert gas while the reactor cools down. For growth on the substrates, the catalyst mixtures need to be applied to the substrate before loading it inside the reactor.

2.3.4. Electrochemical Methods

An electrochemical method for the synthesis of MWCNTs has been described in the literature[33]. This process involves the electrolysis of molten lithium chloride using a graphite cell in which the anode is a graphite crucible and a graphite rod immersed in the melt as a cathode. A current of 30 *A* is generally used through the cell for one minute, after which the electrolyte is allowed to cool and then added to water to dissolve the lithium chloride and react with lithium metals. The solution is treated with toluene which contains CNTs.

Taking another innovative approach, *Pal et al.*[47] attempted to grow CNTs on a silicon (001) substrate by an electrodeposition technique using acetonitrile (1 %*v/v*) and water as electrolyte at an applied potential of 20 *V*. The electrolysis of acetonitrile was carried out at atmospheric pressure and the bath temperature kept at ~300 *K*. CNTs were deposited onto a Si wafer (resistivity ~ 15 *kV*) of dimension 10 *mm* × 8 *mm* × 0.3 *mm* attached to a copper cathode. The inter-electrode distance was ~8 *mm* and the deposition time was 4-6 *h*. The typical thickness of the CNT film was ~300 *nm*, measured by interferometry.

2.4. Carbon Nanotubes Decorated with Nanoparticles

While pristine CNTs have unique electronic properties for numerous applications, CNTs filled with elements and compounds exhibit fascinating and desirable properties to serve as nano-scale chemical reactors. Research on decorating CNTs has been one of the most active fields of nanotubes research.

2.4.1. Synthesis of CNTs Decorated with Nanoparticles

When CNTs were discovered, it was a natural attempt to introduce foreign materials into the central cavities. Generally, the filling of CNTs is accomplished using two processes[48-51]. The first involved carrying out arc-discharge in the usual way, but with an anode containing some of the materials to be encapsulated. This technique generally seems to favor the formation of filled particles, and only applicable to materials which can survive the extreme condition of the electric arc[33]. The second approach involves several steps after synthesis of CNTs by the usual way. For internal filling of CNTs, at least two steps are required: opening up and filling the nanotubes through either capillary action or other chemical means. Such decoration of CNTs with nanoparticles is accomplished as a post-processing step which involves deposition of nanoparticles on nanotubes by various means. In the literature, a variety of decoration techniques for CNTs with nanoparticles was reported through variety of ways. Some of the most important procedures are discussed here.

Ang et al. attempted to decorate CNTs using an electroless plating synthesis[52]. In their route, the first step was to activate the CNTs with *Pd-Sn* catalytic nuclei via a single-step activation approach. Such activated nanotubes were used as precursors for obtaining nickel- and palladium-decorated nanotubes via electroless plating. Activation of the nanotube surfaces promoted specific deposition of the metals on the catalytic tube surfaces. As a result, CNTs densely coated with metal nanoparticles were obtained with reduced metal deposition in the reaction solution. However this method needs several steps to decorate the CNTs. *Ye et al.*[53] tried to decorate palladium particles on CVD-grown CNTs by hydrogen reduction of a *Pd(II)*-β-diketone precursor in super critical carbon dioxide with precisely controlled temperature and pressure environment. Their study demonstrated the deposition of palladium nanoparticles (5-10 *nm*) on MWCNTs using a complicated instrument. This procedure is not only time consuming but also inefficient. Deposition of platinum nanoparticles and nanoclusters on functionalized CNTs was attempted by *Liu et al.*[54]. In their study a higher yield of functionalized CNTs was obtained by treatment of CNTs in HNO_3 or H_2SO_4-$K_2Cr_2O_7$. The deposition of platinum nanoparticles and nanoclusters on these functionalized MWCNTs by electroless plating and two-step sensitization-activation pretreatment. Several complicated steps are required for bulk synthesis using this process. *Lordi et al.*[55] synthesized SWCNTs coated with platinum nanoparticles using a three step process. First step was the purification of SWCNTs using HNO_3. This was followed by a weak oxidation to create anchor sites for the platinum. Finally, platinum was attached to the surface oxidized SWCNTs by reduction of K_2PtCl_4 in ethylene glycol. Despite its high efficiency, multiple steps make this process time consuming. *Planeix et al.*[56] synthesized ruthenium decorated CNTs for heterogeneous catalysis using a ruthenium precursor. Ruthenium 2,5-pentanedionate was dissolved in toluene for 72 *hrs* in contact with CNTs. The

CNTs were separated from toluene by drying toluene. Afterwards, the CNTs were treated for 3 *hrs* under a stream of nitrogen at 523 *K* and then reduced for 1 *h* in a stream of diluted hydrogen. *Che et al.*[57] used a very complex method to decorate the CNTs. They synthesized ensembles of highly aligned monodisperse CNTs within the pores of alumina membranes using CVD. The CNT/alumina membranes were immersed into a solution of the desired metal ion for 5 *hrs*. The membrane was dried in air and the ions were reduced to the corresponding metal or alloy by 3 *hrs* exposure to flowing hydrogen at 580 º*C*. The underlying membrane was dissolved away by immersion in 46 % *HF* solution to obtain the desired free standing CNTs. A series of CNTs decorated with various catalysts were synthesized by a constant pH co-precipitation method[58]. A series of aqueous solutions of metal precursors was prepared by dissolving appropriate metal nitrate-salts. A 4*N* Na_2CO_3 solution was added drop-wise to the solutions with vigorous stirring at a constant temperature of 353 *K*. The addition of such solution was adjusted to maintain a constant *pH* of 7.0. The precipitation procedure was completed in 1 *h*. Repeated rinsing samples was required to remove the sodium ions. In another attempt, *Luo et al.*[59]synthesized CNTs supporting rhodium for nitric oxide catalysts. First, the CNTs were synthesized by means of *CO* disproportionation using a hydrogen-reduced Ni/La_2O_3 catalyst at 600 º*C* for 30 *min*. The CNT-supported rhodium were prepared by treating the CNTs with a 5 *mM* $RhCl_3$ solution. These materials was dried at 80 º*C* and calcined at 500 º*C* in air for 2 *hrs*.

Hsin and coworkers[60] attempted to produce metal-filled CNTs using arc discharge in a cobalt sulfate solution which resulted in the formation of CNTs-filled with not only metallic cobalt, but also cobalt sulfide particles. The encapsulated particles were mostly rod-shaped. Moreover, the mechanism of the encapsulation of such particles was not clear from such attempts[60]. Preparations of *TiC*-[61] and *Cu*-[62] filled nanotubes using a CVD process were attempted; however, the filler material was continuous along the length of the nanotube. Nanowire-filled CNTs posses a surface area less than that of CNTs filled with nanoparticles, hence, the latter is more suitable for gas storage applications.

2.4.2. Applications of CNTs Decorated with Nanoparticles

1. Catalytic Applications

The regeneration of water to replenish this important component for sustaining life during space missions is extremely important because 92 % of the total consumable mass used by the space crew is water[63]. Moreover, such regenerated water can also be used to produce oxygen, another important constituent for a life support system. A significant amount of CO_2 is present in the lunar atmosphere[64]. Water can be regenerated by reduction of CO_2 and hydrogen over a suitable catalyst. The *Sabatier*[65] and *Bosch* processes[66] are two carbon dioxide reduction systems. *Sabatier* reaction (*Eq. 2.1*) utilizes an alumina supported ruthenium catalyst and, in comparison to the Bosch reaction (*Eq. 2.2*), has the advantage of greater thermodynamic favorability and higher reaction rates. Nevertheless, the efficiency of this reaction is too poor to be used successfully for a life support system. The only way to improve the efficiency is by increasing the catalytic activity of the reaction. Therefore, developing a technology for conversion of carbon dioxide into water by using a physico-chemical process remains a challenging task towards development of an advanced life support system in space which can supply the basic necessities to the crew.

$$\textit{Sabatier}\text{ Reaction } CO_2(g) + 4H_2(g) \rightarrow CH_4(g) + 2H_2O(l) \qquad \textit{Eq 2.1}$$

Bosch Reaction $CO_2(g) + 2H_2(g) \rightarrow C(s) + 2H_2O(l)$ *Eq 2.2*

Table 2.3: Catalytic activity comparison with other carbonaceous materials

Catalyst	Reactions	Results
Rh-MWCNT	*NO* Decomposition[67]	Higher conversion rate than $Rh\text{-}Al_2O_3$
	Cinnamaldehyde Hydrogenation[68]	Three times higher rate than *Rh*-activated Carbon
Pt-Graphite Nano-fiber (GNF)	n-Hexen Reaction[69]	Higher selectivity than Pt/SiO_2
	Methanol oxidation[69]	Higher rate than Pt-vulcan carbon electrode
Co-MWCNT	Cyclohexanol dehydrogenation[70]	Higher activity than cobalt-activated carbon
Rh-GNF	Ethylene Hydroformylation[69]	Activity higher than cobalt-activated carbon
Ni-GNF	Butene Hydrogenation[69]	Higher conversion rate than $Ni\text{-}Al_2O_3$ and *Ni*- activated carbon
	Methane Decomposition[69]	Higher than $Ni\text{-}Al_2O_3$

Thus the development of advanced catalytic support materials is of utmost importance to build a clean environment. A three-way catalytic converter is usually used to reduce various gases such as NO_x, and *CO* using reducing and oxidizing catalysts. Both these catalysts consist of a ceramic structure coated with a metal catalyst (usually platinum, rhodium and/or palladium).

As these catalysts are very expensive metals, it is always beneficial to create a structure that exposes the maximum surface area with minimum amount of catalyst to the exhaust stream to optimize the cost. So, implementation of nanostructured catalyst materials is an effective way to reduce the cost due to high surface area. Cerium oxide is used as a catalyst in a wide variety of reactions involving the oxidation or partial oxidation of hydrocarbons because the ceria lattice can contain a high concentration of highly mobile oxygen vacancies and can thus act as a local sink for oxygen involved in the reactions. A number[71] of metal oxides can function as decomposition catalyst for conversion of NO_x. It is widely accepted that the oxygen defects on the surface of metal-oxide catalysts are the active centers for reduction[72]. Up to 80 % conversion of nitrogen oxides to N_2 was observed for alumina at 500 °*C*. Alumina and zirconia aerogels exhibited higher catalytic activities at lower temperatures. Such high catalytic activity was attributed to the high effective diffusivity of the reaction gas in the porous nanostructures. The role of ceria, niobium and molybdenum oxides on the promotion of the nitrogen oxide reduction by *CO* was studied by *Noronha et al.*[73].

Among the different types of supports used in heterogeneous catalysis, carbon materials attract a growing interest due to their specific characteristics. These characteristics include resistance to acid/basic media, possibility to control up to certain limits, the porosity and surface chemistry and ease of recovery of precious metals burned resulting in a low environmental impact[74]. CNTs might function by routing molecules through the channels between the layers of close-packed tubes. Opened nanotubes have been shown to intercolate many materials[61,75,76]. Carbonaceous materials in various forms[35-37] have high temperature durability. Therefore it has a great potential in catalytic applications[71,74,77]. Besides their use as supports, CNTs have been used as direct catalysts for the decomposition of various gases[77,78]. Data in *Table 2.3* implies that CNTs and carbonaceous materials have the capability to improve the catalytic activity.

2. Hydrogen Storage Materials

Hydrogen storage in CNTs has been a subject of intense research[79-85]. According to the literature[82], the storage potential of CNTs must exceed 8 *wt%* of hydrogen to power electric vehicles effectively. However, recent studies[83,84] confirm that hydrogen uptake in CNTs is limited to 2 *wt%*. CNTs combined with selective elements and compounds exhibit enhanced desirable properties to serve as nano-scale chemical reactors for the aforementioned applications[52-59]. Lithium- and potassium-doped CNTs have also been studied for the development of materials for hydrogen storage[84] and solid-state batteries[86]. Palladium nanoparticles on CNTs have received considerable attention for a variety of such potential applications. CNTs decorated with *Pd*-nanoparticles exhibit fascinating and desirable properties for nano-scale storage as palladium has very high affinity towards hydrogen[87,88].

3. Other Applications of Nanoparticles Decorated CNTs

Numerous applications of nanoparticles decorated CNTs have been found in the literature. *Ye et al.*[53] reported the deposition of 5-10 *nm* sized palladium nanoparticles on multi-walled CNTs (MWCNTs) by hydrogen reduction of *Pd*(II)-β-diketone precursors in the presence of supercritical carbon dioxide. The system showed[53] promising catalytic properties towards hydrogenation of olefins in carbon dioxide and electro-reduction of oxygen in fuel cell applications. CNTs can also act as field-effect transistors by coupling with metals. However, the presence of a *Schottky* barrier at the metal-CNT junction is a serious problem[89,90]. In order to circumvent such a problem, *Jamey* and co-workers[91] have recently fabricated a high-performance ballistic nanotube field-effect transistor using palladium with a single-wall carbon nanotube (SWCNT) junction that reduces the *Schottky* barrier to a great extent. Copper-filled CNTs[62] are suggested as an interconnect material for integrated circuits. All such studies indicate that synthesis of metal-filled CNTs has tremendous potential for technological applications.

2.5. Arc-discharge in Liquid Phase

Although different methods have been employed for the synthesis of multi-walled carbon nanotubes (MWCNTs), arc discharge in water and in solution (ADS) methods have proven to be highly efficient to researchers. During the last couple of years, arc-discharge in the liquid phase has attracted considerable attention due to its simplicity[92-98]. In several publications[99-102], the arc discharge in solution (ADS) procedure is discussed elaborately. Without maintaining a vacuum, carbon nanostructures can be synthesized with a simple technique avoiding costly and time consuming equipment. The method has not only assisted production of clean CNTs, but also the synthesis of in-situ decorated CNTs with metallic and ceramic nanoparticles has been successful[99,100,101,102].

Besides these preliminary investigations on the arc-discharge in a liquid phase on the synthesis of carbonaceous materials, detailed parametric studies on the synthesis of CNTs in the liquid phase have not been attempted so far. *Ishigami et al.*[92] first reported in 2000 the continuous synthesis of MWCNTs in liquid nitrogen using a dc power supply of 20-25 *V* operating at 60 *A*. *Hsin* and coworkers[60] attempted to produce metal-filled CNTs using arc discharge in a cobalt sulfate solution, which resulted in the formation of CNTs-filled with not only metallic cobalt but also cobalt sulfide particles. The encapsulated particles were mostly rod-shaped. Moreover, the mechanism of the encapsulation of such particles was not clear from such attempts. During the synthesis of carbon-onions, Sano and coworkers found rod shaped carbon nanostructures, carbon nanotubes and carbon onions. *Zhu et al.*[103] took an initiative to synthesize MWCNT's using a dc power supply inside water maintaining at dc 30 *V* and 50 *A*. They categorized the product into three different categories: (i) floating materials, (ii) hard deposits on cathode's surface, and (iii) hard carbon plates dropped and collected from the bottom of the container. The yield is 7.0 $mg.min^{-1}$, however, the CNTs were associated with a multitude of impurities. Water-protected arc discharge (WPAD) was reported with a DC (30 *V* and 50 *A*) using a drill-holed cathode packed with a metallic catalyst (Ni:Y=5:1). The product was a collected product from the drill-hole of the anode. Although, performances of synthesis of CNTs were explored in two different liquid media, liquid nitrogen and deionized water, a detailed parametric study has not been reported. The pressure effect on the synthesis of CNTs through arc-discharge in water was studied by *Sano et al.*[104]. They found that the diameter of CNTs increases with decreasing hydrostatic pressure used in this process. In another attempt, *Sano et al.*[105] synthesized SWCNTs along with carbon nanohorns using liquid nitrogen and *Ni* as catalyst. They found that a relatively inert environment is required to synthesize SWCNTs and carbon nanohorns selectively. *Lange et al.*[97] demonstrated the production of well-crystallized nano-onions, nanotubes, fully and partially filled with crystalline metallic particles using the arc-discharge in water methodology. Using alternating current (AC) arc discharge in water, *Biró et al.*[94] produced well-graphitized MWCNTs. They found that the arc is stable at a voltage of 40 *V* in a current range of 45-85 *A*. However they reported lower current values help to increase the fraction of CNTs in the product. *Antisari et al.*[96] analyzed the MWCNTs synthesized by arc-discharge in liquid media, liquid nitrogen and water. They reported water provides a suitable environment to synthesize high-quality CNTs. They[96] purified the raw MWCNTs selectively through air oxidation at 500 º*C* for 30 *min*. Recently, *Montoro et al.*[106] reported the synthesis of SWCNTs and MWCNTs by the arc-discharge in water method. However, a large quantity of graphite particles with estimated diameters ranging from 10 *nm* to 600 *nm* was present in the sample. Moreover, it was found that the concentration of elongated straight structures was low.

2.6. Importance of this Study

There are three methods available which are widely used for commercial manufacturing of CNTs: arc-discharge in vacuum, laser ablation and chemical vapor deposition (CVD). These methods generally rely on the presence of metallic catalysts in the form of nanoparticles that are planted previously on the templated substrate. Such procedures cause dispersion of catalytic nanoparticles along the CNT specimen. An additional process is generally employed to clean up the catalyst nanoparticles from the CNTs. The additional steps of nanotube decoration increases the overall production cost. A unique method of synthesis of CNTs is required which can produce clean CNTs and needs no further major purification procedures.

More than 1100 papers and about 100 patents related to synthesis aspects of CNTs have been published to date[107]. Despite such tremendous research efforts, the low-cost, large-scale production of high-quality CNTs is yet to be reported[108], due to the proprietary nature of all the processes. High costs and complicated instrumentation along with maintaining high-vacuum conditions for the synthesis of CNTs have made the above mentioned methods inaccessible to the majority of researchers across the world. A simple and inexpensive route of synthesis is required to synthesize CNTs which can bring down the overall production cost of CNTs.

To decorate the CNTs with nanoparticles, the existing methods need at least two steps. An additional step of decoration is not only inefficient, but also adds to the overall production cost. A technique which simultaneously decorates the nanotubes with nanoparticles during its synthesis is inherently devoid of such disadvantages. Besides preliminary investigations on arc-discharge in the liquid phase on the synthesis of carbonaceous materials, as mentioned earlier, detailed systematic studies on the in-situ decoration of CNTs with nanoparticles have not been attempted so far. So, a procedure is required which results in-situ decoration of CNTs with nanoparticles. The present work studies, the in-situ decorating of CNTs with nanoparticles using arc discharge in solution. The present investigation also focuses on the mechanistic aspects of the formation, the decoration of nanoparticles in the nanotubes and on the systematic parametric studies.

Although arc discharge in the liquid phase is highly efficient for bulk production, one of the major gaps in the past research, as reviewed from published literature, is a comprehensive study that correlates parametric data from the experimental synthesis method. The purpose of such study is to synthesize MWCNTs in a controllable manner through correlation of growth parameters with yields that will be one step closer to the preferential efficient production of CNTs. In other words, there has been a lack of correlation between the yields, currents and voltage. The knowledge of current/voltage characteristics in the process of CNT production is essential as the efficiency of the production rate is controlled by these parameters. Completion of the parametric research is necessary in order to fill these gaps in the published literature.

For the arc-discharge in water or solution method, a full-fledged instrumentation for such method is required for bulk production. Although, instrumentation details for arc-discharge in vacuum are reported in the literature[109], that for arc-discharge in solution (ADS) is yet to be published. The aim of the present work is to develop a simple, inexpensive, optoelectronically automated instrumentation for the bulk synthesis of carbon nanostructures and in-situ decorated CNTs with industrially important nanoparticles.

The characterizations of pristine CNTs and CNTs decorated with nanoparticles are also part of the objective. The synthesized nanostructured materials have been characterized by transmission electron microscopy (TEM), high resolution transmission electron microscopy (HRTEM), scanning transmission electron microscopy (STEM), X-ray diffraction (XRD), scanning electron microscopy (SEM), energy dispersive spectroscopy (EDS), and X-ray photoelectron spectroscopy (XPS) to obtain information of their size, morphology, structures, chemical constituent and chemical state. These characterization results were used to gain the needed insights for the growth mechanisms of CNTs.

CHAPTER 3: EXPERIMENTAL WORK

As discussed previously, the objective of the current research is to develop a simple, inexpensive method of CNT synthesis. In the present research, arc-discharge in water or in solution is used for the synthesis of carbon nanostructures. We have named this method the ADS process. In this chapter, building the setup for the arc-discharge in solution (ADS) process, experimental procedures for the synthesis of CNTs and CNTs decorated with nanoparticles including the systematic parametric studies on the ADS process and the purification of CNTs will be discussed. The different characterization techniques used during the study are also explained.

3.1. Chemicals

During this investigation, several different selected chemicals were used. In the following table, the chemicals used in the present work are tabulated with their specification and commercial supplier.

Table 3.1: List of chemicals used during present investigation

Chemicals	Purity	Commercial Supplier
Graphite rod	99.9995%	*Alfa-Aesar®*
Palladium (II) chloride	99%	*Aldrich Chem. Co.*
Cerium (III) Nitrate hexahydrate	99%	*Aldrich Chem. Co.*
Tetra-ethylene-ortho-silicate (TEOS)	98%	*Aldrich Chem. Co.*
Nickel (II) nitrate hexahydrate	99.999%	*Aldrich Chem. Co.*
Hydrochloric Acid	37%	*Aldrich Chem. Co.*

3.2. An Optoelectronically Automated System for ADS

In the ADS process, the fraction of carbon deposited on the cathode depends on the volume of the plasma. Thus, the influence of the relative distance between the two electrodes during ADS is a very important factor for overall system performance. Secondly, during the synthesis of CNTs, various noxious gases are produced. Carbon monoxide, carbon dioxide, chlorine gas along with water vapor are all by-products as noted in *Eqs. 3.1, 3.2* and *3.3*. Such gases and excessive heat may be harmful to humans if the system is to be operated manually. Automation of the system for the arc discharge in the solution is proposed as a way to perform the experiment without the need of human interaction and allow for bulk production of CNTs in a safer environment.

$$2C(g) + O_2(g) \xrightarrow{\Delta} 2CO(g) \qquad (Eq.\ 3.1)$$

$$2CO(g) + O_2(g) \xrightarrow{\Delta} 2CO_2(g) \qquad (Eq.\ 3.2)$$

$$H_2O(l) \xrightarrow{\Delta} H_2O(g) \qquad (Eq.\ 3.3)$$

Herein, an optoeletronically automated system was built which consists of two main units: a unit of basic components for arc-discharge and an optoelectronically control unit. A schematic diagram showing all parts of the two main components are shown in *Fig. 3.1*.

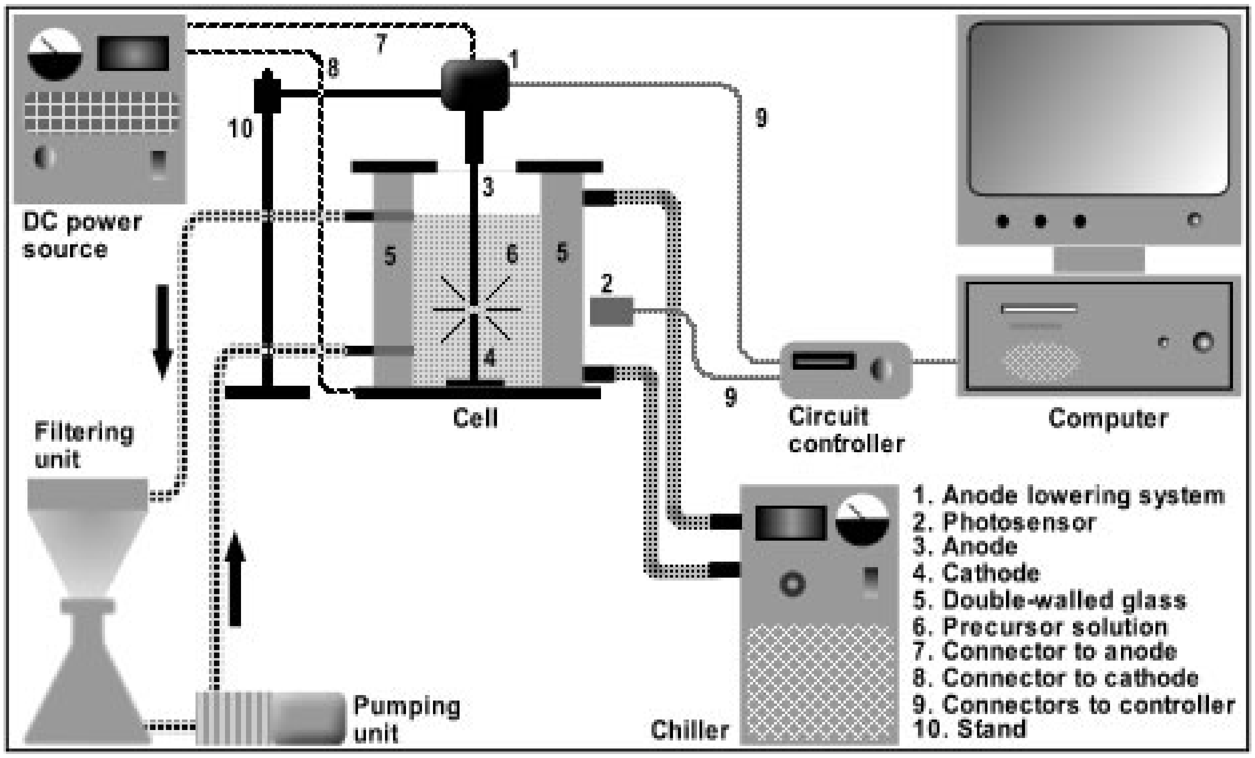

Fig. 3.1: A schematic diagram of a set-up for the synthesis of carbon nanotubes (CNTs) and nanoparticles decorated CNTs using the ADS method

3.2.1. Basic Components

The basic components of the setup for arc discharge in solution are composed of (1) a cell, (2) a DC power supply system, (3) a filtering unit, and (4) a chilling loop. The cell is the main part of the whole setup. The electrodes are brought in contact to strike an arc inside the cylindrical cell. *Fig. 3.2(a)* shows a three-dimensional diagram of the cell with a height of 20 *cm* that consists of a double walled glass container with 2 *cm* thickness for a flow of cooling water at 7 º*C*. The outer and the inner walls are marked as '*i*' and '*j*' in the *Fig. 3.2*, respectively. The inner diameter of the cell is 10 *cm*. The cell has two inlets, labeled as '*d*' and '*e*' in the *Fig. 3.2*, and two outlets, labeled as '*c*' and '*f*'. A pair of the inlets and outlets is connected to the volume between the double walls for the cooling of the cell with a flow of chilled-water as shown in *Fig. 3.1*. The other pair is directly connected to the interior of the cell for filtering the carbon nanotubes from the cell and filling the cell with filtered solution, as shown in the *Fig. 3.1*. Two stainless steel plates are placed on the two open ends of the cylindrical cell. These plates are labeled as '*a*' for the upper stainless plate and '*b*' for the lower stainless steel plate. The bottom stainless steel plate is used to attach the cathode electrode through a holder indicated by '*g*' in *Fig. 3.2(b)* (a dimensional sketch of the cell). Three metal connecting rods outside the cell are 120 *degree* apart from each other to hold the two stainless plates together. One such rod has been shown in the *Fig. 3.2* as '*h*'. The anode electrode is connected to the anode lowering unit labeled as '1' in *Fig 3.1*. The lowering unit allows the anode to move along its vertical path.

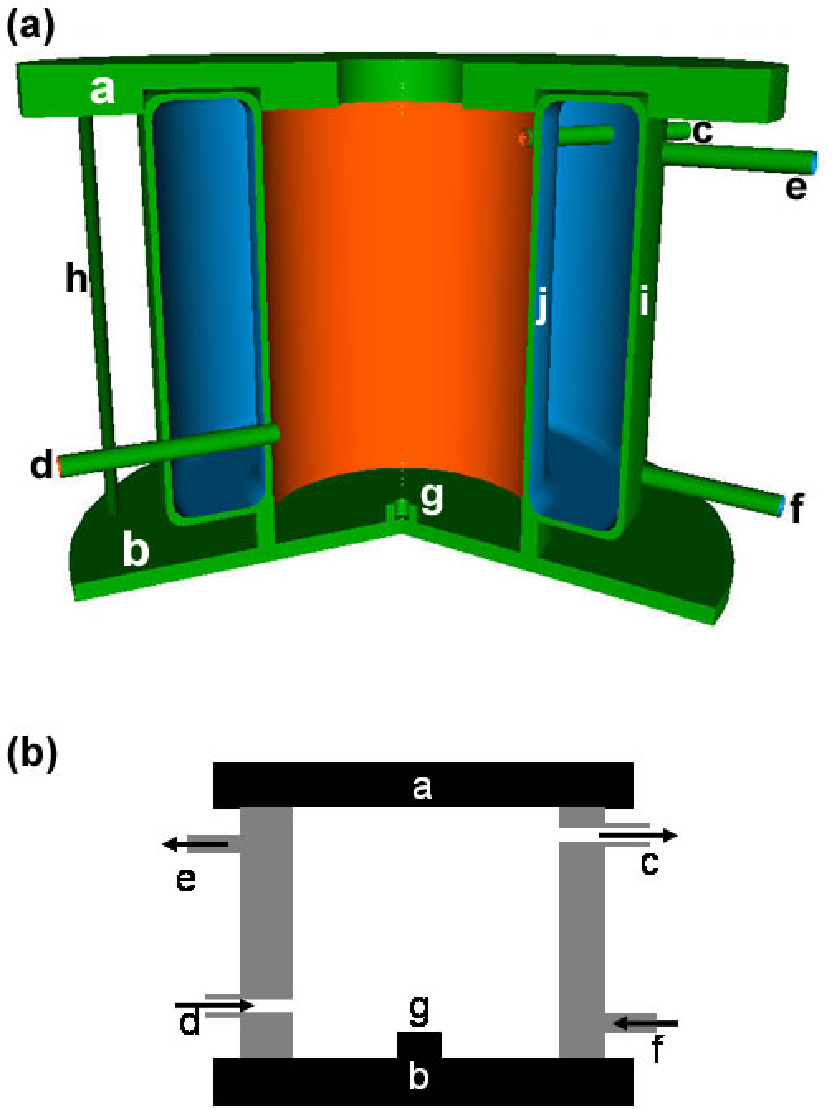

Fig. 3.2 (a) A three dimensional view of the cell, (figure not drawn to scale). (b) Schematic diagram of the cell for arc-discharge in solution. a: the upper stainless plate, b: the lower stainless steel plate, c: the outlet from the inner volume to the filtering unit, d: the inlet to the inner volume from the filtering unit, e & f: the pair of inlet and outlet, connected between the outer volume and the chiller, g: the cathode holder, h: one of the three metal rods for holding the top and bottom stainless steel plates together, they are situated at 120 degrees from each other, i & j: the outer and inner walls, respectively

3.2.2. Optoelectronic Control Unit

The concept of an optoelectronically optimized automation process is presented in *Fig. 3.3(a)*. It was adopted to make the arc-discharge process continuous by feeding the anode electrode vertically towards the cathode. A pre-selected constant distance can be maintained between the two electrodes using the optoelectronic system to sustain the arc. The system consists of three main components: (a) a photosensor for an optical emission diagnosis, (b) a feedback loop which is composed of analogue electronics and a computing unit, and (c) a servo unit for the *Z*-axis translation of the anode. The servo unit, which is shown in *Fig.3.1* as the anode lowering system, is coupled with *X*, *Y* and *Z* translational levers. The servo unit is controlled by pulse from the analogue controller unit. The speed of *Z*-translation depends on the duration of the pulses which are specified by the analogue controller unit. Generally *X* and *Y* positions are specified by the user before the arc discharge process begins. Since the *Z*-position is solely based on pulse and pulse duration, very precise movements along the *Z*-axis are easily achievable.

The electronics of the analogue controller unit is a kit of the BASIC Stamp (Home version). The electronic circuit of the controller is presented in *Fig. 3.4*. It is basically a programmable logic device. This BASIC stamp kit consists of necessary parts including resistors, light emitting diodes (LEDs), push buttons, and capacitors. The whole unit is powered by a 9 *V* battery. The capacitor is in parallel with the photosensor. The pins, which are shown in *Fig. 3.4*, are used as signal inputs and outputs.

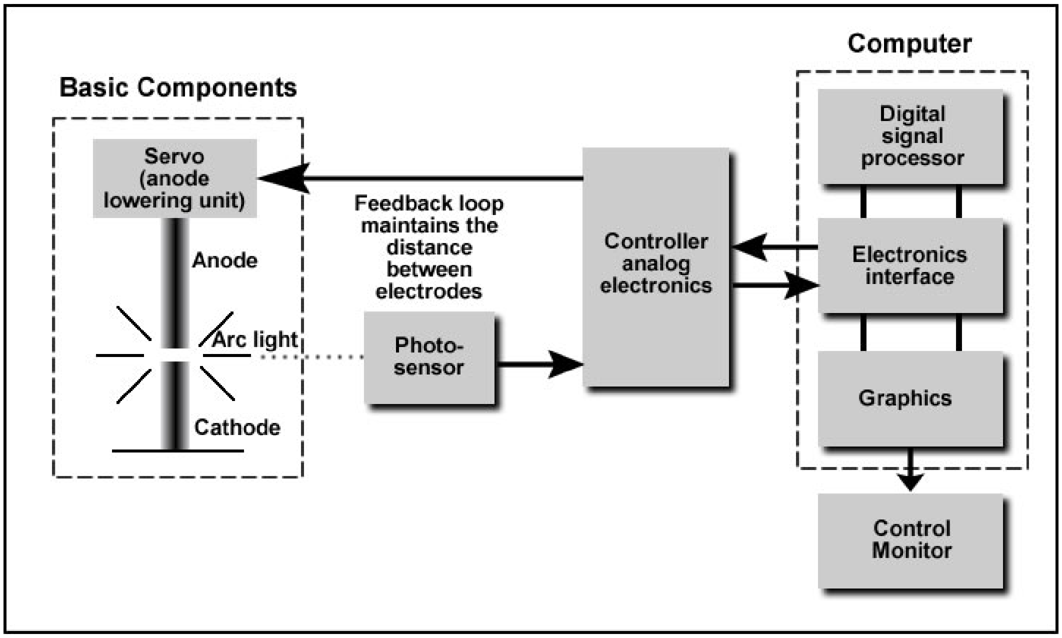

Fig. 3.3: Block diagram showing the concept and major components for the optoelectronic feedback control of the electrode feeding system that is implemented in the present ADS process

A program was implemented to communicate to the integrated circuit of the BASIC stamp via a computing unit. The language of the program is a derivative of BASIC. A program was written on a WINDOWS-based computer using the BASIC Stamp program as an editor. The program was then transferred to the integrated circuit of the analogue controller unit from the computer through a COM 1 serial link. The feedback information from the analogue controller unit feeds to the computer through the same serial link. The information is immediately directed to the WINDOWS program that interprets the data. Such a program allows direct user input. Throughout this process the digital processor handles the necessary computations to run the system. The graphics can be used to plot the data in real-time as well as post-synthesis.

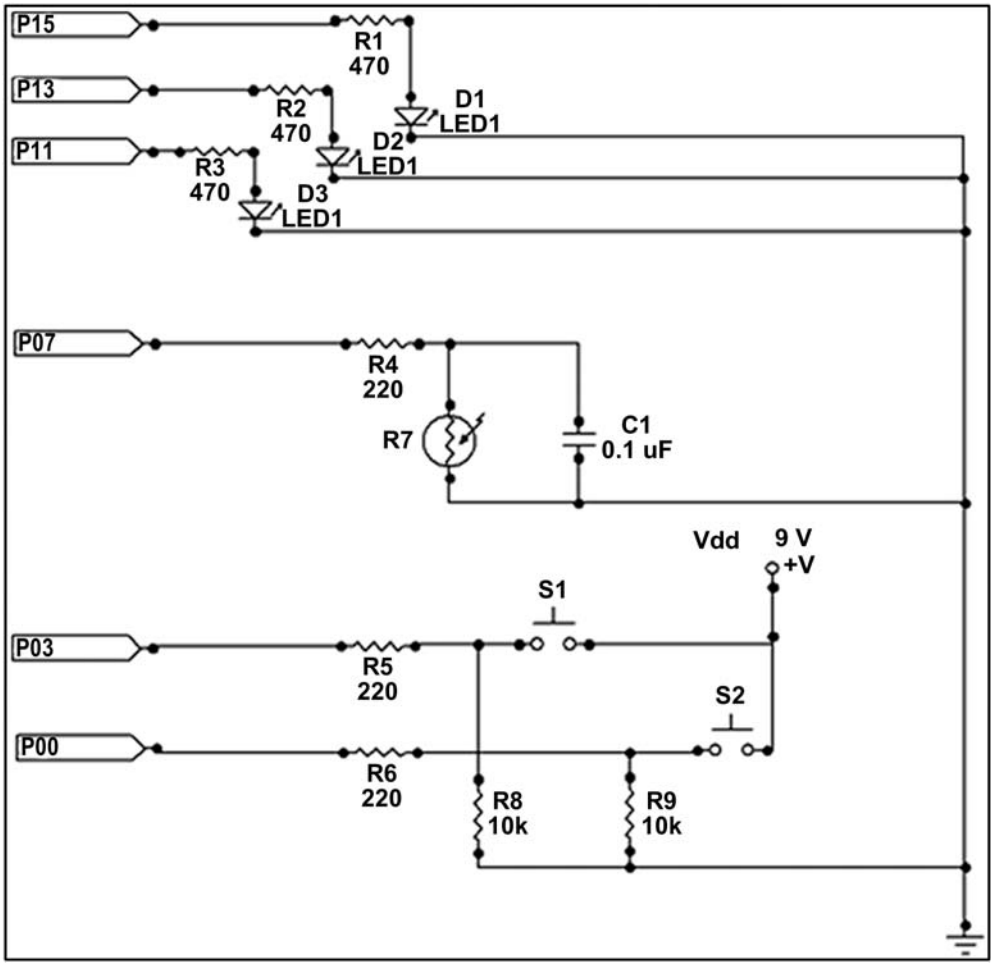

Fig. 3.4: Integrated circuit of controller analogue electronics. R: resistor, C: capacitor, LED: light emitting diode, S: switches, P: input pins

3.2.3. Logic of Automation

The program consists of a few main blocks including initialization and a feedback loop. A flow-chart diagram of the program is shown in *Fig. 3.5*. During initialization of the program, the green LED is switched on, setting the initial *X*, *Y* and *Z* position specified by the user. The feedback loop can be activated when the START button is pressed on the circuit board. The feedback loop moves the *Z*-translational lever arm down through a very precise movement of the servo. The feedback loop is also preceded by a check of the current signal from the photosensor. The servo continues downward until it gets a feedback from the photosensor. When the distance between the two electrodes is approximately 1 *mm*, the arc discharge starts simultaneously sending a signal to the feedback loop from the photosensor. The program is optimized to account for any inconsistency of the servo and intrinsic instabilities created by the arc. The loop constantly checks the feedback reading from the photosensor. When the arc is diminished, the value of the photosensor signal increases, and the feedback loop activates the servo to drive the *Z*-translational lever towards the cathode, thereby maintaining the electrode gap constant.

3.3. Synthesis of Carbon Nanostructures in Water

The synthesis of CNTs was carried out in the cell containing the de-ionized water. The resistance of the de-ionized water used in the present investigation was greater than 10 *MΩ*. Two graphite electrodes with diameter of 6.15 *mm*, acting as a cathode and an anode, were immersed ~ 1 *cm* in water inside the cell at ~ 760 *Torr*. A direct current power supply (model: Dual Mig 131/2 by *Chicago Electric*), was connected to the graphite electrodes. The electrodes were brought in contact to strike an arc. They were separated immediately to a distance of about 1 mm to sustain the arc inside the solution. The synthesis was carried out at a constant open circuit potential of 28 *V* throughout the experiment, while four different values of direct current were used: 25, 35, 50 and 75 *A*. The samples were collected from the upper water meniscus for characterization. The samples were filtered using *Fisherbrand* filter paper of diameter 18.5 *cm*. and a pore size of 1-5 μm.

Sixty production runs were performed for this parametric study for four direct current variables. An open circuit potential of 28 *V* was used for all these measurements. To study the consumption of the electrode during arc-discharge in the water, the weights of the electrodes were monitored before and after each run. For a particular value of current, a set of five runs was carried out. Such five runs are typically: 2, 2, 2, 2 and 1 *min*. The average time gap between two runs in a set is 1 *min*. Three sets of experiments were carried out at a particular value of current to minimize the statistical error. The initial weight of the anode was measured before carrying out each experiment. After each run, the loss of the weight of the anode was measured after drying off the anode. Average values of loss of anode mass for each timed run were calculated from the values of three data sets. These average values were plotted against time.

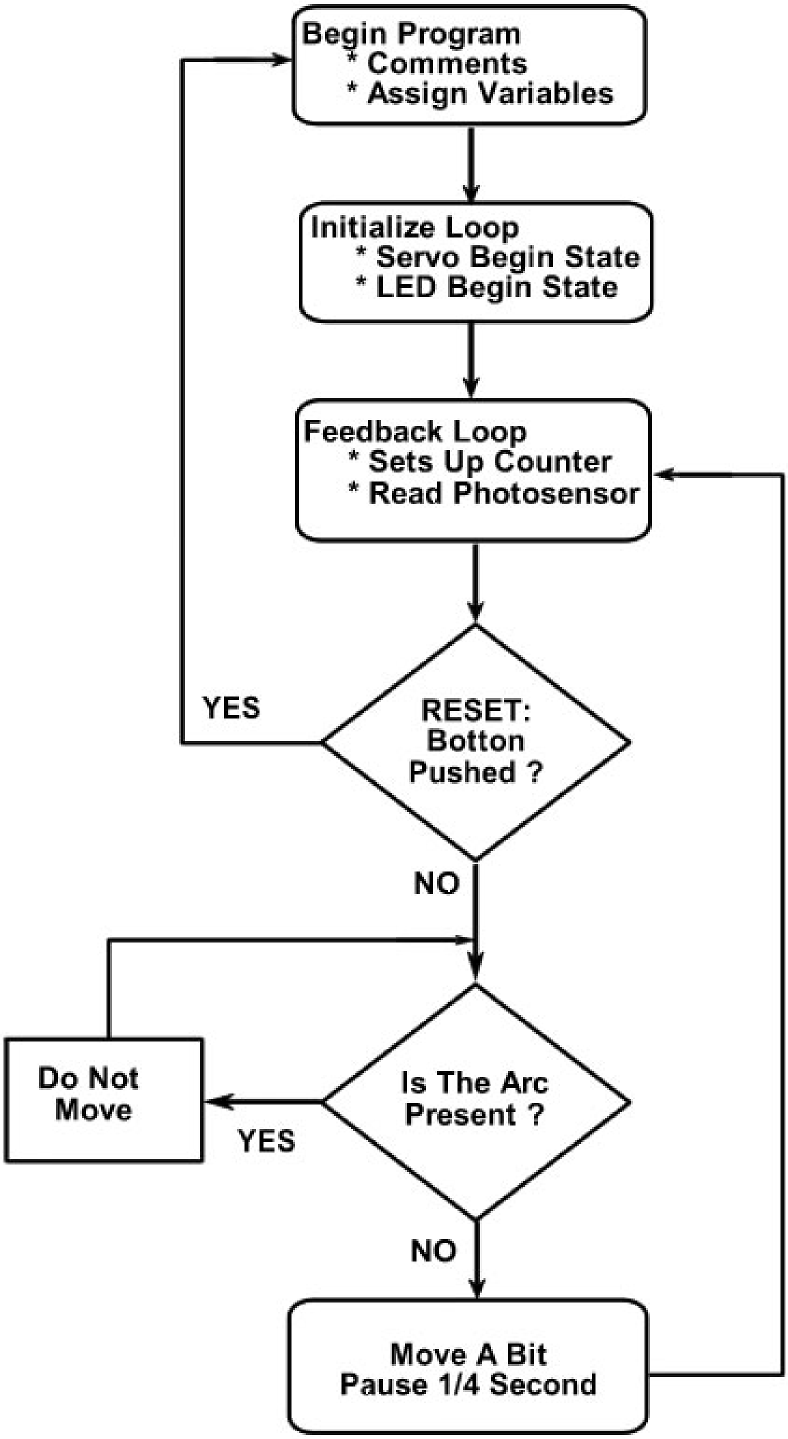

Fig. 3.5 : The flow-chart of the program for the integrated circuit of BASIC stamp for constant electrode-feeding to maintain the arc in the ADS process

3.4. Synthesis of Carbon Nanostructures in Solution (ADS)

The synthesis of CNTs decorated with nanoparticles, such as palladium, nickel, silica, and ceria, was carried out in the precursor solution. For the synthesis of CNTs decorated with palladium nanoparticles, an aqueous solution of 2.087 *mM* concentration was prepared by dissolving palladium chloride as the precursor in de-ionized water (specific resistance of 10 *MΩ.cm*). In order to ensure complete dissolution of the palladium chloride, hydrochloric acid was added to reach 0.1 *M* concentration in the solution. CNTs decorated with palladium nanoparticles were synthesized in the cell with graphite electrodes of diameter 6.15 *mm* immersed in the $PdCl_2$ solution. As mentioned before, a direct current power supply was connected to the graphite electrodes. The electrodes were brought in contact to strike an arc and the electrodes were separated immediately to a distance of about 1 *mm* to sustain the arc ~ 1 *cm* inside the solution. The synthesis was carried out at an open circuit potential of 28 *V* with direct currents of 75, 50, 35 and 25 *A*. The CNTs decorated with nanoparticles were collected from the solution for characterization.

To study the consumption of the electrode during the arc-discharge in the solution, the weight and the length of the electrodes were monitored throughout the experiment during the synthesis of CNTs decorated with palladium nanoparticles. The initial weights of the two electrodes were recorded after drying them inside the furnace at 150 º*C* for 1 *h*. The weight differences were measured every two minutes after drying off the electrode in the furnace for 30 *min* at 150 º*C*. The evaporation rate of the solution had also been followed by measuring the volume of the solution after cooling down to room temperature.

3.5. Purification by Oxidation

As-synthesized CNTs are invariably accompanied by carbon nanostructures and amorphous carbon. There are few methods available to remove unwanted nanostructures and amorphous carbon. In the present research, two methods were used to purify the CNTs: thermal purification and chemical purification. Experimental details of these processes are given in the following sections.

3.5.1. Thermal Oxidation

The concept of thermal purification is based on the idea that the defect-rich nanoparticles and structures oxidize readily compared to the defect-free nanostructures. In this investigation, as-synthesized carbon nanostructures were oxidized isothermally in dry air at 500 °*C*. The temperature chosen was reasonably efficient but not a severe oxidation temperature for polyaromatic carbon. The oxidation kinetics was measured continuously in a thermogravimetry set-up consisting of a microbalance (Sartorious, Model LA230P; ±0.01 *mg*), a vertical customized furnace with temperature controlling accessories, and a computer for continuous data acquisition. The data acquisition was performed every 20 *s*. The temperature was first elevated to 500 °*C* and the sample was introduced into the furnace for isothermal oxidation of amorphous carbon and defective carbon nanostructures. The oxidation is described by *Eq. 3.4*.

$$C + O_2(g) = CO_2(g) + \Delta \qquad (Eq\ 3.4)$$

3.5.2. Chemical Oxidation

Purification by chemical oxidation is nothing but oxidation of amorphous carbon with the treatment of an oxidizing agent. Various types of oxidizing agents are used for oxidation, such as, H_2O_2, H_2SO_4, and HNO_3. In the present investigation, 30 *wt%* H_2O_2 was used for oxidation of amorphous carbon. Such oxidative treatment was carried out using 20 *ml* of H_2O_2 taken in a 50 *ml* of beaker. The unpurified CNTs and H_2O_2 mixture was kept in a dark environment for 24 *hrs* at 20±2 º*C*. Oxidation of amorphous carbon was carried out as in *Eq. 3.5*. Then the liquid was dried at 100 º*C* in a furnace and the purified CNTs were collected from the beaker. Differences in weights, before and after treatment, were noted for a percent loss calculation.

$$C + H_2O_2 \rightarrow CO_2(g) + H_2(g) \qquad (Eq\ 3.5)$$

3.6. Characterization Methods

This section gives a review on the major instruments used as part of this research. The descriptions are intended to give insights into the benefit to the specific applications. As-synthesized and post-treated samples were analyzed by the following characterization techniques.

3.6.1. Scanning Electron Microscopy (SEM)

The SEM provides high-magnification images of solid materials with a high focal depth. In this research, a JEOL 5400 SEM with a cold cathode field emission gun (FEG) system was used. The FEG source yields up to a five orders of magnitude higher in brightness than conventional thermionic tungsten or lanthanum hexa-boride (LaB_6) guns. Elements, as light as B, can be detected to ~ 1 *wt.%* with the EDAX system for energy dispersive spectroscopic (EDS) analysis. This instrument is capable of capturing digital image. It has an EDAX system for electron backscattered diffraction (EBSD), orientation imaging microscopy (OIM) analysis. In the present investigation, the CNTs and the morphologies of the electrodes were characterized using a range of accelerating voltages of 4-15 *kV*.

3.6.2. High-resolution Transmission Electron Microscopy

High-resolution transmission electron microscopy (HRTEM) and scanning transmission electron microscopy (STEM) studies were carried out, using a FEI Tecnai F30 at 300 *kV*, to investigate the size and structure of the CNTs and the CNTs decorated with nanoparticles. The FEI Tecnai F30 is an analytical electron microscope (AEM) which can function as a conventional transmission electron microscope or a scanning transmission electron microscope. It has a field emission gun (FEG) and a multiscan CCD camera for digital imaging. It can operate up to an accelerated voltage of 300 *kV*. It includes both an energy dispersive x-ray detector for energy dispersive x-ray spectroscopy (EDS) and an electron energy loss spectrometer (EELS) for elemental analysis. Most of the investigations were carried out at an accelerating voltage of 300 *kV*. The spot size can be reduced to 0.3 *nm* for the chemical analysis and microdiffraction studies.

In the present investigation, TEM samples were prepared by deposition of a drop of nanomaterials dispersed in acetone onto the TEM grid. Such solution was prepared by dispersing the nanostructured materials in acetone followed by ultra-sonication for 5 *min*. The holy carbon films on copper (300 *mesh*) grids were [Quantifoil®, *SPI*] used throughout the investigation. Selected area electron diffraction (SAED) pattern of the Pd nanoparticles were collected for crystallographic information. For elemental analysis, the energy dispersive spectroscopy (EDS) system attached to the TEM was used.

3.6.3. X-ray Photoelectron Spectroscopy

X-ray photoelectron spectroscopy (XPS) is also referred as electron spectroscopy for chemical analysis (ESCA). This spectroscopic technique provides data on the chemical state and concentration information of the sample surface. The sampling depth for XPS is typically 5 *nm* or less.

In this study, the XPS analysis was performed on a *Perkin-Elmer* PHI 5400 system at a pressure of about 10^{-9} *Torr*. Non-monochromatic Mg-Kα X-radiation with energy 1253.6 *eV* was generated using a power of 300 *Watt* and 15 *kV*. To achieve the maximum resolution, both survey and individual high-resolution XPS spectra were recorded with pass energies of 44.75 *eV* and 35.95 *eV*, respectively. The spectrometer was calibrated using a metallic gold standard (*Au*

$4f^{7/2}$ = 84.0 ±0.1 *eV*). Any charging shifts produced by the specimens were removed by using a binding energy scale referenced[110] to that of *C(1s)* of the adventitious carbon line at 284.6 eV.

Individual peaks were deconvoluted using specialized peak fitting software. Before each peak was deconvoluted, the raw data were smoothed using a *Savitzky-Goley* algorithm. This is a time domain procedure that fits a fourth order polynomial in a moving window of a sizable number of data points. Once the data were smoothed a linear baseline was taken. A *Gaussian-Lorentzian* sum function was used to fit the individual peaks in the deconvolution.

3.6.4. X-ray Diffraction Studies

X-ray diffraction (XRD) analysis was carried out on the sample using a *Rigaku*, (Model: D/B max) X-ray diffractometer with a *Cu-Kα* (0.154 *nm*) monochromatic radiation and optimized operating conditions of 30 *mA* and 30 *kV*. All analyses were carried out at room temperature, scanning from 20º-90º in 2θ. The scanning rate was $1.8^{\circ}.min^{-1}$ with a step size of data collection of 0.05º. The powder was evenly spread out on a double-faced adhesive tape and placed on the sample holder. The holder was then inserted into the chamber for the angular distribution of X-ray diffraction (XRD) peaks. The acquired patterns were matched with a corresponding standard file using the *Jade* software.

3.6.5. BET Analysis

The physisorption (physical adsorption) and chemisorption (chemical adsorption) of inert and reactive gases on the solid surface are of high interest to many applications. In physisorption a relatively weak *Van der Waal's* type interaction between the solid and adsorbed gas molecules, multilayers of adsorbate can result akin to condensation of vapor on the solid surface. Chemisorption involves relatively strong chemical bonding between the solid and the adsorbate and is therefore limited to monolayer coverage. Although any gas will physically adsorb on any solid at appropriate temperature and pressures, chemisorption can only occur with certain gases. In the temperature controlled reactions, the physics and chemistry of reactions can be determined after BET data analysis. A *Brunauer-Emmett-Teller* (BET)[111] adsorption isotherm instrument is commonly employed for adsorption and desorption behavior of gases on the surfaces. The following equation (*Eq. 3.6*) is used to analyze the adsorption, desorption and surface area measurements.

$$\frac{P}{N(P_0 - P)} = \frac{1}{N_m C} + \frac{(C-1)P}{N_m C P_0} \qquad \textit{Eq. 3.6}$$

where P is the adsorbed gas pressure and P_0 the saturation gas pressure of the adsorbate gas at the system temperature. N and N_m are the amount of gas adsorbed in equilibrium and in the monolayer respectively. C is a constant which depends on the solid-gas system.

In the present research, physisorption was employed for the analysis of surface area measurements using a BET Sorptometer (Model: BET 201-A; *Porous Materials Inc.*). For surface area measurements, few milligrams of nanostructured materials were taken in a quart

‘U’-tube. The sample was outgased at 200º *C* and 20 *microns* vacuum for 30 *min*. Ultra-high purity nitrogen gas was used as adsorbate. The gas condensation pressure (P_0) was measured using a small-bulb tube, often called P_0 tube. The adsorption of nitrogen gas on the sample in the ‘U’-tube was measured for different pressures (P) at testing temperature -195.76 º*C*. Finally, the extent of nitrogen-gas adsorption vs. P/P_0 was plotted for the surface area calculation using *Eq. 3.6*. A standard reference sample, a silica-alumina powder, (*NIST,* reference: 1897) with a surface area of 258±5.29 $m^2.g^{-1}$ was used before the measurement to ensure the reproducibility of the BET spectrometer.

Using the BET Sorptometer, chemisorptions of the hydrogen gas were investigated on the palladium nanoparticles decorated on CNTs. A high-purity hydrogen gas was used to determine the adsorption and desorption behavior of hydrogen at different temperatures. Prior to the test, the sample was outgased to 20 *microns* vacuum at 200 º*C* for 30 *min*. The testing temperatures were 25 º, 30 º and 40 º*C*.

3.6.6. Ultraviolet Visible Spectroscopic Study

Ultraviolet visible (UV-Vis) spectroscopy is a very useful technique to study the chemistry of a solution. The absorbance of a solution increases as molecules in the solution absorb ultraviolet or visible light. Consequently, the attenuation of the incident beam of light increases. The absorbance, A, is directly proportional to the path length, b, and the concentration of the solution, c. According to *Beer’s* law:

$$A = \varepsilon bc \qquad \text{Eq. 3.7}$$

where, ε is a proportionality constant, called absorbtivity.

Different molecules absorb at different wavelengths of the UV or Visible light. An absorption band shows the specific wavelength for particular molecule. Depending on the height of the absorption peak, the concentration can be calculated using *Eq. 3.7*.

In this study, an ultraviolet-visible (UV-Vis) spectrometer was used to examine the chemistry of the aqueous solution of 2.087 *mM* $PdCl_2$ with 0.1 *M* hydrochloric acid. Such aqueous solution was used to decorate the CNTs with palladium nanoparticles. The Absorption measurements were made with a *Varian* spectrometer (model: Cary 1E) using a quartz cuvette.

The fitting of peaks was carried out according to the procedure mentioned previously. The software *Peak-fit*® was used for this purpose.

CHAPTER 4: RESULTS AND DISCUSSIONS

In the arc-discharge in water method, the anode and the cathode are brought in contact to strike an arc. They are separated to a distance of about 1 *mm* to sustain the arc inside the liquid for the approximate voltage of 20 *V*. The distance can be calculated from *Eq. 4.1*. If distance between the two electrodes and the potential difference are measured from the boundary of the cathode drop furthest from the cathode, the *Poisson's* equation[112] gives *Eq. 4.1*.

$$\frac{d^2V}{dx^2} = -4\pi\rho = -4\pi\left(\frac{j}{v} - \frac{i}{u}\right) \qquad \textit{Eq. 4.1}$$

where, j and i are the current density carried by the positive ions and electrons respectively, and u and v are the velocities of the positive carbon ions and electrons. It is assumed that the whole cathode drop occurs within one mean free path (ρ). V is the applied potential and x is the distance between the two electrodes.

In an arc, the current density at that portion of the cathode is normally of the order of hundreds of $A.cm^{-2}$ and the cathode drop[112] is of the order of 10 *V*. The temperature at the anode edge is greater[30] than 3000 °*C* while it is 100 °*C* at the solution-vapor interface. Hence, the plasma region produced by the arc adjacent to the electrodes is enveloped by a liquid-vapor interface. The heat transfer from the plasma to bulk water in the ADS system depends on the distance of the two electrodes, the rate of heat transfer through radiation, conduction, convection, temperature of the plasma and few other parameters[30].

There is a substantial thermal gradient across the plasma region. A schematic representation of the two layers at the anode edge is shown in *Fig. 4.1*. The first layer is the *Knudsen* layer[113], which is a kinetic nonequilibrium layer. This layer is attached to the anode surface. Second layer is the hydrodynamic nonequilibrium layer where the electron and the carbon particle temperature differ. The volume of the plasma region depends on the distance between the cathode and the anode. Arcing results in consumption of the anode and the simultaneous deposition of the carbon nanostructures on the cathode. The amount of CNTs synthesized from the anode depends not only on the volume of the plasma, but also on the relative distance between two electrodes, the overall current density and applied voltage across the electrodes during ADS process. An optimization of all these parameters is very important for the overall system performance as described in later sections.

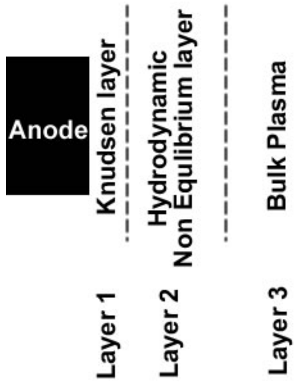

Fig. 4.1: Schematic representation of layers near the anode edge

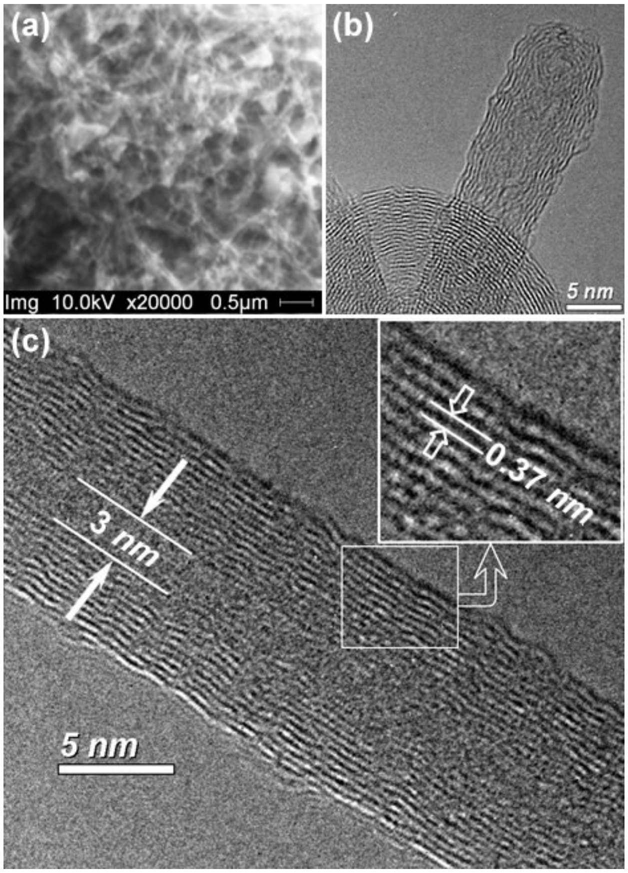

Fig. 4.2 : (a) SEM micrograph of CNTs; (b) HRTEM micrograph of graphitized and ungraphitized CNTs (c) HRTEM micrograph of a CNT; inset: the inter-layer distance

4.1. Carbon Nanostructures

During arc-discharge in water, the clusters of CNTs were found to be floating on the water. The surface average diameter of the clusters is more than 10 *μm*. Assuming the temperature at the center of the arc being 3727 °*C*, a rough estimation[30] of the gradient yields 1209 $K.mm^{-1}$ using *Eq. 4.2*. The loss of weight of the electrodes is due to the formation of carbon dioxide, carbon monoxide, CNTs and other carbonaceous materials including dislodged graphene sheets, carbon onions, amorphous carbon and carbon rods. Such carbonaceous materials were formed inside the plasma region at various temperature zones[30]. A high density of

CNTs were observed at the tip of the cathode during SEM investigation when arc discharge was operated at 28 *V*. One such low-magnified micrograph of highly dense CNTs is presented in *Fig. 4.2 (a)*. The micrograph shows the formation of a '*cotton-like*' stacking of nanotubes bundles. *Fig. 4.2(b)* represents a high resolution transmission electron microscopy (HRTEM) micrograph of a CNT along with a hemispherical highly crystalline carbon onion. A HRTEM micrograph of well-crystallized CNT is presented in *Fig. 4.2(c)*. The inner and outer diameters of a CNT as shown in the HRTEM micrograph of *Fig. 4.2(c)* are 3 and 10 *nm*, respectively. The inset picture of *Fig. 4.2(c)* shows that the distance between the two concentric walls is 0.359 *nm*. Such distance of the inter-wall spacing supports literature data[114]. The reported[115] interlayer spacing of graphite in literature is 0.34 *nm*. The inner diameter of all CNTs synthesized by arc-discharge in water process is typically 3 *nm*. The outer diameter of the CNTs is found to be in the range of 5-15 *nm*. Detailed results from the different characterization methods are given in following subsections.

4.1.1. Other Carbon Nanostructures

CNTs along with other carbonaceous materials including carbon nanohorns, carbon rods, amorphous carbon, carbon onions, nanoporous carbon (NPC), and a few dislodged graphene sheets have been found for the arc-discharge in solution method. The micrographs in *Fig. 4.3* show examples of such different carbon nanostructures which formed during the arc-discharge in de-ionized water. A HRTEM image of a carbon nanohorn is shown in *Fig. 4.3(a)* synthesized during arc-discharge in water. A detailed discussion on structural features of such a carbon nanohorn follows in a later subsection. *Fig. 4.3(b)* shows a HRTEM image of a carbon nanorod. Such a carbon nanorod is very rare for the arc-discharge method in solution. An ample amount of amorphous carbon is found around the CNTs on the holy-carbon TEM grids. Such amorphous carbon is different from the supported amorphous carbon film of the grid. *Fig. 4.3(c)* is showing a micrograph of the amorphous carbon along the edge of a CNT. For as-synthesized samples, the fraction of amorphous carbon is very high. Therefore, the image contrast is very low due to the weak electron scattering of CNTs[116]. *Fig. 4.3(d)* is showing a carbon onion. Such carbon onions are rarely found during the TEM investigation on the sample synthesized by arc discharge in water. However, a large amount of well-crystallized carbon onions was found by others[30] when arc-discharge was carried out in water. Nano porous carbon was also found in this study and is shown in *Fig. 4.3(e)*. A few dislodged graphene sheets were found during TEM analysis. One such dislodged graphene sheet is shown in *Fig. 4.3(f)*.

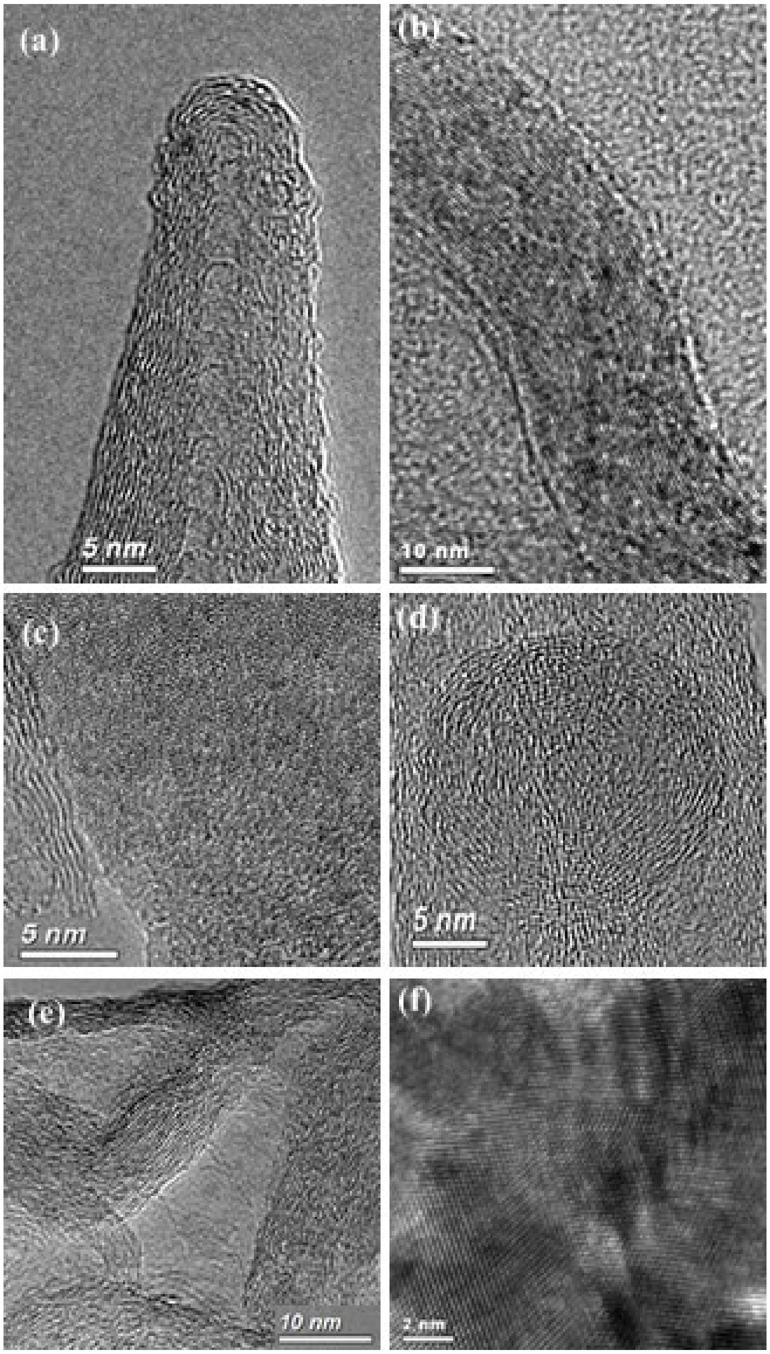

Fig. 4.3 : Various other carbon nanostructures synthesized along with CNTs using ADS method; (a) carbon nanohorn, (b) carbon nanorod, (c) amorphous carbon, (d) carbon onions, (e) nano-porous carbons, (f) dislodged graphene sheets

4.1.2. Defect Structures of CNTs

The main difference between the formation of CNTs during ADS process and the arc-discharge in argon gas at lower pressure is the extent of formation of amorphous carbon. During the ADS process, the rate of formation of amorphous carbon is much higher that for arc-discharge in argon. *Iijima et al.*[117] found no amorphous carbon in the carbon deposit; however, the deposits were composed of pyrolytic graphite. In this study, formation of pyrolytic graphite is found to be less significant compared to arc-discharge in argon. However, like arc discharge in argon at low pressure, we found different shapes and sizes of carbon nanostructures besides the nanostructures as mentioned in *Fig. 4.3*. A variety of tips of CNTs were found in the present study. Unlike arc-discharge in low-pressure argon, the most common tip among many tube-tip shapes observed in TEM study is represented in *Fig. 4.4(a)* a hemispherical cap. The extensive TEM study on as-synthesized samples shows that almost 50 % of the CNTs are not well-graphitized like in *Fig. 4.4(a)*. High-quality lattice-resolution micrographs of CNTs are rare for some of the CNTs produced by arc-discharge in water owing to the poor perfection of the atomic arrangement. Such imperfection was also reported by others[96,118]. It was also found that such nongraphitized CNTs are always associated very small bulb-like structures on the outer wall of CNTs. One of such bulbs is marked with an arrow in *Fig. 4.4(a)*.

The second most common tip is the tip of carbon nanohorn. This ice-cream cone type asymmetric tip is made of pentagonal and heptagonal rings. The cone angle of the carbon nanohorn shown in the *Fig. 4.4(b)* is 17º. However, the average cone angle of carbon nanohorns synthesized by ADS process is approximately 18º. This micrograph of the nanohorn (*Fig. 4.4(b)*) shows unevenly spaced lattice fringes with odd numbers of fringes on either side of the central hollow core. It is also interesting to note that the nanohorn in *Fig. 4.4(b)* has some abruptly terminated inner walls. A few of them are shown with arrows. Although such CNT was rarely found in TEM investigation, this would help to understand the growth mechanism of CNT in ADS process. A frequent observation in nanohorns was the presence of an inner wall closure before end capping. Such inner closures are marked in *Fig. 4.4(c)*. During TEM studies, more complicated internal structures were also found. A closed compartment formed inside the carbon nanotubes in *Fig. 4.4(c)* is interesting to observe. Such internal closed compartment is indicated in the rectangular box.

In the TEM studies, the CNTs were often seen to be accompanied by variety of small carbon nanostructures with different shapes. These are called carbon nanoparticles or nanoshells. They were found to be hollow with spherical or oval shapes. *Fig. 4.4(d)* is showing a HRTEM micrograph of a 'paper clip' shaped nanoshell structure with a length of approximately 10 *nm*. The interwall distance is found to be higher (0.37 *nm*) than that of CNTs. It is not entirely clear from the micrograph whether the structures are concentric or scroll structure. It appears from the high resolution micrograph of such nanostructures that lines corresponding to the projections of the graphitic walls of CNTs which are often discontinuous. For such a complicated structure, the presence of the pairs of pentagon and hexagon is expected than other structures. Possible shapes of such structures are either elongated toroidal (or donut) shapes, or helical coil shapes. In the present study, a few more helical structures are found in the TEM investigations. They are described in the '*CNTs Decorated with Nanoparticles*' section of this chapter.

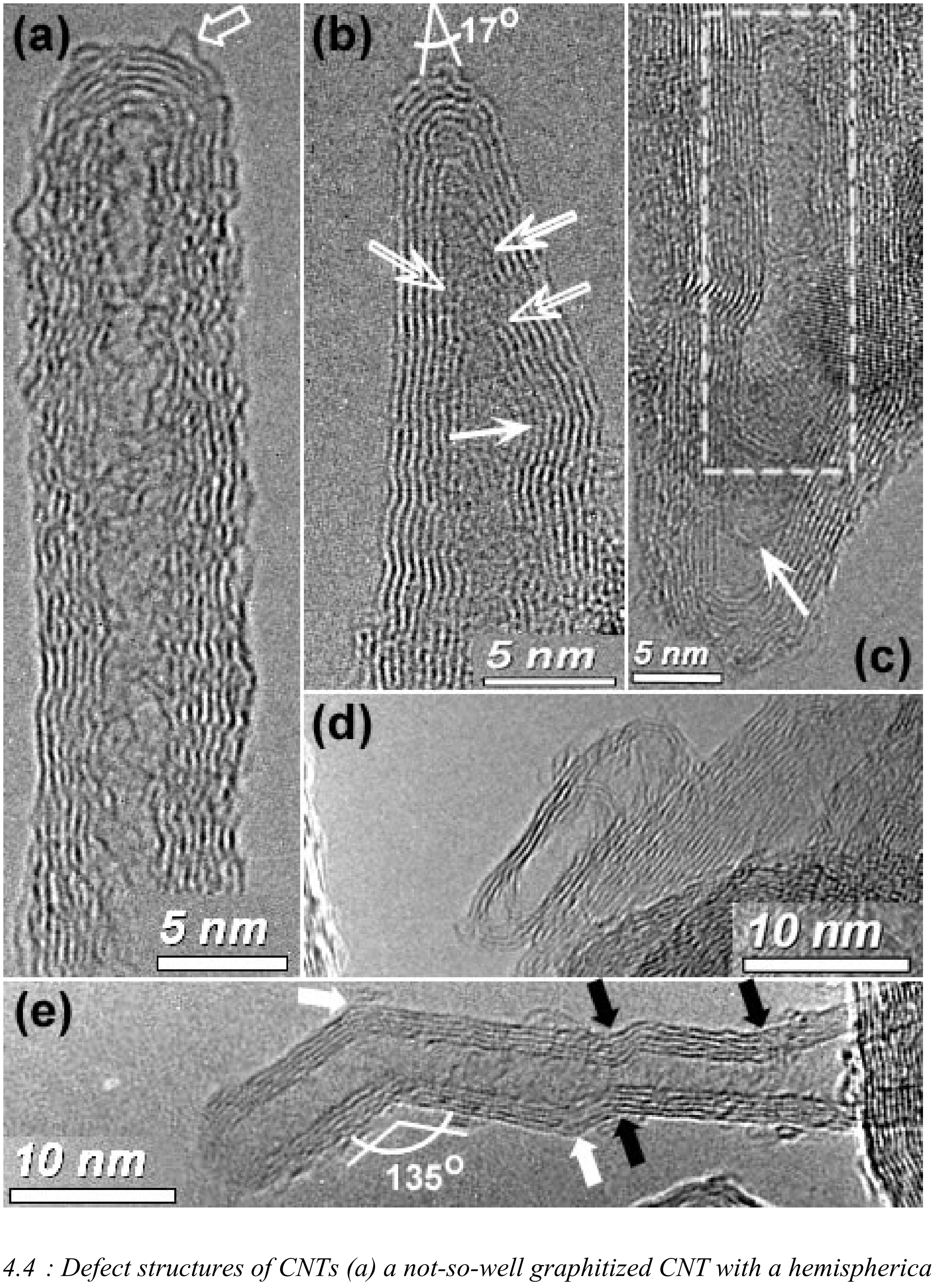

Fig. 4.4 : Defect structures of CNTs (a) a not-so-well graphitized CNT with a hemispherical tip (b) a well graphitized carbon nanohorn, (c) a CNT with complex internal closure, (d) 'carbon nano-clip' -a nanoshell (e) a CNT with several kinks on it

Fig. 4.4(e) shows a HRTEM micrograph of a CNT with several kinks. Such inward and outward kinks are shown with black and white arrows, respectively. The shape of this type of CNTs was found to be very rare in TEM studies. At the junction of the kinks, the lattice fringes appear to curve smoothly, as if the walls are bent without any distortion. According to *Cowley*[119], this appearance probably arises from the selective imaging of layers of graphitic carbon that are parallel to the incident beam and the lack of contrast in HRTEM images from other parts of the specimen. The outward kinks, marked with white arrow in the figure, are believed to result from the presence of a single pentagon at the tip of the kinks[33], however, the inward kinks are formed due to presence of a heptagon at the tip of the kink. The angles, measured at the point of the kinks in the figure, are almost the same at approximately 135º. It is worth mentioning that the measurement of the exact angle from micrograph will not always be the actual angle at the kink, because it is almost impossible to know if the tube axis was precisely perpendicular to the electron beam. However, the angle at such type of kink[33] was found in the literature to be 150º.

4.1.3. XRD Data Analysis of CNTs

The XRD spectrum, presented in *Fig. 4.5*, of the CNTs shows (002) and (004) reflections which can be assigned to the hexagonal ring structure of graphite sheets forming the CNTs. All the peaks are slightly shifted to lower angles from that of graphite indicating the wider interlayer spacing. The sharp and high intensity peak (002) for CNTs is located at, $2\theta = 26.4^{\circ}$ where as for graphite the (002) peak[120] is at 25.6º. Such shifting of values was also found by others[47]. The shifting of peaks to the lower values is due to the turbostratic structure (two dimensional lattice) of CNTs. No additional peak for other graphitic carbonaceous material was found in this study. However, when CNTs synthesized by other methods[47] and analyzed through XRD, additional peaks for other graphitic carbon materials were found. XRD values are in close agreement with HRTEM analysis, where the interlayer spacing of MWCNTs is found to be 0.359 *nm* [*Fig. 4.2(c)*].

4.1.4. Surface Area Analysis

The extent of adsorbed nitrogen gas on CNTs at different values of P/P_0 values is shown in *Fig. 4.6*. A linear trend line is formatted with regression coefficient 1. From the plot, the slope and intercept of the straight line are found to be 0.0513 $cc.g^{-1}$ and 0.00061 $cc.g^{-1}$, respectively. The BET monolayer volume (V_m) and BET constant (C) are found to be 19.2637 and 85.67, respectively. Using *Eq. 3.6*, the surface area of the sample was calculated to be 83.95±3.5 $m^2.g^{-1}$. This value is higher than the data reported in the literature[121] and corroborates the collection of clean CNTs in the present case. *Tsang et al.*[121] measured the BET surface area of as-synthesized MWCNTs and found the surface area to be 21.0 $m^2.g^{-1}$. Using DC arc-discharge in helium at 100 *Torr* (Voltage = 30 *V*, current 180-200 *A*), they synthesized MWCNTs. *Ajayan*[42] recently reviewed the BET surface area of MWCNTs and reported that the range of BET surface area is approximately 10-20 $m^2.g^{-1}$, which is higher than that of graphite and smaller compared to activated porous carbon.

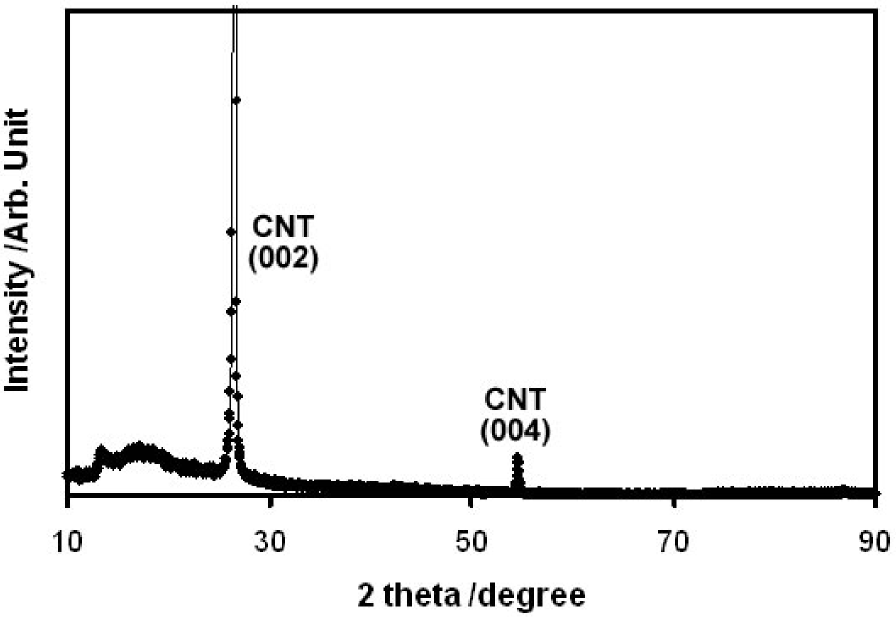

Fig. 4.5 : XRD trace for the pristine CNTs

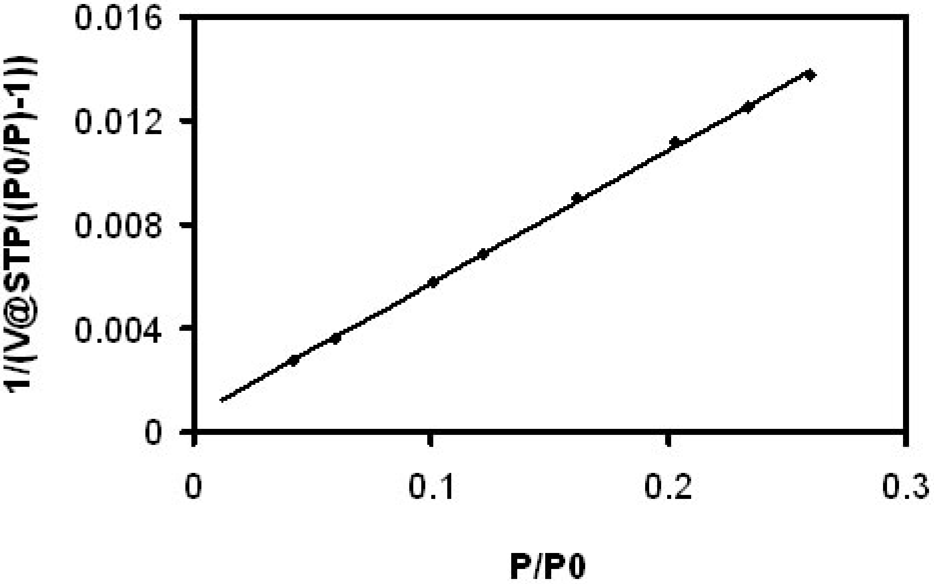

Fig. 4.6: Extent of adsorbed nitrogen gas on CNTs at different P/P0 values for the surface area measurement

The value for SWCNTs is expected to be an order of magnitude higher. Due to the relatively large hollow channels in the center of nanotubes, their density should be very low compared to graphite. Rough estimates suggest that the SWCNT density could be as small as 0.6 $g.cm^{-3}$, and the MWCNT density could range between 1.0 and 2.0 g/cm^3 depending on the constitution of the samples[42].

4.1.5. Purification

Fig. 4.7(a) is a representative of unpurified carbon nanotubes. This low magnified bright-field TEM micrograph shows the presence of a large amount of amorphous carbon around the CNTs. Few carbon soots, hanging in the holes of a holey carbon grid, are indicated with arrows. *Fig. 4.7(b)* represents the HRTEM micrograph of such unpurified carbon nanotubes. The micrograph demonstrates the presence of amorphous carbon on the outside wall of the CNTs. The contrast in *Fig. 4.7(a)* and *(b)* are very weak due to the presence of amorphous carbon around CNTs. Frequently, there are two often encountered situations, when imaging of CNTs is very difficult during TEM investigations: (1) for small tube diameters of CNTs and (2) when CNT is swamped in the amorphous carbon. It is experienced from our present study that when a CNT is buried in amorphous carbon, the scattering from amorphous carbon can easily outshine the contrast from the CNT. Therefore, it is very difficult to identify the CNT in a TEM study. This is illustrated in *Fig. 4.7*. To remove the amorphous carbon from CNT samples, oxidation was carried out in two different ways: air oxidation by heating and chemical oxidation by H_2O_2.

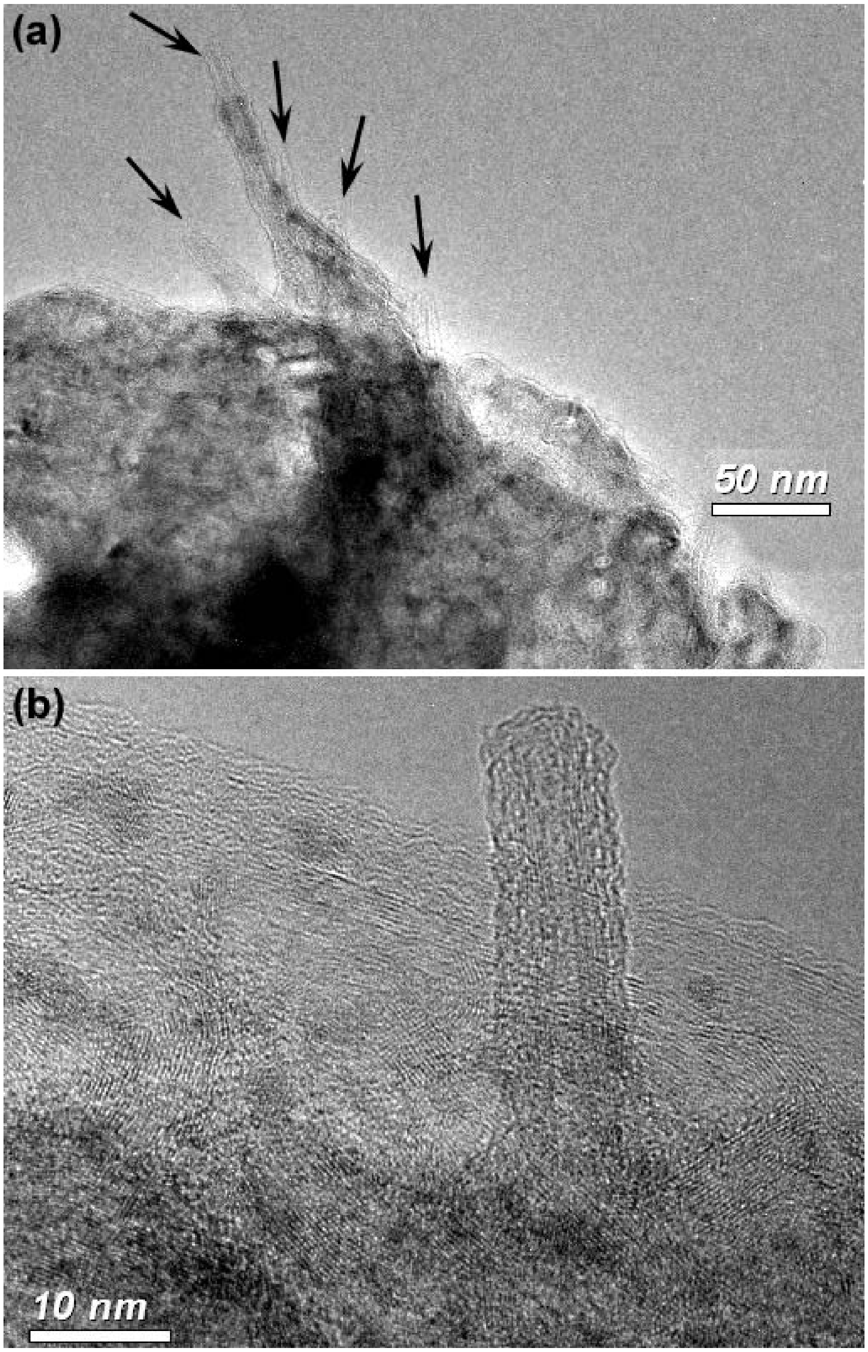

Fig. 4.7: Unpurified product (a) low magnified TEM micrograph of unpurified CNTs (b) HRTEM micrograph of unpurified samples showing amorphous carbon around the CNT

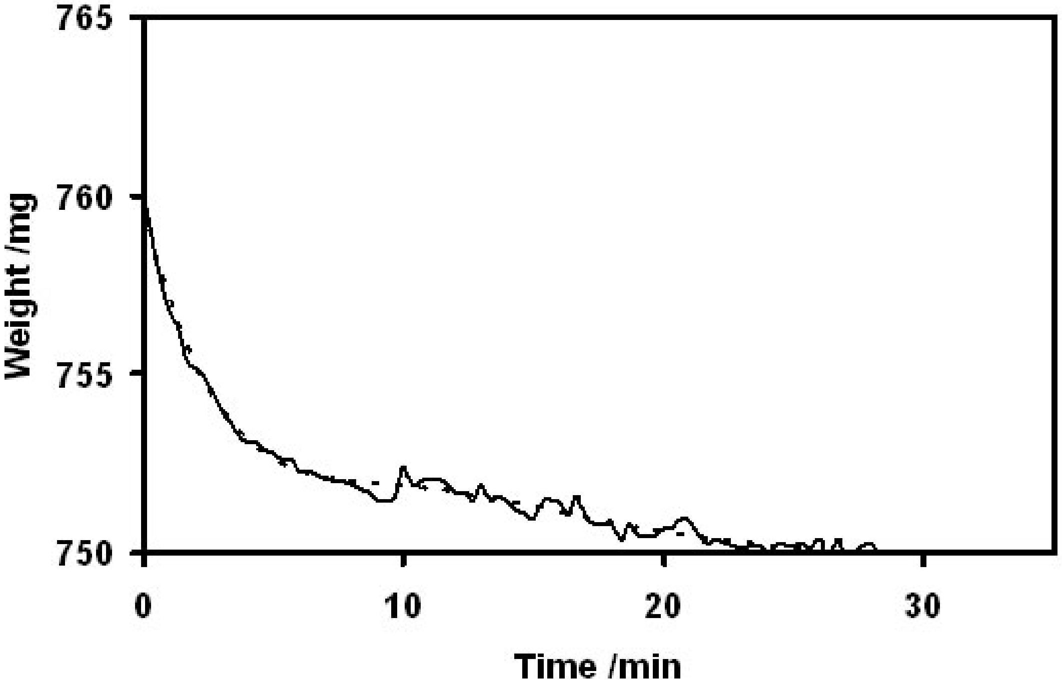

Fig. 4.8: Weight vs. time plot derived from oxidation during purification

Fig. 4.8 represents the weight-time plot derived from the oxidation purification experiment at 500 *°C*. It shows a sharp drop in the weight at the very beginning of the oxidation. This is followed by a nonlinear decrease of the weight as a function of oxidation time. In general, oxidation of amorphous carbon starts with an initial sharp drop due to the reaction between amorphous carbon and oxygen through *Eq. 4.3*. followed by oxidation of other defect-enriched carbon nanostructures. In the present investigation, a similar trend has been observed where the weight quickly dropped to a lower value within 5 *min* of oxidation. It can also be observed, from the *Fig. 4.8*, that only 0.92 *wt%* weight loss has occurred during the air oxidation. The results from the oxidation experiments are presented in the *Table 4.1*.

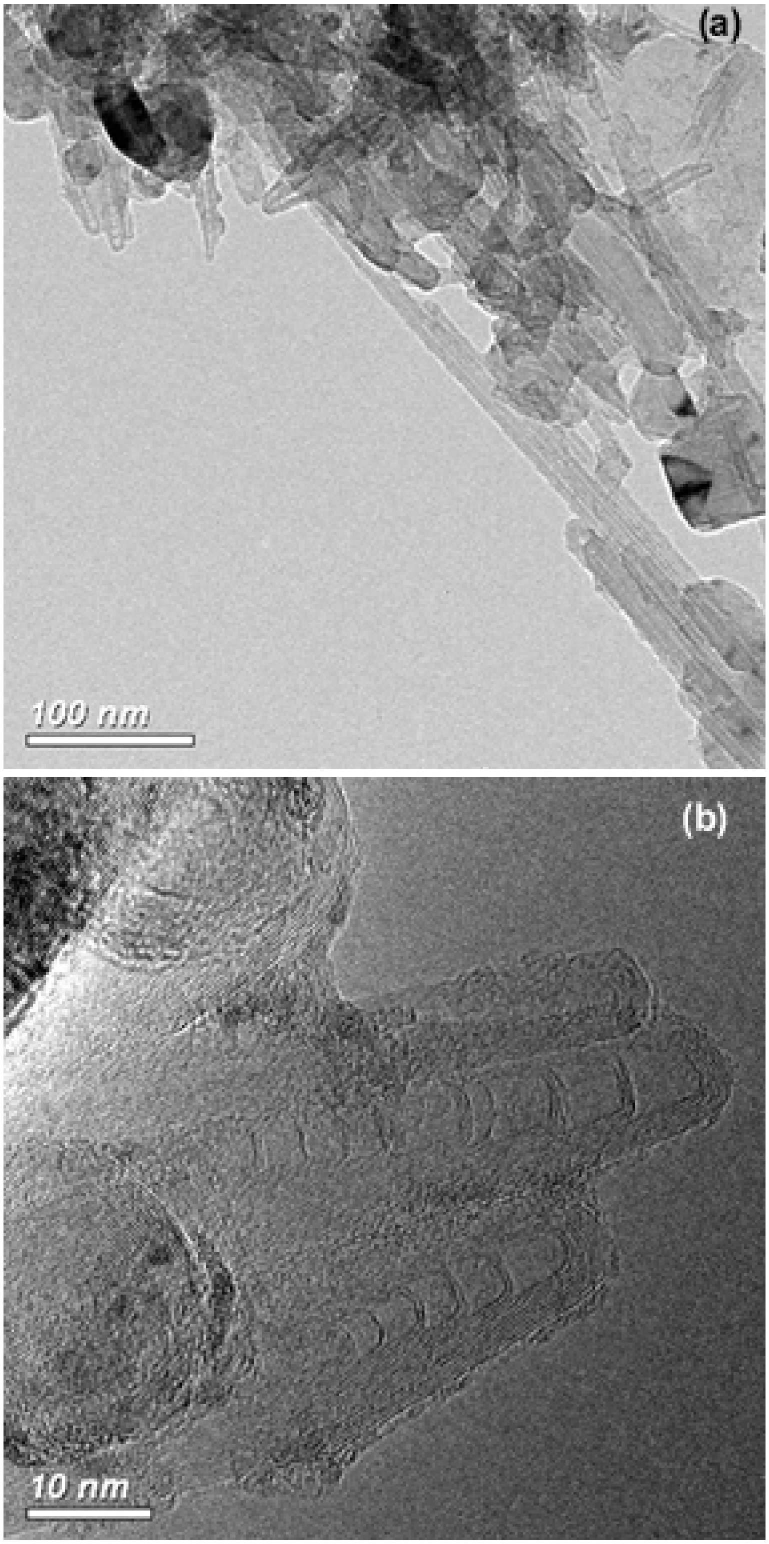

Fig. 4.9: (a) Low resolution (b) high resolution TEM micrograph of purified MWCNTs; Most of the amophous carbon has been removed by oxidation in air at 500 ºC

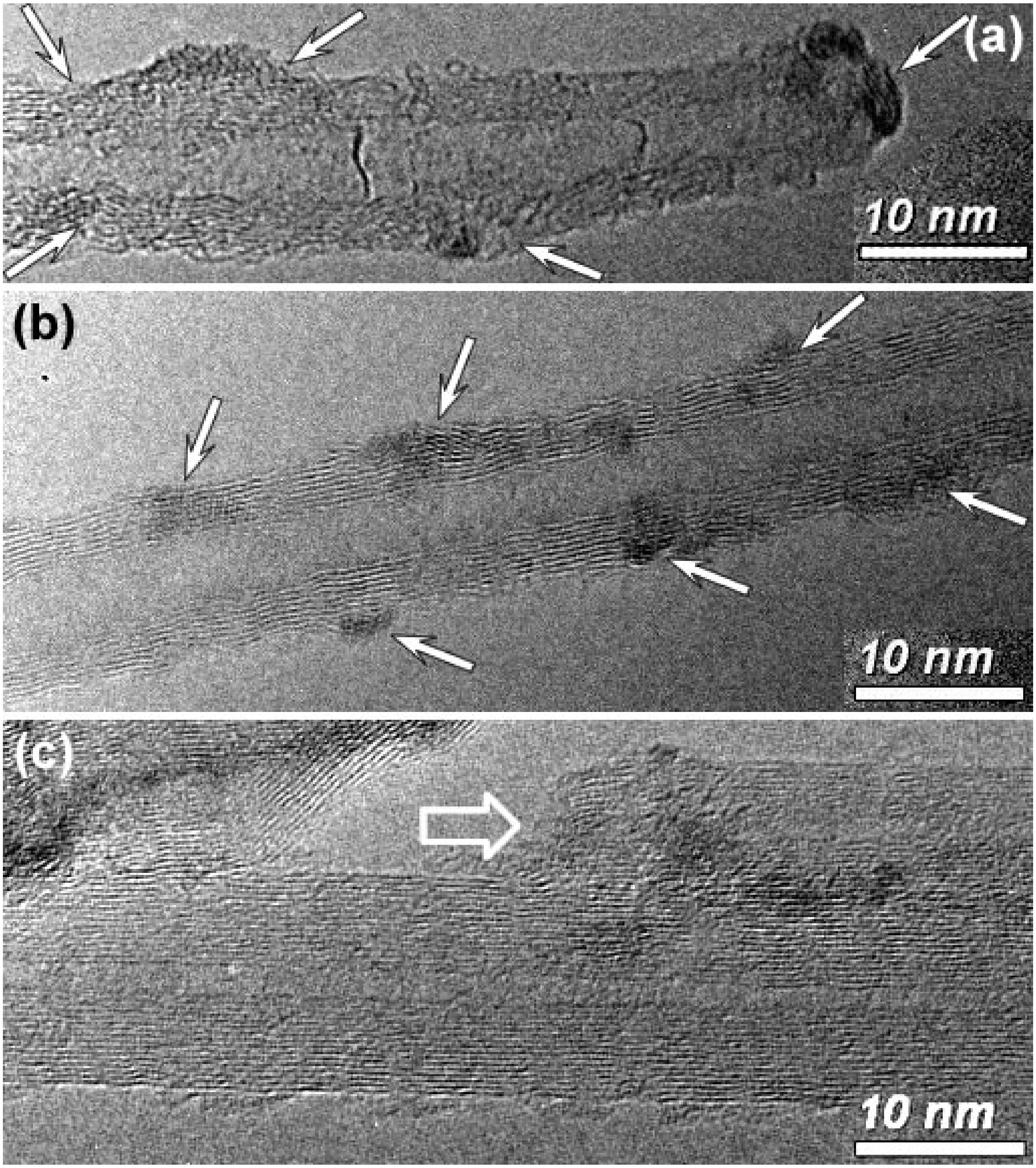

Fig. 4.10: (a) and (b) Chemical oxidation of CNT sample; arrows are showing the points where chemical oxidation had occurred, making pits, necks and deposition of amorphous carbon (c) air oxidation of CNT samples; a few CNTs are open after air oxidation. The arrow is showing the opening of a CNT

Fig. 4.9(a) is low magnification TEM micrograph taken after air oxidation of CNTs for 30 *min*. It is noteworthy that there is almost no amorphous carbon in the sample. A few other carbon nanostructures along with CNTs are clearly visible in *Fig. 4.9(a)*. *Fig. 4.9(b)* is a HRTEM micrograph taken from the air-oxidized sample. This HRTEM micrograph is showing the reduced presence of amorphous carbon. It is worth mentioning that the high-quality lattice resolution TEM micrograph of CNTs can be easily acquired after such a control heating because of graphitization. The presence of nongraphitized, not-well-aligned walls of CNTs is most frequently observed in samples without oxidation.

In another attempt, H_2O_2 was used to purify the CNTs. It is found that the loss of sample is approximately the same. The TEM investigations on the treated sample show that the CNTs are highly pure after chemical oxidation. Amorphous carbon is removed from the sample by the treatment. It can also be noted that the H_2O_2 can also oxidize defect-enriched CNTs. *Fig. 4.10(a)* and *(b)* show that a HRTEM micrograph of a H_2O_2-treated CNT. The arrows in the figures show the oxidation sites on the outer wall of the MWCNT. The nanotube has suffered from corrosion forming pitting, necking and deposition of carbon at various places throughout the length on the nanotube. Such deformations in CNTs were not found when the CNT was treated with air oxidation. The same was also observed by other investigators[121].

Fig. 4.10(c) is a HRTEM micrograph of air-oxidized CNTs. The detailed examination of freshly prepared CNTs showed that the CNTs were invariably capped and that caps could take a wide variety of morphologies. An extensive survey of nanotubes revealed no broken caps. After oxidation in air, it is observed that the caps of a few CNTs are oxidized during air oxidation [shown in *Fig. 4.10(c)*]. It is well-known that the cap is made of five, six and seven membered rings and is more reactive than the other sites.

Table 4.1: Results from high temperature air and chemical oxidations

Oxidation	Air oxidation	H_2O_2 oxidation
Initial weight (*mg*)	760	650
Final weight (*mg*)	752	644
% weight loss	1.05±0.1	0.92±0.1

4.1.6. Parametric Studies

In the parametric study, the change in weight of the electrodes with time and the production rate with each and every runs are monitored to optimize the data related to the production of CNTs. Since the major interest in the parametric study is associated with the optimization of the production rate of CNTs, the weight loss of the anode is discussed in detail. Sixty experimental runs were carried out for the parametric study with varying various parameters.

For four different values of the current, the rate of weight loss of the anode materials has been obtained. The *Figs. 4.11(a), (b), (c)* and *(d)* represent the loss of weight of the anode electrode with time at the operating current of 25 *A*, 35 *A*, 50 *A* and 75 *A*, respectively. Error bars in *Figs. 4.11(a), (b), (c)* and *(d)*, indicate the fluctuations of the rate of weight loss. The error bars are calculated from several experimental runs. *Fig 4.11(a)* shows that the fluctuation of the anode loss is consistent with time. However, for the lower values of current, fluctuations appear to vary with time. There is a slight trend of an increasing error bar with time. This indicates that, at lower values of the current, the production rates of CNTs are varied with time; on the other hand, at higher value of current production rate is much more steady and consistent. In the case of the cathode, the weight gain with time for different current values is shown in *Fig. 4.12*. Like the rate of the anode loss at lower values of current, it is found that the deposition rate of carbonaceous materials on the cathode is not consistent. At 25 *A*, the deposition rate was varied significantly with time (not shown in the figure), however, at 75 *A*, the deposition rate is found to be steady for different runs. It is found that during the experiments, the plasma was much more stable at a higher voltage than at the lower ones, which is the probable reason behind the steady deposition rate onto cathode.

In *Figs 4.11* and *4.12*, the trend lines are formatted using linear regression setting the intercept at zero. It is assumed that the formation of a plasma does not occur at zero voltage, therefore, no change in the weight of electrodes at zero voltage. The weight-change relationships in the abovementioned systems can be mathematically expressed with the following equation (*Eq 4.2*):

$$\Delta W = k \times t \qquad \textit{Eq. 4.2}$$

Where, t is time in minutes and ΔW is the weight change in g during arc-discharge in solution, and k is the kinetic parameter in $g.min^{-1}$.

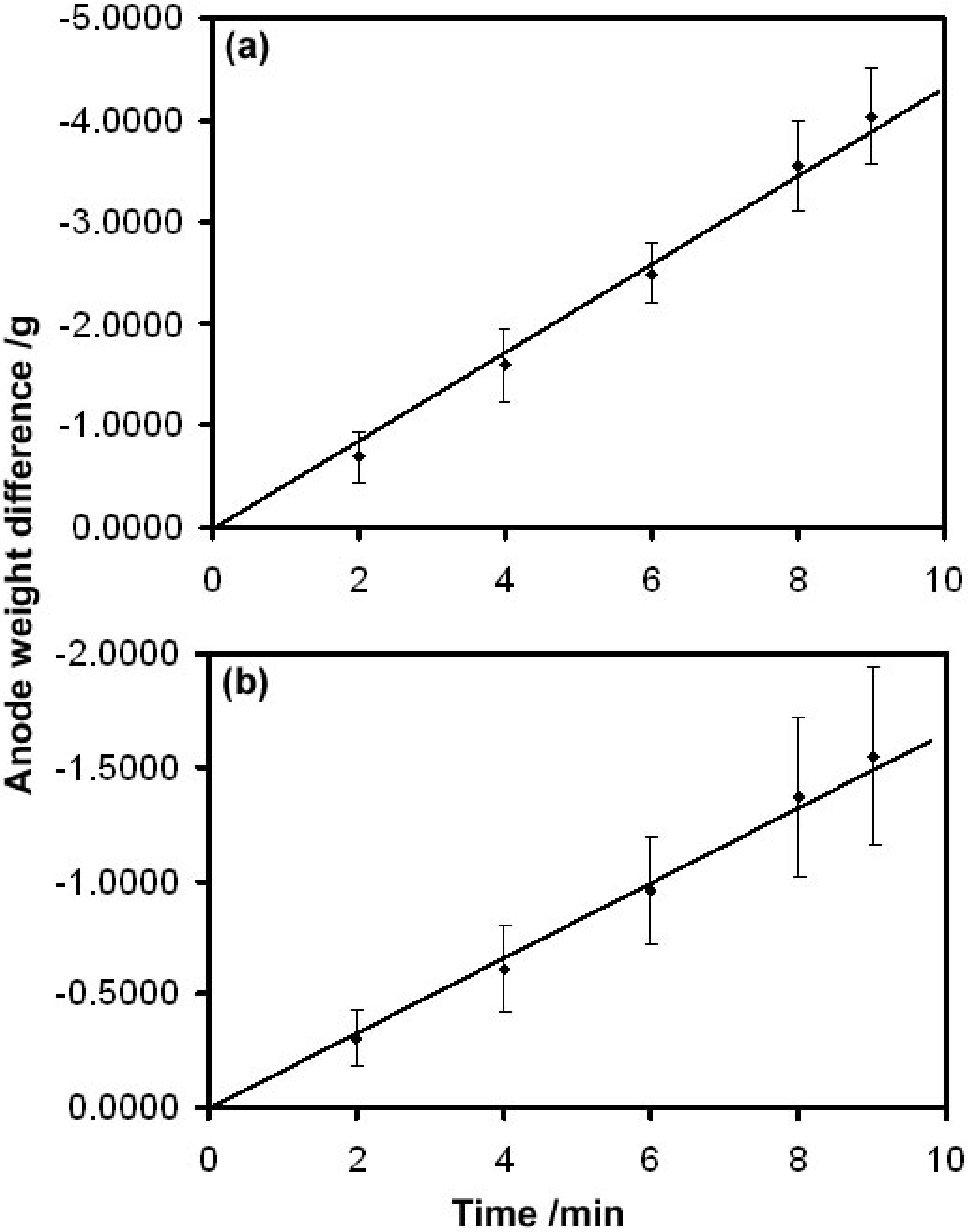

Fig. 4.11: The loss of anode electrode with time for various current; For (a) 75 A, (b) 50 A, (c) 35 A and 25 A. (continued to next page)

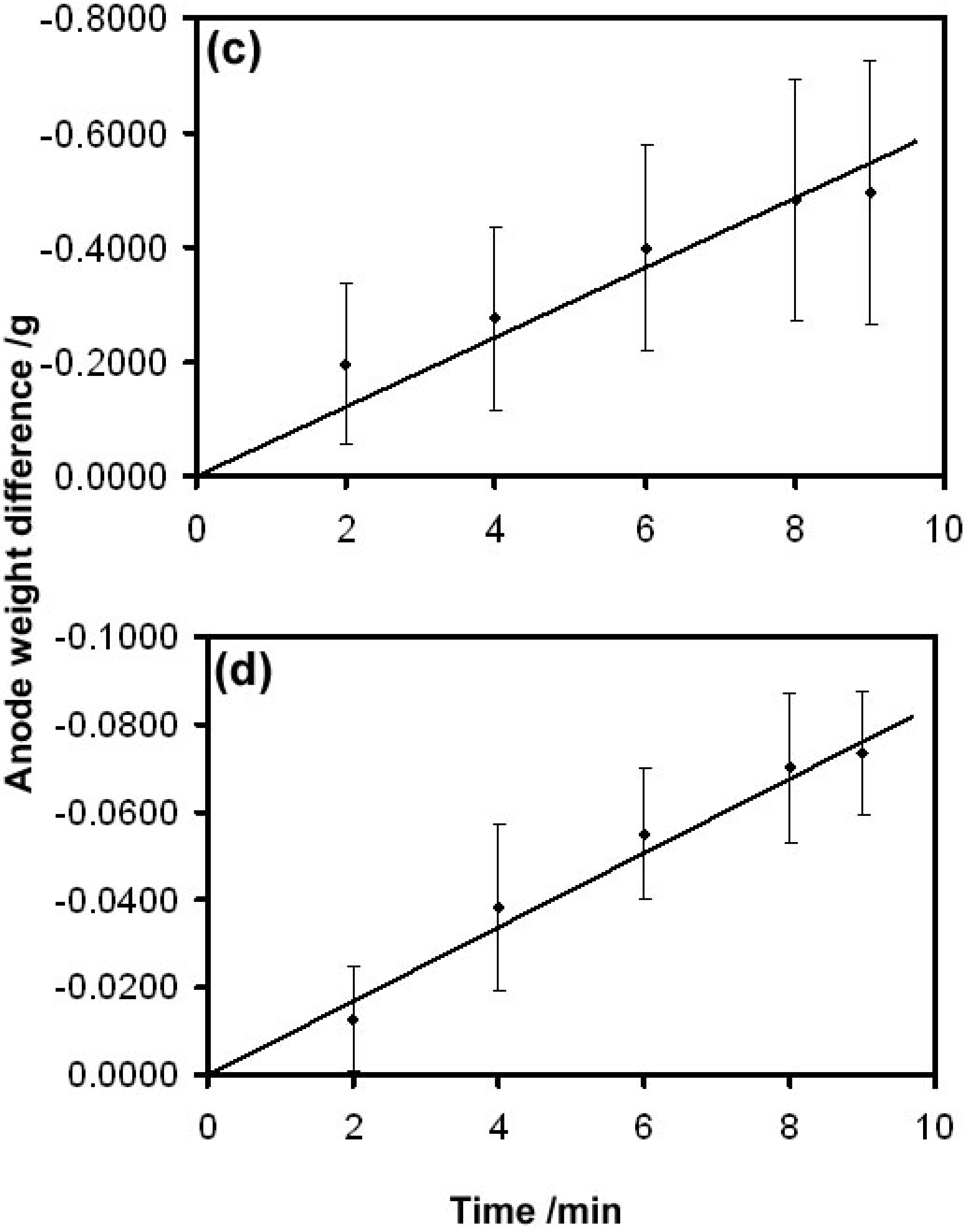

(Continued from previous page) *Fig.4.11: The loss of anode electrode with time for (c) 35 A and (d) 25 A*

The experimental values of k from *Eq 4.2* for anode consumption, cathode gain for their corresponding current values are given in *Table.4.2.* R^2 in the table represents the percent regression coefficients for the corresponding kinetic parameter calculated from the graph.

Table 4.2: Correlation chart of kinetic parameters of electrodes and rate of weight change corresponding current

Current (*A*)			75	50	35	25
Anode	Kinetic parameter k ($g.min^{-1}$)	Value	-0.4351	-0.1676	-0.0606	-0.0086
		R^2 (%)	99.0	99.0	85.0	97.5
	Rate of anode loss ($g.min^{-1}$)	Value	0.4525	0.1731	0.0509	0.0077
		Standard deviation	0.067	0.0201	0.0281	0.0031
Cathode	Kinetic parameter k ($g.min^{-1}$)	Value	0.2398	0.1193	0.0418	0.008
		R^2 (%)	95.0	93.1	90.0	60.0
	Rate of cathode gain ($g.min^{-1}$)	Value	0.090	0.045	0.013	0.0025
		Standard deviation	0.0033	0.0045	0.0019	0.0014

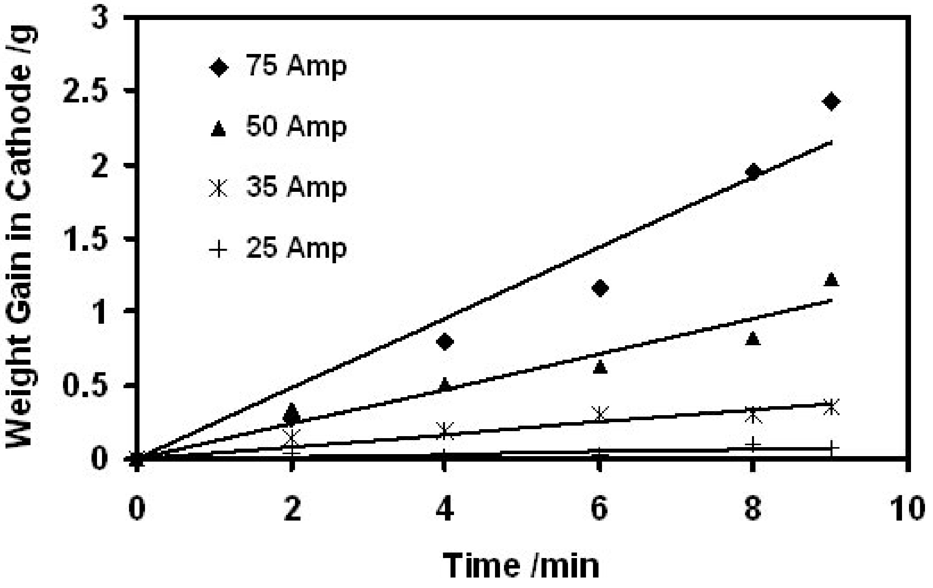

Fig. 4.12: The weight gain of cathode electrode with time for different values of current

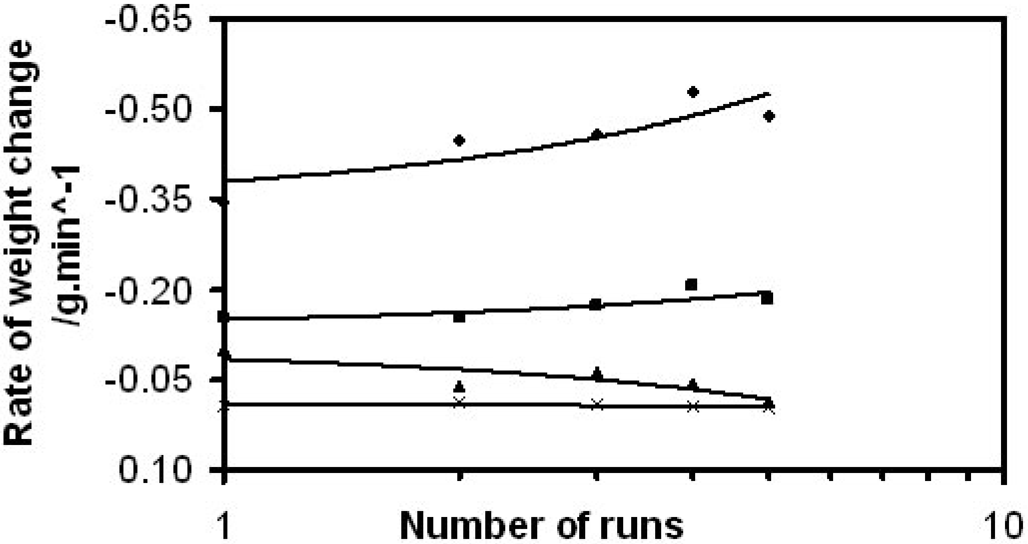

Fig. 4.13: Rate of loss of anode weight vs. number of runs for different values of current

It can be seen in the *Table 4.2* that the scatter of weight loss of the anode increases with time. Not only that, this deviation is higher for lower values of the current. For the weight gain of the cathode, this scatter is much more than the anode. This can be attributed to a loss of deposits from the cathode electrode during arc-discharge. The weight gain data of the cathode are presented in *Table 4.2*.

The weight loss of the anode was calculated for each run for a particular set of experimental parameters. Finally, an average loss of the anode weight was calculated. In *Fig. 4.13*, the average weight loss of the anode per minute vs. number of runs is plotted for the different four currents. It is found that the weight loss of the anode electrode in not constant with time. At higher values of the current, the weight loss of the anode increases with time during the arc-discharge, whereas for lower values of the current, the weight loss of the anode is almost constant or even decreases with time. It is well known that the plasma temperature increases with an increase in current. Therefore, for a higher water temperature, the weight loss of the anode increases with time.

The kinetic parameter is very important to calculate the rate of weight change, because the kinetic parameter is directly proportional to the weight change. Herein, it is assumed that the contribution of the cathode in the creation of nanotubes is negligible. *Fig. 4.14* is representing the plot for the current vs. the kinetic parameter, *k*, for the anode. If the second order polynomial regression of this plot with the regression coefficient 1 is taken, the following equation (*Eq. 4.3*) is derived, where, *I* is the current and *k* is kinetic parameter

$$k = -9e^{-5} I^2 + 1e^{-4} I + 0.0424 \qquad \textit{Eq 4.3}$$

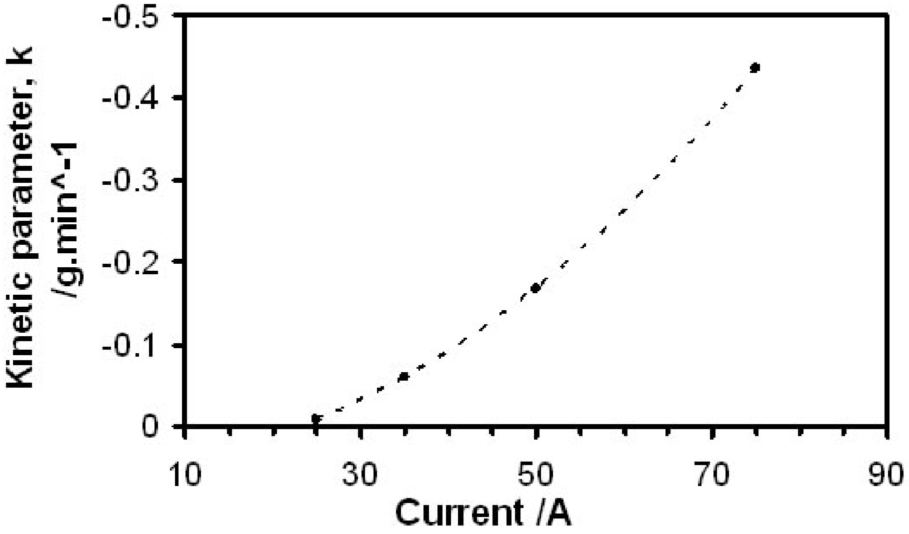

Fig. 4.14: The Plot of different values of current and its parametric constant for the synthesis of the CNTs

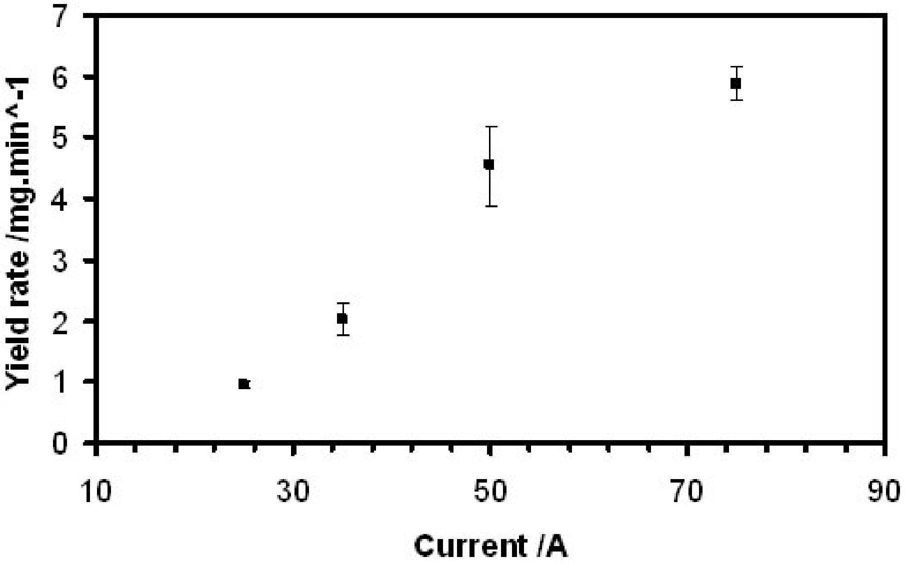

Fig. 4.15: The plot of different current and its corresponding rate of yield for the synthesis of the CNTs in water

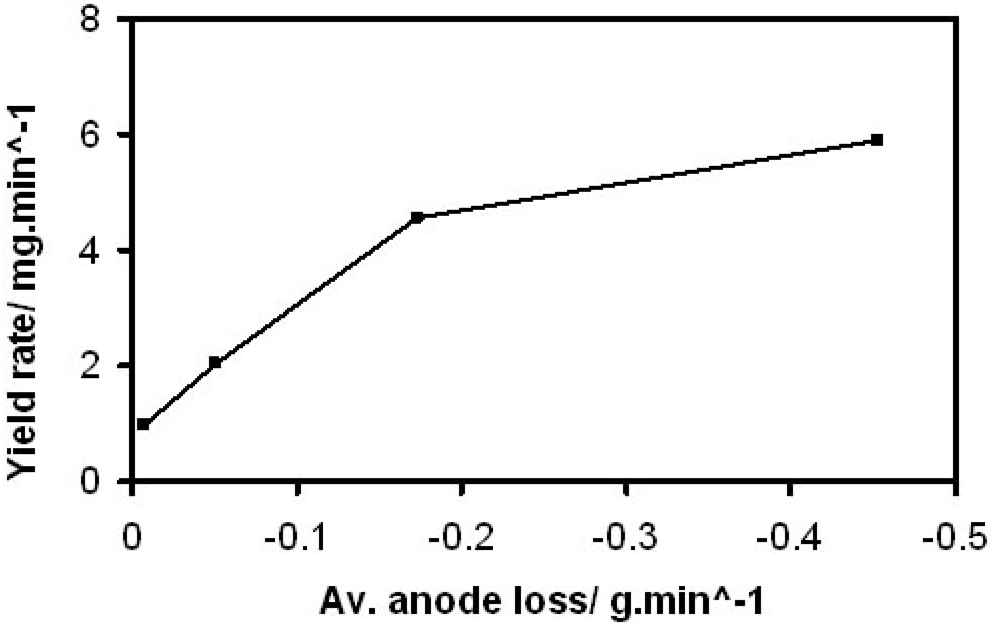

Fig. 4.16: The plot of average rate of anode loss vs. yield at different current values

We know that *k* for the anode is directly proportional to the consumption of the anode. The positive intercept, in *Eq. 4.3* is suggesting that a threshold value of the current is required for the consumption of the anode. In other words, a plasma will be created at a threshold current of approximately 20 *A*. Instead of a polynomial regression, a linear regression with coefficient 0.98 gives the approximately same threshold value.

Fig. 4.15 shows the current (*A*) and the plot of the rate of yield ($mg.min^{-1}$). The actual production rate with respect to the current is tabulated in *Table 4.2* If the curve is formatted, and considering second order polynomial regression with a regression coefficient of 0.985, the threshold current value for the formation of CNTs is approximately 20 *A* by extrapolating *Eq. 4.4*. However, by taking the linear a regression with regression coefficient of 0.9423, the threshold value of the current (*A*) for the formation of CNTs is approximately 12 *A* (*Eq. 4.5*). The equation for the kinetic parameter and the current shows the anode consumption starts at 20 *A*.

$$y = 0.0001I^2 + 0.0229I - 0.4185 \qquad \text{Eq. 4.4}$$

$$y = 0.0091I - 0.118 \qquad \text{Eq. 4.5}$$

where, y is amount of yield ($mg.min^{-1}$) and I is current (*A*)

Table 4.3: Table for the rate of production of CNTs with corresponding currents

Current (*A*)		75	50	35	25
Yield rate ($mg.min^{-1}$)	Value	5.89	4.54	2.03	0.96
	Standard deviation	0.28	0.65	0.26	0.06

Comparing the two plots (*Figs. 4.14* and *4.15*) it can be concluded that the arc starts at 20 *A* which initiates the creation of CNTs.

Fig. 4.16 is representing the average loss weight of the anode vs. yield. The yield is not directly proportional to the current. However, with an increase in the value of the current, both the weight loss of the anode and the yield increase. In other words, the efficiency of the production of the CNTs decreases with an increase in current. It has been speculated from the above experiments that the other carbonaceous products, especially amorphous carbon, increase with increase of current.

4.1.7. Mechanism of Formation of CNTs

The CNT specimens were extensively studied in TEM to unravel the mechanism of the formation of CNTs during the arc-discharge in solution. The formation of CNTs by rolling of graphitic carbon sheets from the anode material during the arc-discharge was suggested[31,36]. Recent attempts revealed that the formation of some of the nanotubes remained incomplete[99]. From *Fig 4.17*, it is obvious that the original graphene sheets were partially rolled up leaving behind some tub-shaped portions. The presence of such tub-shaped portions suggests that CNTs were formed by rolling of graphitic layers from the anode materials. In the present study, the HRTEM micrograph in *Fig. 4.3(f)* also shows a dislodged graphene sheet with a wavy surface morphology. Theoretical calculations[122] predict that the tubular structure is energetically more favorable than a flat graphene sheet.

The observation of curved or wavy non-graphitic carbon in the present investigation supports the scroll mechanism[36] for the formation of CNTs. *Ebbesen* and *Ajayan*[123] attempted to find such wavy graphene sheet as an evidence to establish this formation mechanism. However, they could not observe any such graphene sheets after arc-discharge in vacuum.

A careful examination of more CNT specimens, synthesized using arc-discharge in solution revealed the formation of MWCNTs. *Fig. 4.18(a)* shows a HRTEM micrograph of such a nanotube with nested cylindrical graphitic layers. A few layers are closed inside the nanotube by caps before final closure of the nanotube. The inner walls of CNTs in *Fig. 4.18(a)* have no access to carbon from outside for capping. It is likely that the inner walls closed before closing of the outer layer. Once a cap is formed on the tip of an inner cylindrical layer, the layer cannot grow further. *Iijima et al.*[117] showed such capped CNT which were formed by transformation of the cone to a cylindrical structure with the incorporation of a defect that induces a negative curvature at the tip of the CNT. To establish the mechanism of the CNT formation, extensive TEM investigations were carried out in the present study, however, open-ended CNTs could not be observed. The formation of a cap on the CNTs and the absence of the open-ended CNTs hint to a mechanism other than the scroll mechanism responsible for such formation of CNT. Interestingly, *Fig. 4.18(b)* shows different numbers of walls on the two sides of a nanotube with a final closure by a single cap. *Fig. 4.18(b)* also reveals the presence of incomplete and bent layers at the inner concentric wall, as marked with an arrow. Such defects could initiate an inner cap with time. The scroll mechanism can form a convoluted multi-walled CNT which eventually transforms to a concentric multi-walled CNT by the process of rearrangement of carbon atoms as suggested by *Yasuda et al.*[124]. *Fig. 4.18(c)* shows the same number of walls on the two sides of a CNT which may support the scroll mechanism. The formation of a cap on the CNT was possibly from the systematic deposition of atomic carbon produced during the arc-discharge process. The presence of a large number of CNTs on the surface of the cathode electrode, as presented in *Fig. 4.2(a)*, indicates the deposition of CNTs. Inside the plasma zone during the arc-discharge in solution, positively charged carbon ions migrate to the cathode surface under the applied bias and might help to sustain the growth of CNTs.

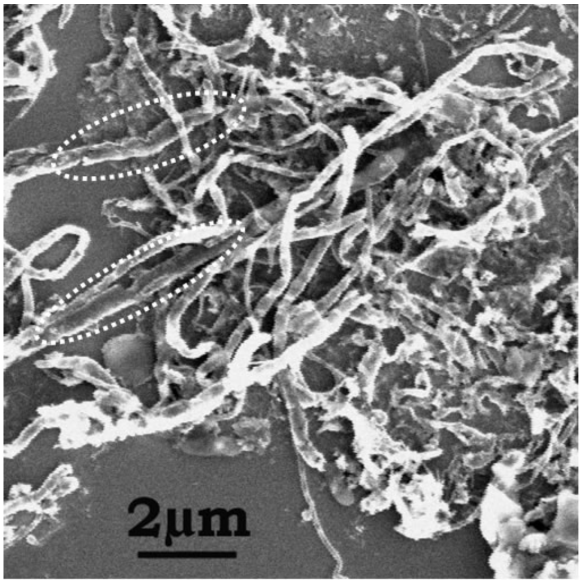

Fig. 4.17: SEM micrograph showing carbon nanotubes, partially rolled up graphene sheets marked with dotted ellipses and other carbonaceous materials

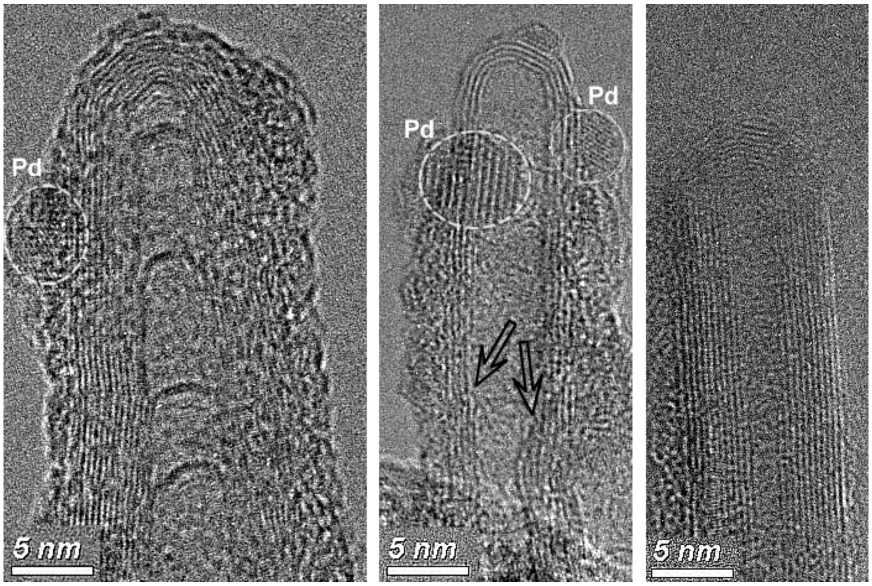

Fig. 4.18: (a) A TEM micrograph revealing the inner walls capped in a periodic manner, the number of walls is the same for both sides of the nanotube (b) unequal number of walls (c) CNT with the same numbers of walls on both sides

4.2. CNTs Decorated with Nanoparticles during ADS

The arc-discharge in water method has been successfully utilized to synthesize a number of metallic and oxide nanoparticles decorating CNTs with little modification in the process. *Fig. 4.19(a)* shows a SEM micrograph of clusters of ceria nanoparticles decorating CNTs. The size of the clusters is 15-20 μm. Such clusters of CNTs are found in the synthesis of pristine CNTs as well as for CNTs decorated with nanoparticles. *Fig. 4.19(b)* shows energy dispersive spectroscopy (EDS) data of CNTs decorated with ceria nanoparticles taken during STEM analysis. CNTs decorated with silica nanoparticles are successfully synthesized using a Si-precursor in the cell. The CNTs have been investigated with scanning transmission electron microscopy (STEM) using a high-angle annular dark-field detector for *Z*-contrast imaging. A STEM image and a corresponding EDS spectrum of the CNTs decorated with silica nanoparticles are shown in *Figs. 4.19(c)* and *4.19(d)*, respectively. Helically-coiled CNTs which are obtained by using a silicon precursor during ADS have been observed in TEM. The diameter of the tube is approximately 50 *nm* and the length is a few microns as shown in *Fig. 4.19(c)*. This helical structure is well known in carbon fiber growth patterns[42,125] in which two growth points can occur at a single nanotube cap. These two growth points provide a mechanism for twist growth which characterizes helical carbon nanotubes. In the present study, such multi-walled twisted helical CNTs, shown in *Fig. 4.19(c)*, are found to be very rare and the mechanism of growth is not clear for arc-discharge in solution. It is worth to mention that such kind of CNTs was found when CNTs were grown through catalytic pyrolysis of acetone on a silica substrate[125].

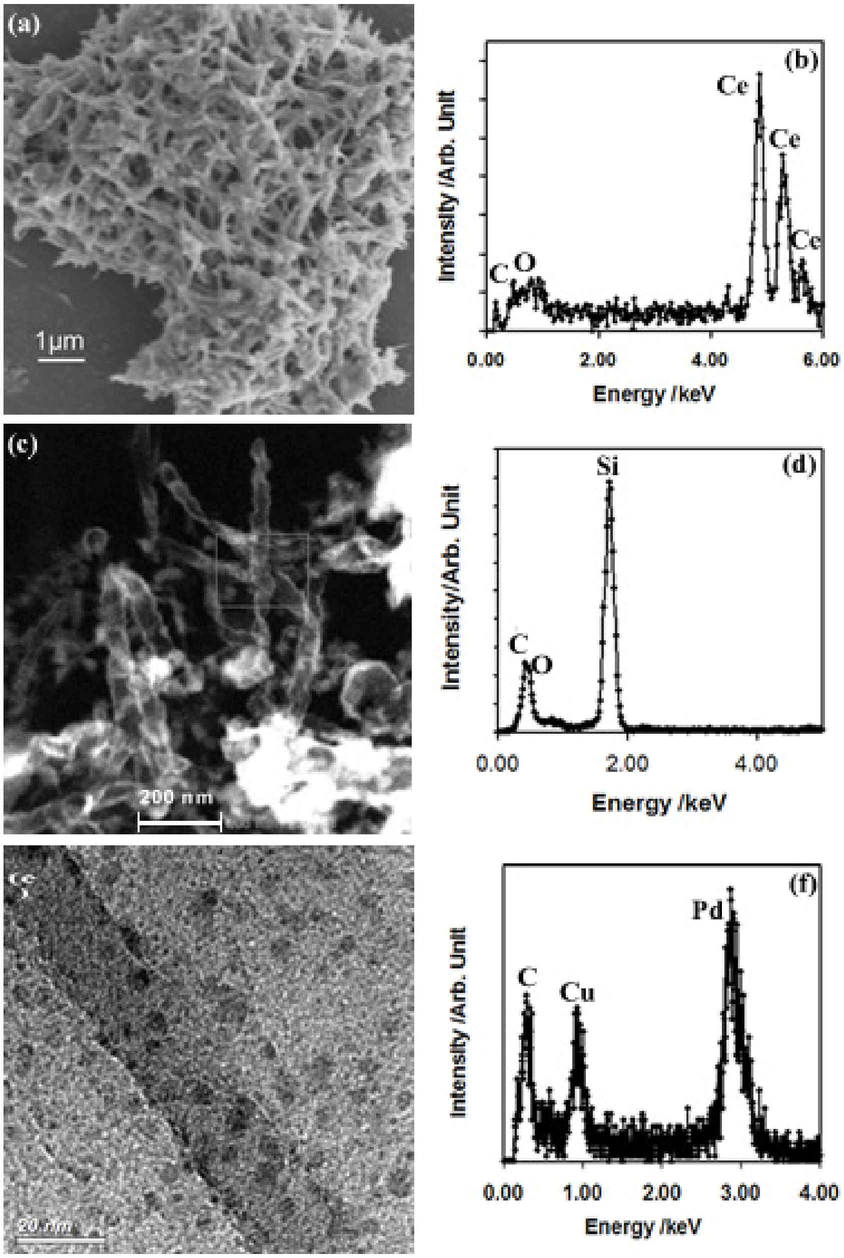

Fig. 4.19: (a) SEM micrograph of carbon nanotubes (CNTs) decorated with ceria nanoparticles, (b) EDS spectrum of CNTs decorated with ceria (c) STEM micrograph of CNTs decorated with silica nanoparticles and (d) corresponding EDS; (e) HRTEM micrograph of CNTs decorated palladium nanoparticles; Black spots are 3-4 nm diameter palladium nanoparticles. (f) EDS spectrum of CNTs decorated with Pd-nanoparticles; the presence of a Cu peak is due to the Cu-grid used during TEM investigation

An EDS spectrum was collected from the rectangular area shown inside the *Fig. 4.19(c)*. A TEM bright-field image of a CNT decorated with palladium nanoparticles is shown in *Fig.*

4.19(e). The diameter of the CNT is about 15 *nm*. The spherical dark regions in *Fig. 4.19(e)* correspond to the palladium nanoparticles with about 3 *nm* in diameter. *Fig. 4.19(f)* is an EDS spectrum of palladium nanoparticles decorating CNTs. The presence of a copper peak in EDS spectrum is due to use of a copper grid in the TEM study.

4.2.1. Study on Morphologies of Electrodes during ADS

Fig. 4.20(a) shows the surface of an electrode prior to the experiment. *Figs. 4.20(b)* and *4.20(c)* show the anode and the cathode electrode after arc discharge in water, respectively. The structure of the anode surface has significantly changed after the arc discharge. The morphology of the cathode surface is also uneven due to the deposition of the carbonaceous materials. *Figs. 4.20(e)* and *(f)* represent an overall picture of the electrodes before and after the experiment, respectively. The SEM investigation of the cathode materials also reveals a deposition of a huge amount of piled palladium nanoparticles decorated on CNTs as shown in *Fig. 4.21(a)*. A high-magnification SEM micrograph of such hillocks of decorated CNTs is presented in *Fig. 4.21(b)*. A detailed discussion on CNTs decorated with palladium nanoparticles is given in next section.

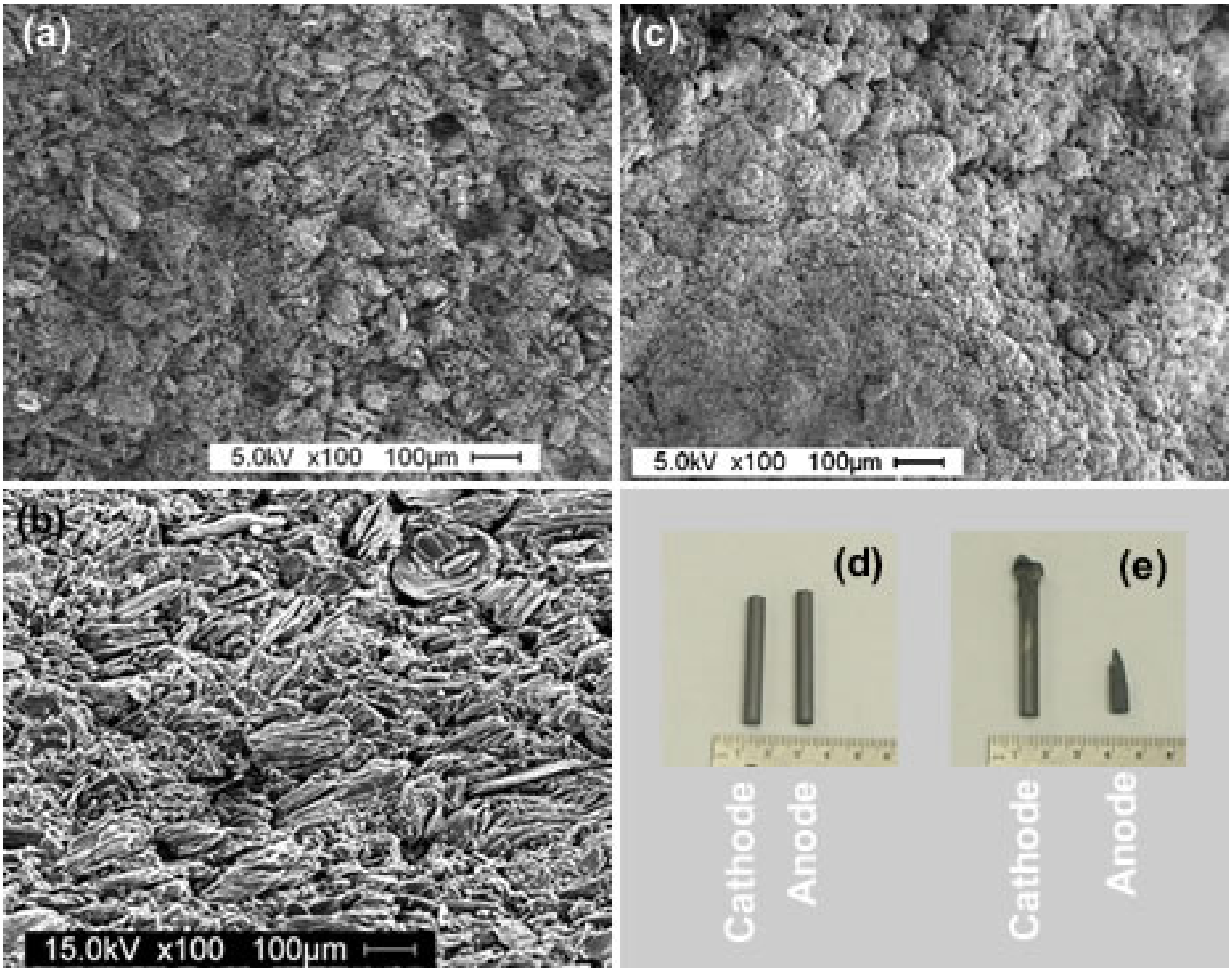

Fig. 4.20: (a) SEM micrograph of a graphite rod prior to the experiment. After 10 minutes of arc-discharge (b) SEM micrograph of the anode, (c) SEM micrograph of the cathode; Images of graphite rods (d) before , and (e) after the experiment

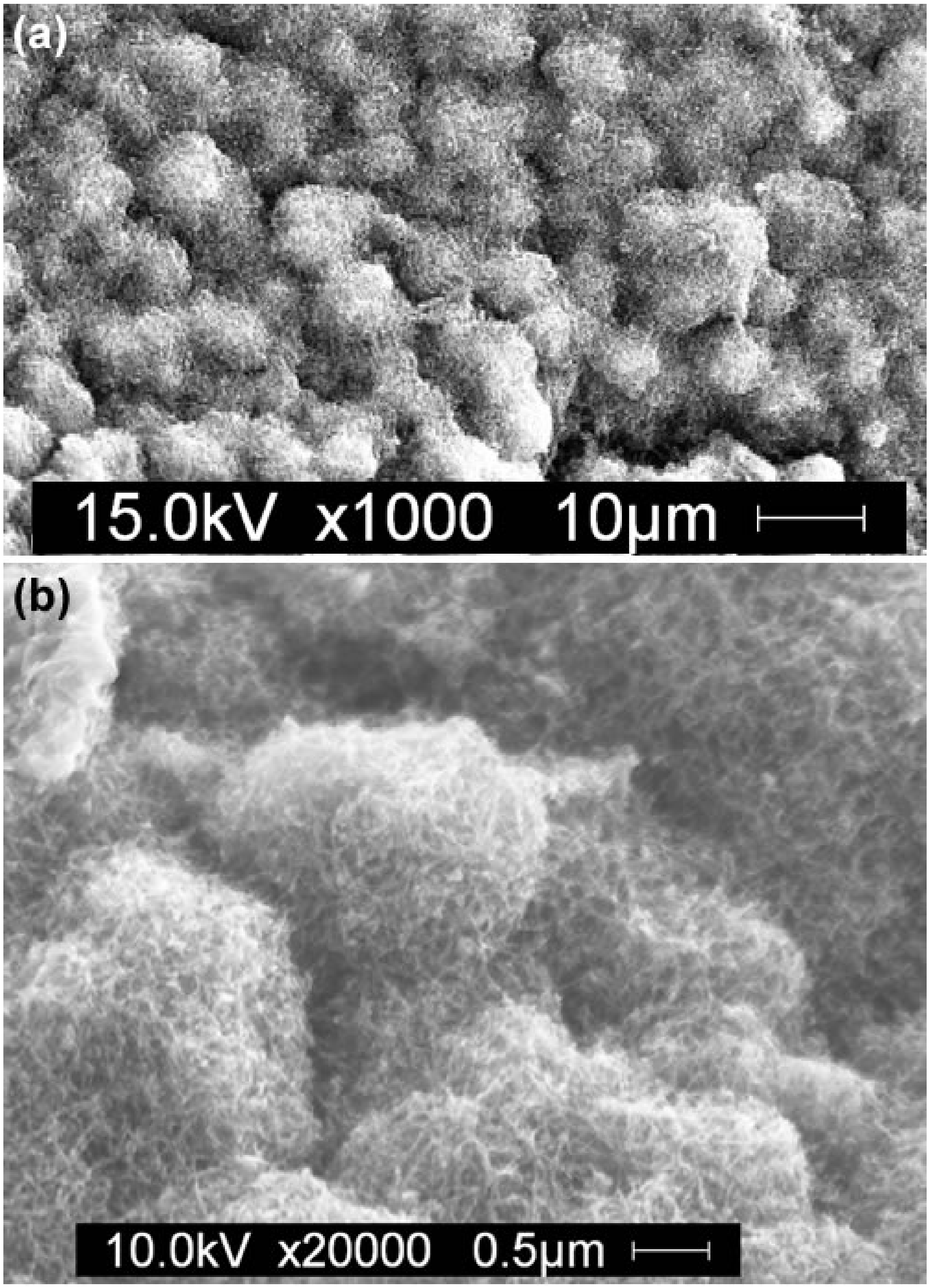

Fig. 4.21 (a) Low-magnification and (b) high-magnification SEM micrograph of CNTs taken from the tip of the cathode

4.2.2. Palladium Nanoparticles Decorated on CNTs

A STEM micrograph of palladium nanoparticles decorated on CNTs is presented in *Fig. 4.22(a)*. The STEM micrograph reveals the presence of a large number of nanotubes. A TEM bright-field micrograph of one such a CNT decorated with palladium nanoparticles is shown in *Fig. 4.22(b)*. The diameter of the CNT is about 15 *nm*. The spherical darker regions in *Fig. 4.22(b)* correspond to the palladium nanoparticles of about 3 *nm* in diameter. The EDS spectrum, shown in *Fig. 4.19(f)*, reveals the presence of carbon and palladium. The EDS spectrum does not show any chlorine peak which suggests that chlorine was not present either as palladium chloride inside the nanotubes or as atomic chlorine attached to the sidewall. Sidewall functionalization of CNTs with fluorine using *HF* vapor at temperatures higher than 600 °*C* has been reported[126], however to date there has been no study reported on the functionalization of chlorine atoms.

An XRD pattern collected from CNT decorated with palladium nanoparticles is presented in the *Fig. 4.23*. The sharp high-intensity peaks at $2\theta = 26.4^{\circ}$ and 54.6° are representing the CNT (002) and (004) plane, respectively. The same result was found when X-ray diffraction studies were carried out on pristine MWCNTs. The additional peak at $2\theta = 40.1^{\circ}$ confirmed the presence of palladium nanoparticles[127]. The inset plot on the *Fig. 4.23* is a blow-up image of a certain area of *Fig. 4.23* to show the low-intensity diffraction peaks of palladium. Three peaks of palladium are identified in the inset figure of *Fig. 4.23*. They are (111) at 41.1°, *Pd*(200) at 46.5° and *Pd*(220) 68.5°. It is observed that the peak values are in very close agreement with literature value[127]. The peak ($2\theta = 40.1^{\circ}$) shows the broadening of peak. Broadening of diffracted peaks indicates the presence of the palladium nanoparticles.

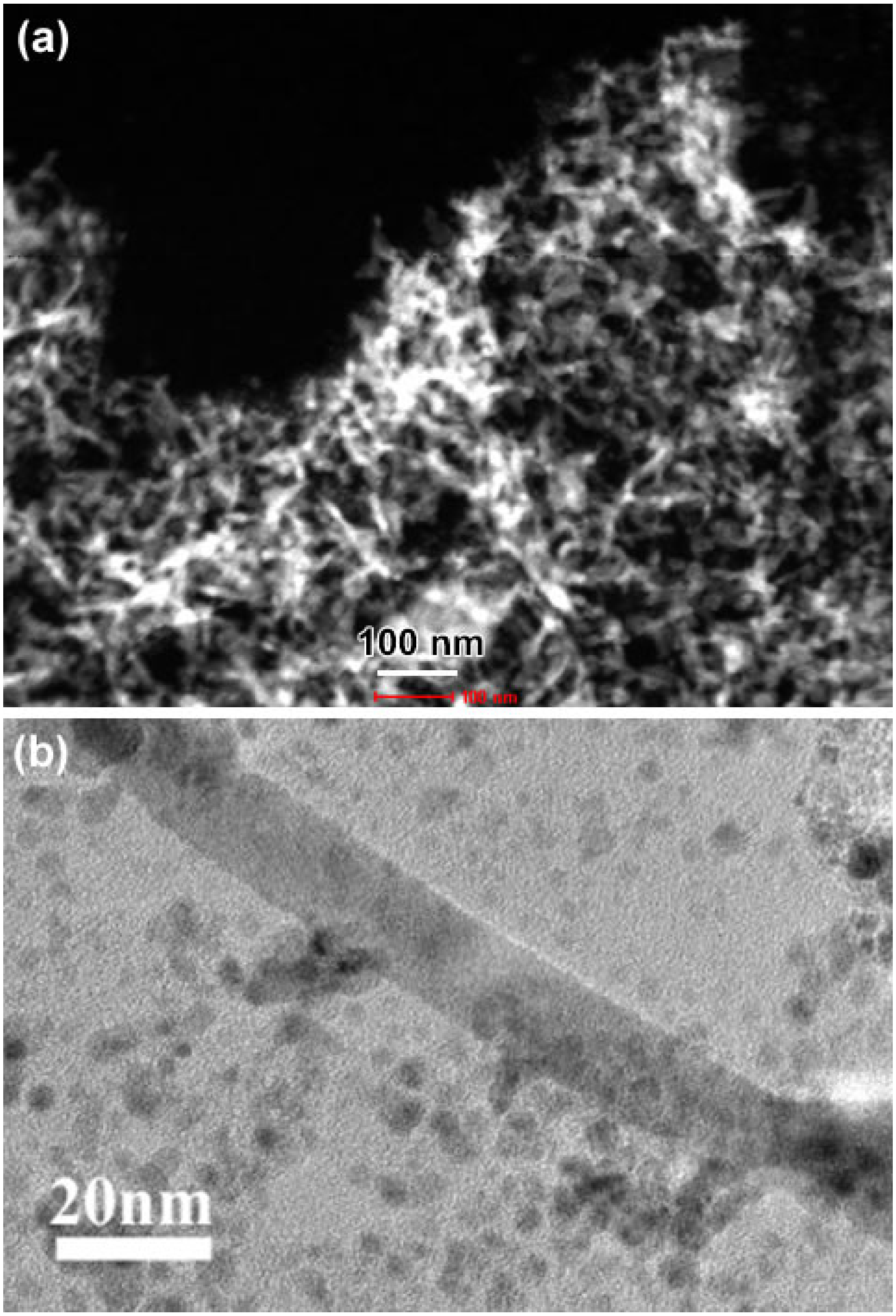

Fig. 4.22: (a) STEM micrograph of hillocks of CNTs, (b) TEM images of Pd nanoparticles decorated on CNT

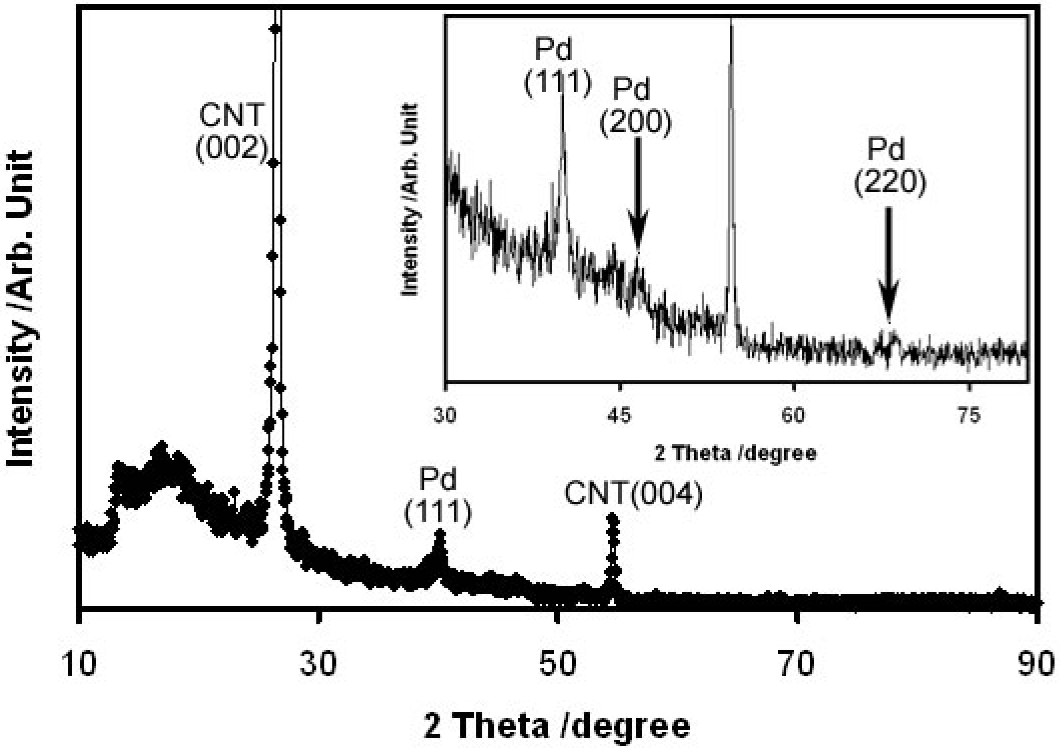

Fig. 4.23: X-ray diffraction profiles of CNTs decorated with palladium nanoparticles

A zero-loss energy filtered image of palladium nanoparticles decorated on CNT is shown in *Fig. 4.24(a)*. An agglomeration of palladium nanoparticles in the center of the projected CNT can be observed in *Fig. 4.24(a)*. To confirm further, a carbon map and a palladium map have been collected using the *Gatan* imaging filter (GIF) on the same portion of the nanotube. Such palladium and carbon maps of the CNT are shown in *Figs. 4.24(b)* and *(c)*, respectively. *Fig. 4.24(b)* shows that the bulged area of the CNT is caused by the deposition of several palladium nanoparticles. The palladium map also reveals that the CNT is decorated with palladium nanoparticles, however, the micrograph [*Fig. 4.24(b)*] does not clearly show that all nanoparticles are outside the CNT. HRTEM is used to investigate the actual position of the palladium nanoparticles. A CNT with nicely decorated and well-separated palladium nanoparticles is shown in *Fig. 4.25(a)*. The HRTEM micrograph shows the lattice fringes of both the CNT and the palladium nanoparticles. The same CNT has also been investigated with scanning transmission electron microscopy (STEM) using the high-angle annular dark field detector for *Z*-contrast imaging [see *Fig. 4.25(b)*]. Because of the high atomic weight, palladium nanoparticles in *Fig. 4.25(a)* appear as bright spots. The HRTEM micrograph in *Fig. 4.25(c)* shows the lattice fringes of the CNT.

In order to investigate the crystal structure of the palladium nanoparticles, selected-area diffraction patterns (SAED) were collected in the TEM mode. *Fig. 4.26* shows a SAED pattern with nine distinct *Debye-Scherrer* rings compatible with a face-centered cubic crystal structure of the palladium particles. The inset image is showing the intensity profile of the rings.

XPS is used to confirm the chemical state of the palladium nanoparticles. The de-convoluted XPS spectrum with the *Pd(3d)* envelope is shown in *Fig. 4.27* revealing the presence of $Pd(3d_{5/2})$ and $Pd(3d_{3/2})$ peaks at binding energy values of 335.6 and 340.9 *eV*, respectively. Such binding energies are similar to those reported for palladium in the literature[128]. The presence of a small amount of palladium oxide has also been confirmed in the XPS envelope as shown in *Fig. 4.27*. The presence of such a small amount of oxides is believed to be formed due to surface oxidations of nanoparticles during sample

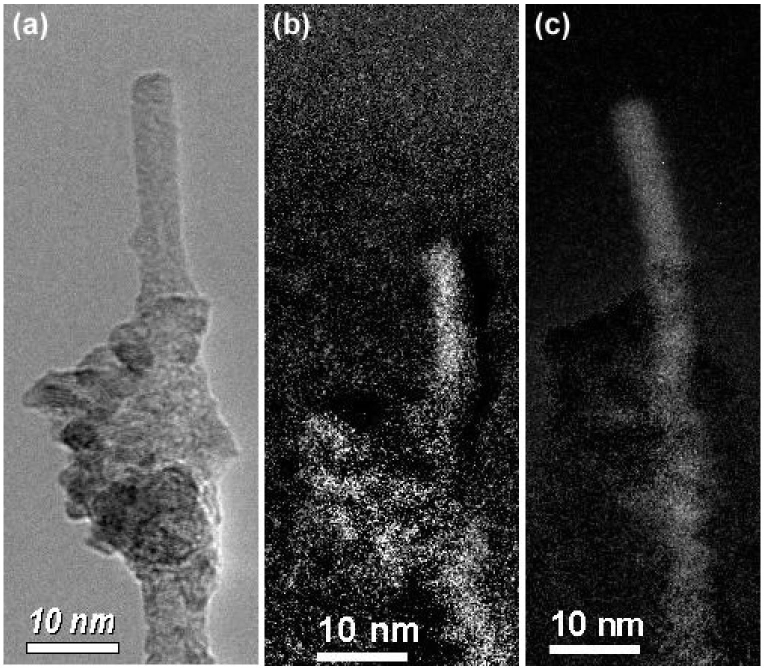

Fig. 4.24: (a) Zero-loss energy filtered TEM image; Energy-loss maps of (b) palladium, and (c) carbon

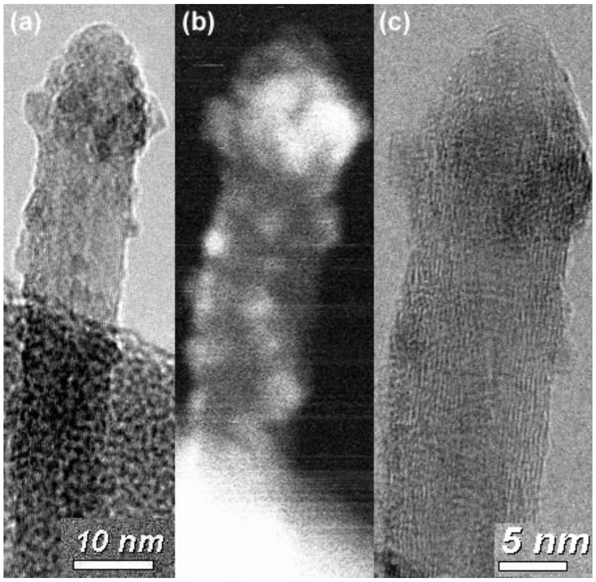

Fig. 4.25: (a) HRTEM image with black spots (b) STEM image of the same nanotube reveals the palladium nanoparticles (white spots) decorated around the nanotube (c) HRTEM image showing the lattice fringes of the CNT

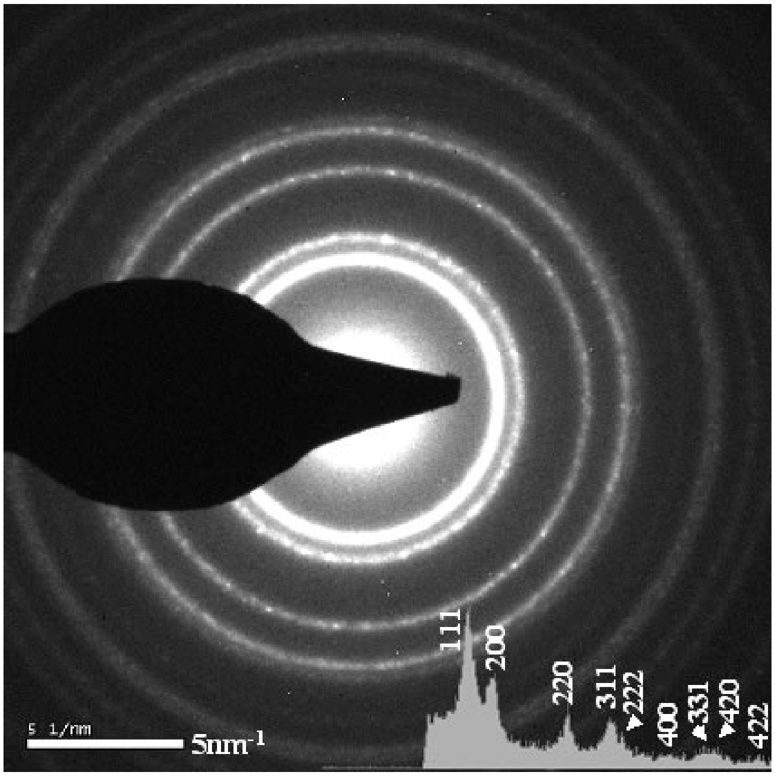

Fig. 4.26: Pd-nanoparticles inside the CNT; SAED pattern Pd nanoparticles, the intensity profiles of diffraction peaks along with miller indices (inset)

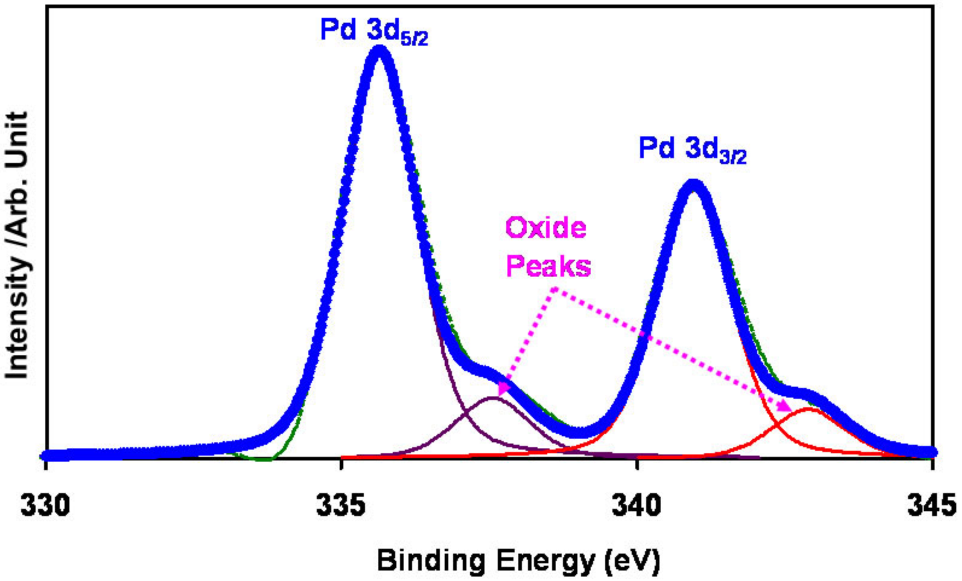

Fig. 4.27: XPS Pd(3d) envelope taken from the CNTs decorated with Pd nanoparticles

4.2.3. Chemistry of the Solution of the Pd-CNT Synthesis System

Fig. 4.28 represents the deconvoluted UV-VIS absorption curve of the aqueous solution of 2.087 *mM* $PdCl_2$ with 0.1*M* hydrochloric acid. The ratio of the chloride ions to the palladium ions, and the ionic strength in the aqueous solution of $PdCl_2$ with hydrochloric acid are calculated to be 50 and 0.10626 $mol.g^{-1}$, respectively. *Sundaram* and *Sandell*[129] revealed the existence of six chloro-complexes, $[PdCl]^{+}$, $[PdCl_2]$, $[PdCl_3]^{-}$, $[PdCl_4]^{2-}$, $[PdCl_5]^{3-}$ and $[PdCl_6]^{4-}$, at different ratios of the chloride ions to the palladium ions in different aqueous solutions. The higher-order complexes, $[PdCl_5]^{3-}$ and $[PdCl_6]^{4-}$ form when the ratio of the chloride ions to the palladium ion in the aqueous solutions[129] is more than 4. The UV-VIS envelope of the present system as presented in *Fig.4.28* shows the presence of peaks at 428 *nm*, 467 *nm* and 500 *nm*, confirming the presence of $[PdCl_4]^{2-}$ and higher chloro-complexes such as $[PdCl_5]^{3-}$ and $[PdCl_6]^{4-}$. The existence of such higher chloro-complexes in the electrolyte plays an important role during the reduction of palladium ions to metallic palladium. The role of these chloro-complexes will be discussed in the section on the mechanism of the deposition of palladium.

4.2.4. Mechanism of Formation of Pd-Nanoparticles in Pd-CNT System

Palladium nanoparticles have been synthesized from a mixture of 2.087 *mM* palladium chloride and of 0.1 *M* hydrochloric acid. In the hydrochloric acid medium, $PdCl_2$ transforms [117] into $[PdCl_4]^{2-}$, a palladium tetra-chloro-square planar complex, as shown in *Eq 4.5*.

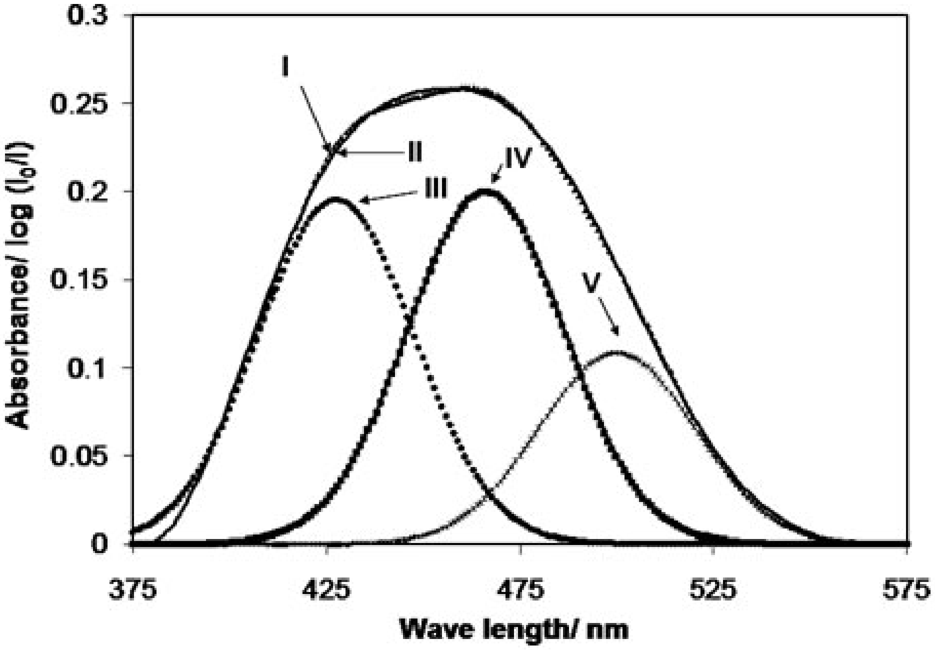

Fig. 4.28: Absorbance (log I_0/I) vs. wave length plot for the aqueous palladium chloride solution in 0.1M HCl. I and II in the figure indicate fitted and experimental lines respectively; III, IV and V are due to the formation of complexes of palladium chloride in HCl

The UV-Vis envelop of the palladium chloride solution presented in *Fig. 4.28*, is showing the formation of higher-order complexes with a palladium tetra-chloro-complex. The reduction of such complexes to metallic palladium (Pd^0) is the subsequent step during arc-discharge in solution. In *Eq 4.6,* the tetra-chloro-complex is taken as an example.

$$PdCl_2 + 2Cl^- = [PdCl_4]^{2-} \qquad Eq.\ 4.6$$

$$[PdCl_4]^{2-} \longrightarrow Pd^0 + 2Cl_2 \qquad Eq.\ 4.7$$

During the arc-discharge in solution, a simultaneous formation of CNT and the reduction of $[PdCl_4]^{2-}$ to Pd-nanoparticles as well as their in-situ decoration of CNTs is taking place through *Eq. 4.7.* Although the exact mechanism for the reduction of palladium chloride into nanoparticles of metallic *Pd* is not clear, the following possibilities may be considered:

1. Reduction of palladium ions into atomic palladium in the solution might take place with the help of reducing gases such as carbon monoxide and hydrogen. Such reducing gases are expected to form near the electrodes during the arc-discharge process through *Eq. 4.8*.

$$C + H_2O = CO + H_2 \qquad Eq.\ 4.8$$

The formation of such reducing gases due to the reaction of carbon with water vapor during arc discharge in solution was reported by others[60].

2. The temperature at the site of the arc is expected[30] to be greater than 3500 º*C*. Hence, the plasma region produced by the arc adjacent to the electrodes is enveloped by a solution-vapor interface. The decomposition temperature of the palladium chloride[130,131] is 738 *ºC* at ambient atmospheric pressure. The thermal decomposition process possibly leads to the formation of atomic palladium and chlorine gas near the electrodes, which is the probable reason for the absence of a chlorine peak in the EDS spectrum [*Fig. 4.19(f)*]. Thermally dissociated palladium nanoparticles may subsequently decorate the CNTs.

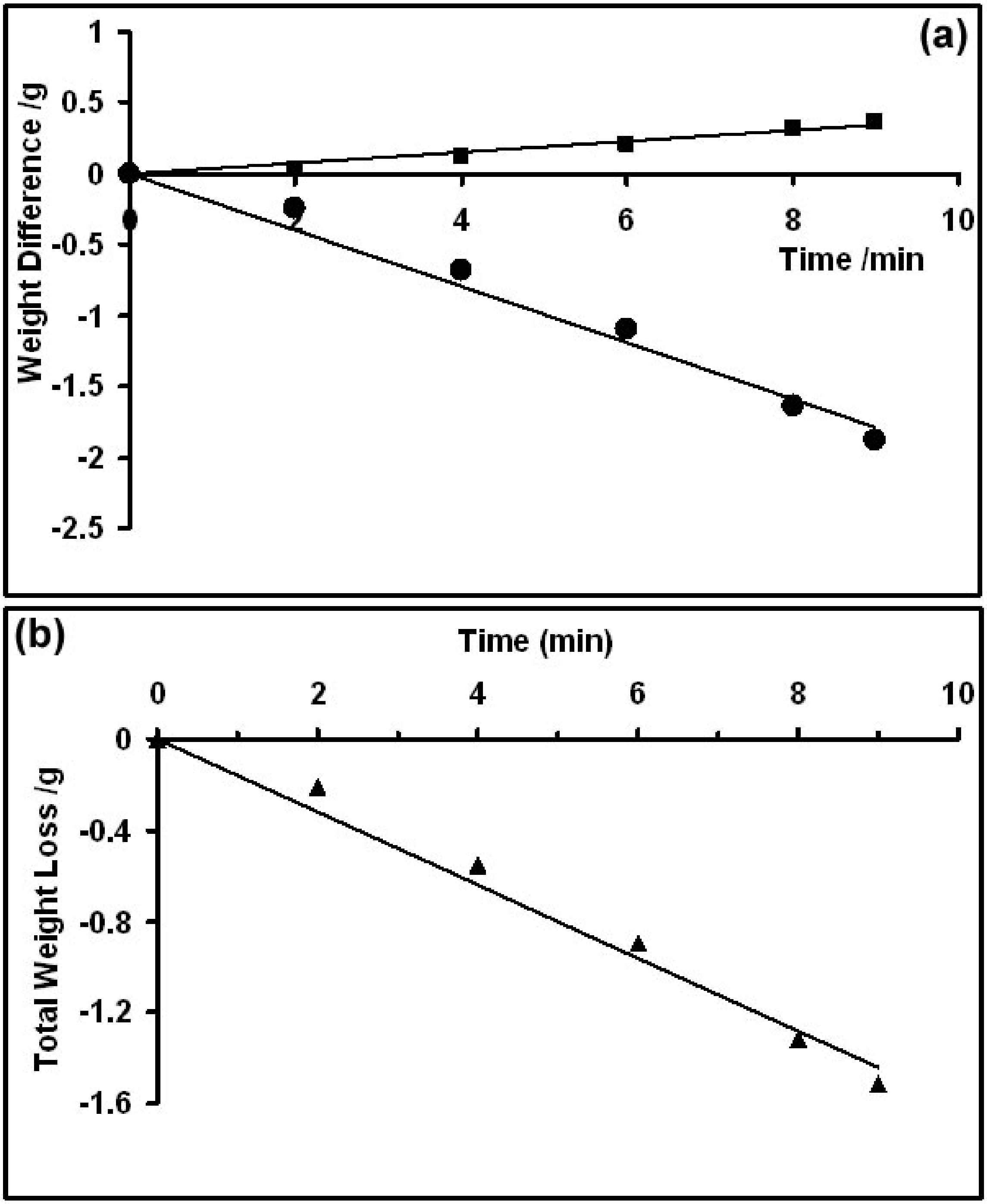

Fig. 4.29: (a) Weight change of cathode and anode electrodes with time during arc-discharge in solution (b) Overall weight change of anode and cathode with time during arc discharge in solution

3. The plasma region near the electrodes during the arc discharge is an excellent source of electrons[132]. The palladium ions situated near the solution-vapor interface can be reduced to palladium atoms accepting electrons from such electron pool.
4. The formation of atomic *Pd* through an electrochemical process under the applied bias[19,20,21,22] is another possibility.

Although four mechanisms were proposed for the formation of palladium nanoparticles, high-temperature dissociation of palladium chloride is highly likely, because the decomposition temperature of palladium chloride is 738 º*C* at ambient atmospheric pressure whereas the temperature at the anode edge is more that 3000 º*C*.

4.2.5. Parametric Study on the Pd-CNT System

Figs. 4.29(a) and *(b)* represent the weight change of each electrode individual as well as the cumulative weight change in every two minutes, respectively. The weight-change relationship in the present system can be mathematically expressed with *Eq. 4.9,* where t is the time in minutes and ΔW is the weight change in $g.cm^{-2}$ during arc-discharge in solution, and k_c is the normalized kinetic parameter in $g.cm^{-2}.min^{-1}$.

$$\Delta W = k_c \times t \qquad \textit{Eq. 4.9}$$

The experimental values of k_c in *Eq. 4.9* for cathode and anode are 0.52 $g.cm^{-2}.min^{-1}$ and -2.73 $g.cm^{-2}.min^{-1}$, respectively. The k-value of anode and cathode electrodes conbined is -2.17 $g.cm^{-2}.min^{-1}$. The cathode gains weight with time whereas the anode loses weight with time during the arc discharge. The overall weight of the electrodes decreases with time. A portion of the excessive heat produced in the solution during arcing help evaporating the solution. The evaporation rate of the water during arc-discharge in solution in the present system was found to be 3.2 $cm^3.min^{-1}$. The plot for the loss of volume of the solution with time is presented in *Fig. 4.30*.

4.2.6. Surface Area Measurement

Fig. 4.31 represents a linear plot of the extent of adsorbed nitrogen as a function of P/P_0 with a correlation coefficient 0.99. From the plot, the slope and intercept of the straight line are calculated to be 0.1475 $cc.g^{-1}$ and 0.0071 $cc.g^{-1}$, respectively. The BET monolayer volume (V_m) and BET constant (C) were found to be 6.468 and 21.78. Using *Eq. 3.6*, the surface area of the samples were determined to be 28.187±1.5 $m^2.g^{-1}$. It is interesting to note that the surface area of pristine CNTs is found to be 83.95±3.5 $m^2.g^{-1}$. Astonishing, the surface area of palladium nanoparticles decorated is much lower than the pristine CNTs. This anomaly can be explained considering the density of palladium which is 12.8 $g.cm^{-3}$, and the surface area is directly related to the density of a material.

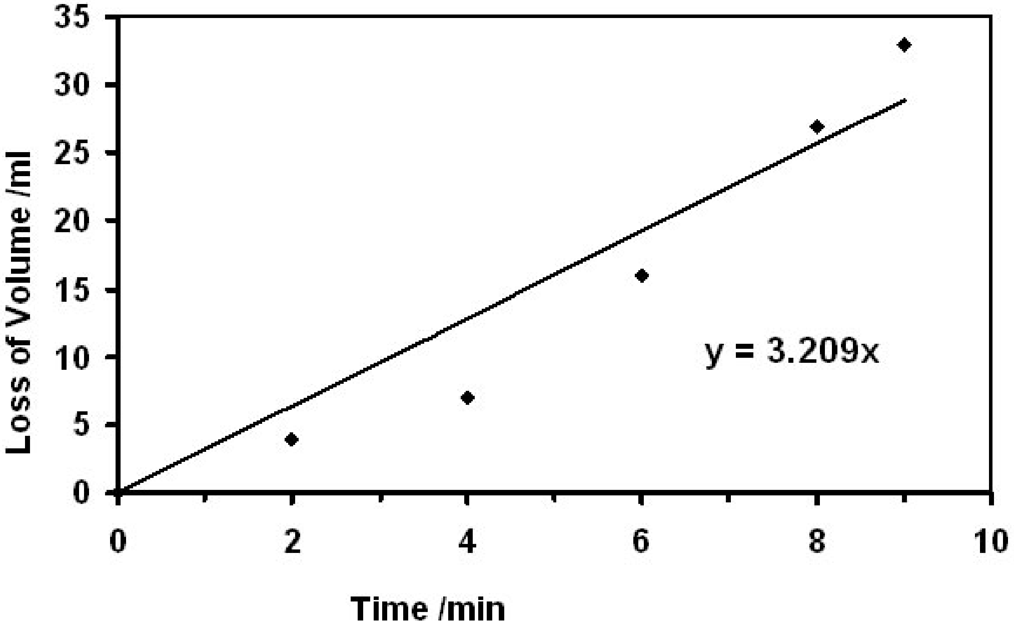

Fig. 4.30: Volume of solution loss vs. time plot during the ADS

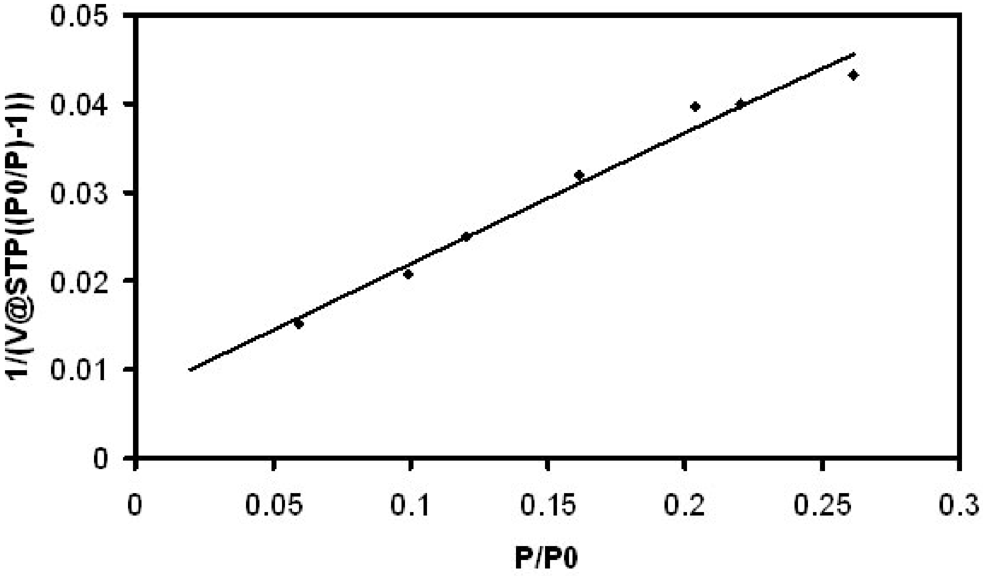

Fig. 4.31: Volume of nitrogen adsorption with various values of P/P0 found from BET sorptometer for surface area analysis

4.2.7. Hydrogen Adsorption and Desorption

A property of central importance in the application of palladium nanoparticles for hydrogen storage is the relation between the pressure and the temperature. Palladium forms palladium hydrides when it absorbs hydrogen. Palladium hydride may be considered as an interstitial alloy, PdH_x, $0 \leq x \leq 1$, where octahedral sites of the *fcc* palladium lattice are occupied by hydrogen. In chemisorption, however, such formation of a palladium-hydrogen alloy is only expected to happen at the surface. Chemisorption is the adsorption of gas in which the forces involved are valence forces as those operating in the formation of chemical compounds. *Sellers*[133] computed the perpendicular stretching potentials, the equilibrium *Pd-H* distances, and, the quadratic stretching force constants during chemisorption. The hydrogen bond to the *Pd (111)* plane penetrates the surface and a significantly interacts with palladium atoms in the second layer. Since chemisorption occurs only on the surface, the extent of hydrogen which can be absorbed by the palladium nanoparticles will not be possible to determine. However, an indication of surface adsorption would promote further research on hydrogen storage in palladium nanoparticles decorated CNTs.

Fig. 4.32 shows the hydrogen chemisorption behavior on palladium nanoparticles decorated on CNTs at three different temperatures. The amounts of hydrogen adsorptions in palladium nanoparticles decorated on CNTs at 25 º*C* and 30 º*C* are the same whereas adsorption and desorption follow different paths. This suggests that hydrogen atom mobility and chemisorption are going on at different ways whereas at 40 º*C* the amount of hydrogen adsorption drops down drastically if temperature rises slightly. This preliminary result, however, shows the ability to store hydrogen in palladium nanoparticles decorated on CNTs.

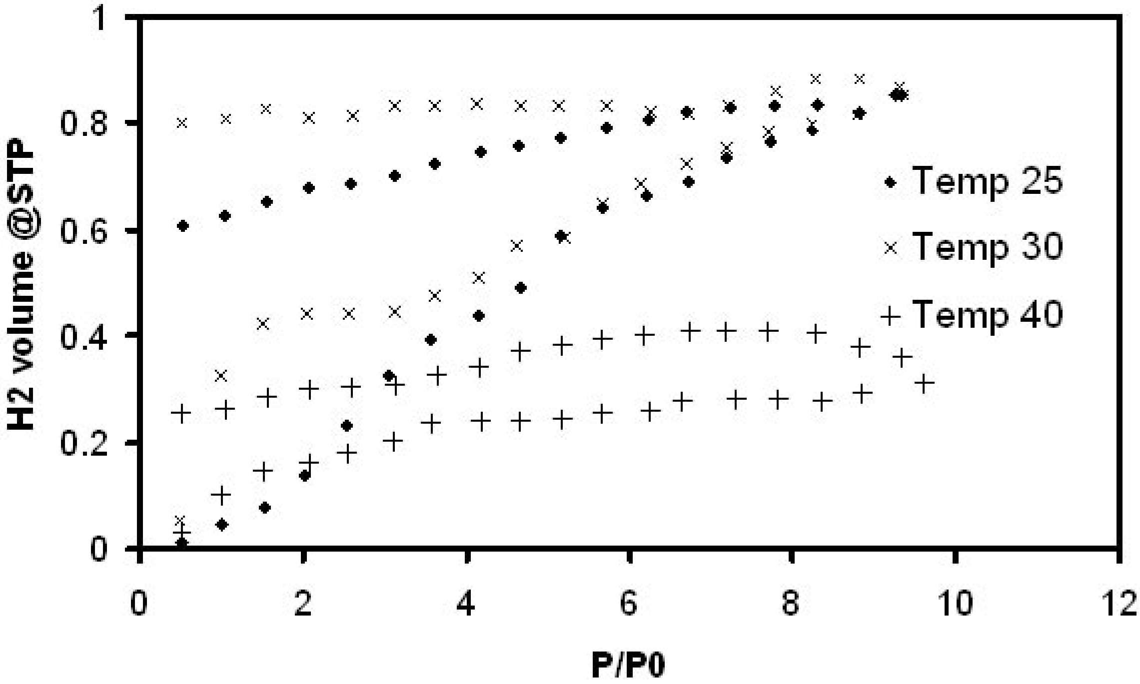

Fig. 4.32: The chemisorptions of hydrogen on palladium nanoparticles decorated CNTs at various temperature

CHAPTER 5: CONCLUSION

5.1. Synthesis Method for CNT Production

- A simple, low-cost, high efficiency method for carbon nanotube synthesis is reported.

- Such inexpensive route of CNT synthesis doesn't rely on the catalyst for the production of CNT synthesis. The major advantage lies in the production of very clean CNTs without major purifications.

- The method is based on conventional arc-discharge in argon at low pressure. In our process, two graphite electrodes, acting as a cathode and an anode, were brought in contact to create an arc inside water at atmospheric pressure using a direct current power supply, which has the capability to supply a constant potential of 28 *V* and currents of 25 *A*, 35 A, 50 A and 75 A. We call this process arc-discharge in solution (ADS).

- A range of industrially important carbon nanostructures apart from CNTs was synthesized using ADS. This process is highly scalable. So, low-cost large-scale production of high-quality CNTs is easily achievable which can bring down the overall production cost of CNTs.

- The synthesis of CNTs decorated with nanoparticles, such as palladium, nickel, silica, ceria etc., was carried out successfully using appropriate precursor solutions.

- A comprehensive parametric study on the arc-discharge in solution was successfully carried out to correlate the parametric data from the synthesis method, so that MWCNTs can be synthesized in a controllable manner.

- It was found that a steady rate of synthesis can be achieved at higher values of applied current. However, the efficiency of the production of CNTs decreases with an increase in current. Such discrepancy was found due to the formation of amorphous carbon.

- The rate of production of CNTs was as high as $5.89 \pm 0.28\ g.min^{-1}$ at 75 *A*.

5.2. Instrumentation for the ADS Process

- For the ADS process, a full-fledged instrumentation was developed and implemented successfully for both bulk and continuous production of CNTs and nanoparticles decorated CNTs.

- Such a custom-built instrument was controlled optoelectronically for the automation of the process.

- The optoelectronic system consists of three main components: a photosensor for optical emission diagnosis, a feedback loop which is composed of analogue electronics, a computing unit, and a Z-axis translational unit (servo).

- A kit of BASIC Stamp was used for the analog controller unit. To communicate between the analog unit and the computing unit, a program was written using BASIC language.

- The program was optimized to account for the inconsistency of the servo and the intrinsic instabilities created by the arc. The loop constantly checks the feedback reading from the photosensor. When the arc is diminished, the value of the photosensor signal increases, and the feedback loop activates the servo to drive the Z-translational lever towards the cathode, thereby maintaining the electrode gap constant.

5.3. Carbon Nanotubes Synthesized through ADS

- During arc-discharge in water, clusters of CNTs were found to float on the water surface. The diameter of average sized clusters was more than 10 μm.

- A high density of CNTs was also observed at the tip of the cathode in SEM studies. The microscopic investigation showed the formation of a ‘cotton-like’ stacking of nanotubes bundles.

- Extensive TEM studies on as-synthesized samples show that almost 50 % of the CNTs are not well-graphitized. High resolution transmission electron microscopy (HRTEM) shows that 50 % of CNTs are hemispherically capped among all capped CNTs.

- The average inner diameter of the CNTs synthesized by the arc-discharge in water process was typically 3 nm. The outer diameter of the CNTs was found to be in the range of 5-15 nm. The distance between the two concentric walls was 0.359 nm.

- All XRD peaks are slightly shifted to lower angles compared with scattering angles of graphite indicating a wider interlayer spacing due to turbostratic structure (two dimensional lattice) of CNTs. No additional peak for other graphitic carbonaceous material was found in this study.

- Using a BET spectrometer, the surface areas of samples were calculated and found to be 84±3.5 m2.g-1. This result was found to be higher than literature values.

- To remove the amorphous carbon from CNT samples, two types of oxidation were carried out: air oxidation by heating at 500 ºC for 30 min and chemical oxidation by 30 % H_2O_2 for 24 hrs.

- Similar amounts of weight loss were found from both oxidation results. The presence of the amorphous carbon is almost negligible after oxidations.

- The oxidation by H_2O_2 results in the formation of defect-enriched CNTs. Most of the nanotubes had suffered from corrosion forming pitting, necking and deposition of carbon at various places throughout the length on the nanotubes.

5.4. Other Carbonaceous Nanostructured Materials

- Along with CNTs, a wide range other carbonaceous materials, such as carbon nanohorns, carbon rods, amorphous carbon, carbon onions, nanoporous carbon (NPC), and a few dislodged graphene sheets were found during microscopic investigation.

- The average cone angle of carbon nanohorns synthesized by ADS process is about 18º. Nanohorns are the second most common tip found during TEM investigations.

- Carbon nanorod is very rarely found during TEM investigations.

- Carbon onions, NPC and dislodged graphene sheets are also found during the TEM investigation.

- The CNTs are often found to be accompanied with carbon nanoparticles or nanoshells. These are found to be hollow with spherical or oval shapes with a presence of pairs of pentagons and hexagons. A detailed study on various defect structures of different carbon nanostructures was also presented.

5.5. Nanoparticles Decorated Carbon Nanotubes

- In-situ decoration of CNTs with a variety of nanoparticles, including metallic particles as well as oxides, during synthesis of CNTs was successfully achieved using the arc-discharge in solution method.

- No additional step for the decoration of CNTs is required which makes it very efficient. A technique which simultaneously decorates the nanotubes with nanoparticles during its synthesis is inherently devoid of such disadvantages.

- The present study also focuses on the mechanistic aspects of the formation and the decoration of nanoparticles in the nanotubes.

- Although the actual mechanism of formation was not known, based on the experimental speculations, it can be inferred that scrolling of graphene sheet is a step for the formation of CNTs.

- The formation of 3 nm palladium nanoparticles was explained by a reduction of the palladium-chloro-complex. Such higher-order chloro-complex is found in acidic palladium chloride solutions.

- An UV-Vis spectrometer was employed to investigate the solution chemistry of such a palladium chloride solution. Four mechanisms were proposed for the formation of palladium nanoparticles

- The high-temperature dissociation of palladium chlorides is highly likely, because the decomposition temperature of the palladium chloride is 738 °*C* at ambient atmospheric pressure whereas the temperature at the anode edge is more that 3000 °*C*.

5.6. Palladium Nanoparticles Decorated on Carbon Nanotubes

- The surface area of palladium nanoparticles decorated on CNTs was measured using a BET spectrometer and found to be 28.187±1.5 $m^2.g^{-1}$.

- The reduction of the surface area from pristine CNTs can be explained considering the density of palladium. The density of palladium is 12.8 $g.cm^{-3}$, however that of MWCNT is less than 2 $g.cm^{-3}$.

- The adsorption and desorption behavior of hydrogen in palladium nanoparticles decorated on CNTs was measured using chemisorption of CNTs for a feasibility study on the hydrogen storage using palladium nanoparticles decorated on CNTs.

- The temperature-dependence of the adsorption–desorption studies was also studied. A significant amount of hydrogen adsorption on palladium nanoparticles decorated on CNTs was observed.

CHAPTER 6: FUTURE STUDIES

The future studies should include computer modeling of such nanomaterials system. The modeling will be done with density functional theory-molecular dynamics simulations (DFT-MD). The first principles approach is necessary to fully and accurately describe the relevant chemical interactions. MD simulations integrate Newton's second law of motion to predict the responses of atoms to external forces. While these first principles simulations are quite computationally intensive and will require continuous use of several nodes on an expanded Linux cluster.

The computational components of the proposed future work will consist of two related parts. The first part is the use of first principles DFT calculations to establish the mechanism of formation of CNTs, correlation between experimental parametric results and theoretical results and the control parameters for the formation of other nanostructures. The second part will include the examination of the interaction of nanotubes and related structures with metal and metal oxide nanoparticles. The DFT calculations will use ultrasoft pseudopotentials and will be performed within the supercell approximation using the local spin density approximation or the generalized gradient approximation with spin corrections. The objective will be to characterize the nature of these interactions, including atomic and electronic structures.

APPENDIX: PROGRAM FOR INTEGRATED CIRCUIT OF BASIC STAMP

In this appendix, a basic program for the automation of the arc-discharge synthesis process is reported. The Program was written in a derivative of the original BASIC language. The program consists of four major parts. All parts and the source code are given below.

I. Introduction

```
'Description:  Automation of apparatus for arc-discharge in solution process
'Contains:     Variable description, Initialization loop, and Automation loop
'{$STAMP BS2}                  'Current board revision (BS2)
'{$PBASIC 2.5}                 'Version of PBASIC (2.5)
```

II. Variable Definition

```
counter   VAR     Word
light     VAR     Word


DEBUG ? IN0                    'Bottom push button input
DEBUG ? IN2                    'Top push button input
```

III. Initialization

Initiation sets the servo at the appropriate X, Y and Z position. It turns on the green or red LED depending on running or stop. It also tells the debug window that initialization is completed.

```
IF (IN0 = 1) THEN              'RESET system
FOR counter = 800 TO 650 STEP 20
```

```
PULSOUT 15, 800

     PAUSE 7                    'Creates a 20 millisecond PAUSE between steps

     HIGH 13                    'Green LED turned on

     LOW 11                     'Red LED turned off

NEXT

DEBUG "Initialization Complete",CR,

"Ready to begin",CR,CR

ENDIF
```

IV. Feedback Loop

The feedback loop controls the servo, and therefore the Z- translational lever, through a range of motion. The Z- translational lever traverse a period of time until the arc is generated. The feedback loop is entered when the START button is pressed. The START button is attached to IN3 on the circuit board. A FOR loop is created to move the servo through the slowest possible traversal of the desired range of the servo. Generally 800 through 700, was chosen which allows it for the least possible horizontal movement and the maximum vertical movement. Both LEDs, red and green, are turned on to show that the feedback loop is in process. The feedback loop begins with checking if the arc has been started, thereby creating a resistance in the photosensor.

```
IF (IN3 = 1) THEN                'START when BUTTON pressed

FOR counter = 800 TO 700 STEP 1  'The range with the least horizontal

                                 'movement and most vertical
```

```
PULSOUT 15, counter
HIGH 11                              'Red LED on as well as green LED
DEBUG "Counter =", DEC counter,CR 'Output counter to see that it 'is counting properly

HIGH 7                               'Discharge capacitor
PAUSE 100
RCTIME 7, 1, light                   'Record amount of light
```

The following code snippet is designed to stop the system in the event that the RESET button is pushed. At any time there is power in the circuit, the circuit and program can be reset.

```
IF (IN0 = 1) THEN                    'RESET system
     DEBUG "Process Stopped",CR
     LOW 11
     GOTO Initialize                 'Re-initialize
```

The servo continues downwards until the photosensor is activated with the light from the arc. The activation of the photosensor increases the resistance to the value towards 1. Generally, a value of 5 or less is chosen to allow for error caused by the reading of photosensor. A RESET loop was incorporated to allow for a system reset. The value of resistance of the photosensor is checked to determine the activation of the loop. If the arc is constantly checked, it is assumed to be running. When the arc switches off, the value of the photo-resistor goes up to 10. The servo is positioned 10 pulses higher and the feedback loop is continued. This repositioning allows for a fresh start of the arc discharge process, and avoids the situation where the two carbon rods touch and current merely passes through them.

```
        ELSEIF (light < 5) THEN          'Check photo-resistor
            DO
            IF (IN0 = 1) THEN            'RESET system
                DEBUG "Process Stopped",CR
                LOW 11
                GOTO Initialize          'Re-initialize

            ENDIF

            HIGH 7                       'Discharge capacitor
            PAUSE 100
            RCTIME 7, 1, light           'Record amount of light
            DEBUG "still burning", CR    'A check to find out when program
                                         'is waiting a when it is counting
        LOOP UNTIL (light > 10)          'Until reaction is over
        PAUSE 750                        'Keeps process slow enough for
        counter = counter + 10           'an observer to follow
        PULSOUT 15, counter               'Move servo up 10 pulses to get a fresh start down
```

Finally, after the loop has run its course, the loop is exited. The green LED is turned off to show that the program has completed and needs to be reset. The red LED remains on to signal a stopped system. The system can then be reset and restarted with use of the buttons on the circuit board.

```
ELSE                        'fresh start down
        PAUSE 250           'Keep motion slow


ENDIF


PAUSE 250
NEXT
LOW 13                      'Green LED off to show completion of loop
ENDIF                       'Red LED still lit, red meaning stopped
LOOP
```

Once the program is successfully transferred to the integrated circuit, it can act independently without the need of a serial connection.

LIST OF REFERENCES

1. Vayssieres, L., “On the design of advanced metal oxide nanomaterials” *Int. J. Nanotech.* **1**, 1-41 (2004).
2. Huczko, A., “Template-based synthesis of nanomaterials” *Applied Physics A* **70**, 365-376 (2000).
3. Suryanarayana, C., “The structure and properties of nanocrystalline materials: issues and concerns” *JOM* **54**, 24-27 (2002).
4. Dresselhaus, M.S.; Avouris, P., In “Carbon Nanotubes: Synthesis, Structure, Properties and Application” Ed: M.S. Dresselhaus, G. Dresselhaus, Ph. Avouris. Springer, Germany, (2000).
5. Foss, C.A., In “Nano Particles: Synthesis, Characterization and Application” Eds: D.L. Feldhiem, C. A. Foss, *Maccel Dekker*, New York, (2002).
6. Shen, T.D.; Koch, C.C.; Tsui, T.Y.; Pharr, G.M., “On the elastic moduli of nanocrystalline Fe, Cu, Ni and Cu-Ni alloys prepared by mechanical milling/alloying” *J. Mater. Res*. **10**, 2892-2896 (1995).
7. Cao, H.S.; Hunsinger, J.J.; Elkedim, O., “Determination of elastic modulus of nanocrystalline iron and titanium by means of acoustic microscopy” *Scripta. Mater*. **46**, 55-60 (2002).
8. Kim, H.S.; Bush, M.B., “The effects of grain size and porosity on the elastic modulus of nanocrystalline materials” *Nanostruc. Matls*. **11,** 361-367 (1999).

9. Sanders, P.G.; Eastman, J.A.; Weertman, J.R., "Elastic and tensile behavior of nanocrystalline copper and palladium" *Acta. Mater.* **45**, 4019-4025 (1997).

10. Van Swygenhoven, H.; Caro, A., "Plastic behavior of nanophase Ni: A molecular dynamics computer simulation" *Appl. Phys. Lett.* **71**,1652-1656 (1997).

11. Siegel, R.W.; Fougere, G.E., "Mechanical properties of nanophase metals" *Nanostruc. Matls.* **6**, 205-216 (1995).

12. Konstantinidis, D.A.; Aifantis, E.C., "On the 'anomalous' hardness of nanocrystalline materials" *Nanostruc. Matls.* **10**, 1111-1118 (1998).

13. Koch, C.C.; Morish, D.G.; Lu, K.; Inoue, A., "Ductility of nanostructured materials" *MRS. Bull.* **24**, 54-59, (1999).

14. Bohn, R.; Haubold, T.; Birringer, R.; Gleiter, H., "Nanocrystalline intermetallic compounds-An approach to ductility?" *Scripta Metall. Mater*. **25**, 811-816 (1991).

15. Wang, Y.; Chen, M.; Zhou, F.; Ma, E., "High tensile ductility in a nanostructured metal" *Nature*, **419**, 912-915 (2002).

16. Champion, Y.; Langlois, C.; Guérin-Mailly, S.; Langlois, P.; Bonnentien, J.; Hÿtch, M.J., "Near-perfect elestoplasticity in pure nanocrystalline copper" *Science* **300,** 310-311 (2003).

17. Srivastava, D., In "Carbon Nanotubes: Science and Application" Ed. M. Meyyappan, *CRC Press*, New York, 25 (2005).

18. Bera, D.; Patil, S.; Scammon, K.; Seal, S., "Diffusion limited growth of FTO nanofilm coated tin fractals" *J. Mater. Res.* (submitted).

19. Bera, D.; Kuiry, S.C.; Patil, S.; Seal, S., "Palladium nanoparticles arrays using template-assisted electrodeposition" *Appl. Phys. Letts.* **82**, 3089-3091 (2003).

20. Bera, D.; Kuiry, S.C.; Rahman, Z.; Seal, S., "Template-assisted deposition of palladium nanoarrays: preparation. Microscopic and scectroscopic studies" *J. Electrochem. Soc.* (accepted).
21. Bera, D.; Kuiry, S.C.; Seal, S., "Synthesis of nanostructured materials using template-assisted electrodeposition" *JOM* **56**, 49-53 (2004).
22. Bera, D.; Kuiry, S.C.; Seal, S., "Kinetics and growth mechanism of electrodeposited palladium nanocrystallites" *J. Phys. Chem. B* **108**, 556-562 (2004).
23. Bera, D.; Seal, S.; Azad, Wang; C.M.; Shutthanandan, V.; McCready, D.E.; Saraf, L.; Engelhard, M.; Thevuthasan, T., "Growth and Characterization of Highly Oriented Pure and Gd_2O_3 doped CeO_2(111) on ZrO_2(111)/Al_2O_3(0001) system" (under preparation).
24. Bera, D. Seal. S. "Preparation of nanosized Ni-Fe alloys using microemulsion" (Unpublished).
25. Bera,D.; Anal, A.; Rao, B.T.; Mohan, T.R.R., "Synthesis of 45S5 Bioglass" *Proc. 28th Inter. Annual Meeting on Powder metallurgy, Powder Metallurgy Association of India*, New Delhi, (2002).
26. Kroto, H.W.; Heath, J.R.; O'Brien, S.C.; Curl, R.F.; Smally, R.E., "C60: Buckminsterfullerene" *Nature* **318**, 162-163 (1985).
27. Ugarte, D., "How to fill or empty a graphitic onion", *Chem. Phys. Lett.* **209**, 99-103 (1993).
28. Ugarte, D., "Curling and closure of graphitic networks under electric beam" *Nature* **359**, 707-709 (1992).
29. Sano, N.; Wang, H.; Chhowalla, M.; Alexandrou, I.; Amaratunga, G.A.J., "Synthesis of carbon 'onions' in water" *Nature* **414**, 506-507 (2001).

30. Sano, N.; Wang, H.; Alexandrov, I.; Chhowalla, M.; Teo, K.B.K.; Amaratunga, G.A.; Iimura, K., "Properties of Carbon Onions Produced by an Arc Discharge in Water" *J. Appl. Phys.* **92**, 2783-2788, (2002).

31. Iijima, S., "Helical microtubules of graphitic carbon" *Nature* **354**, 56-59 (1991).

32. Krätschmer, W.; Lamb, L.D.; Fostiropoulos, K.; Huffman, D. R., "Solid C60: a new form of carbon" *Nature* **347**, 354-358 (1990).

33. Harris, P.J., In "*Carbon Nanotubes and Related Structures*" *Cambridge University Press*, Cambridge, UK, (1999).

34. Sano. N.; Nakano, J.; Kanki, T. "Synthesis of single walled carbon nanotubes with nanohorns by arc in liquid nitrogen" *Carbon* **42**, 667-691(2004).

35. Davis, W.R.; Slawson, R.J.; Rigby, G.R., "An unusual form of carbon" *Nature* **171**, 756 (1953).

36. Bacon, R., "Growth, structure, and properties of graphite whiskers" *J. App. Phys.* **31**, 283-290 (1960).

37. Tibbetts, G.G., "Why are carbon filaments tubular" *J. Cryst. Growth* **66**, 632-638 (1984).

38. Speck. J.S.; Endo, M.; Dresselhaus, M.S., "Structure and intercalation of thin benzene derived carbon fibers" *J. Cryst. Growth.* **94**, 834-848 (1989).

39. Iijima, S.; Ichihashi, T., "Single-shell carbon nanotubes of 1nm diameter" *Nature*, **363**, 603-605 (1993).

40. Saito, R., Dresselhaus, G.; Dresselhaus, M.S., In "Physical properties of carbon nanotubes". *Imperial College Press*, London, 35. (1998).

41. Charlier, J.-C.; Michenaud, J.-P., "Energetics of multilayered carbon tubules" *Phys. Rev. Letts.* **70**, 1858-1861 (1993).

42. Ajayan, P.M. “Nanotubes from carbon” *Chem. Rev.* **99**, 1787-1799 (1999).

43. Baxendale, M. “The physics and applications of carbon nanotubes” *J. Mater. Sc.: Mater. Electro.* **14**, 657-659 (2003).

44. Tans, S.J.; Verschueren, A.R.M.; Dekker, C., “Room-temperature transistor based on a single carbon nanotube” *Nature* **393**, 49-52, (1998).

45. Collins, P. G.; Zettle, A.; Bando, H.; Thess, A.; Smalley, R.E., “Nanotubes nanodevices” *Science* **278**, 100-103 (1997).

46. Han, J., In “Carbon Nanotubes: Science and Application” Ed. M. Meyyappan, *CRC Press*, New York, (2005).

47. Pal, A.K.; Roy, R.K.; Mandal, S.K.; Gupta, S.; Deb, B., “Electrodeposited carbon nanotubes thin films” *Thin Solid Films* **476**, 288-294 (2005).

48. Tsang, S.C.; Chen, Y.K.; Harris, P.J.F.; Green, M.L.H., “A Simple chemical method of opening and filling carbon nanotubes” *Nature* **372**, 159-162 (2002).

49. Ajayan, P.M.; Iijima, S., “Capillarity-induced filling of carbon nanotubes” *Nature* **361**, 333-335 (1993).

50. Seraphin, S.; Zhou, D.; Jiao, J.; Withers, J.C.; Loutfy, R., “Yttrium carbide in nanotubes” *Nature*, **362**, 503 (1993).

51. Ajayan, P.M.; Colliex, C.; Lambert, J.M.; Bernier, P.; Barbedette, L.; Tence, M.; Stephan, O., “Growth of manganese filled carbon nanofibers in the vapor phase” *Phys. Rev. Lett.* **72**, 1722-1726 (1994).

52. Ang, L.-M.; Hor, T.S.A.; Xu, G.-Q.; Tung, C.-h.; Zhao, S.; Wang, J.L.S., “Electroless plating of metals onto carbon nanotubes activated by a single-step activation method” *Chem. Mater*. **11,** 2115-2118 (1999).

53. Ye, X.R.; Lin, Y.; Wai, C.M., "Decorating catalytic palladium nanoparticles on carbon nanotubes in supercritical carbon dioxide" *Chem. Comm.*, **5**, 642-643 (2003).

54. Liu, Z.; Lin, X.; J.; Lee, Y.; Zhang, W.; Han, M.; Gan, L.M., "Preparation and characterization of platinum-based electrocatalysts on multiwalled carbon nanotubes for proton exchange membrane fuel cells" *Langmuir* **18**, 4054-4058 (2002).

55. Lordi, V.; Yao, N.; Wei, J., "Method for supporting platinum on single-walled carbon nanotubes for a selective hydrogenation catalyst" *Chem. Mater*. **13,** 733-737 (2001).

56. Planeix, J. M; Coustel, N.; Coq, B.; Brotons, V.; Kumbhar, P. S.; Dutartre, R.; Geneste, P.; Bernier, P.; Ajayan, P. M., "Application of carbon nanotubes as supports in heterogeneous catalysis" *J. Am. Chem. Soc.* **116,** 7935-7936 (1994).

57. Che, G.; Lakshmi, B.B.; Martin, C.R.; Fisher, E.R., "Metal-nanocluster-filled carbon nanotubes: Catalytic properties and possible applications in electrochemical energy storage and production" *Langmuir* **15,** 750-758 (1999).

58. Dong, X.; Zhang, H.-B.; Lin, G.-D.; Yuan, Y. -Z.; Tsai, K.R., "Highly active CNT-promoted Cu-ZnO-Al_2O_3 catalyst for methanol synthesis from $H_2/CO/CO_2$" *Catal. Letts.*, **85**, 237-246 (2003).

59. Luo, J.Z.; Gao, L.Z.; Leung, Y.L.; Au, C.T., "The decomposition of NO on CNTs and 1 *wt%* Rh/CNTs" *Catal. Letts.* **66**, 91-97 (2000).

60. Hsin, Y.L.; Hwang, K.C.; Chen, F.; Kai, J., "Production and In-situ metal filling of Carbon Nanotube in Water" *Adv. Mater.* **13**, 830-833 (2001).

61. 57. Gao, Y.; Liu, J.; Shi, M.; Elder, S.H.; Virden, J.W., "Dense arrays of well-alligned carbon nanotubes completely filled with single crystalline titania carbide wires on titanium substrate" *Appl. Phys. Lett.* **74**, 3642-3646 (1999).

62. Zhang, G.Y.; Wang, E.G., "Cu-filled carbon nanotubes by simultaneous plasma assiated copper incorporation" *Appl. Phys. Lett.* **82**, 1926-1928 (2003).

63. Tamponnet, C., "Life support systems for lunar missons", *Advances in Space Research,* **18**, 103-110 (1996).

64. Technical Panel of Earth Satellite Program, "Research in outer space" *Science* **127**, 793-802 (1958).

65. Sabatier, P.; Senderens, J.B., "Hydrogénation directe des oxides du carbone en présence de divers métaux divisés" *Comptes Rendus Hebdomadaires Des Seances De L'Academie Des Sciences* **134**, 689-691 (1902).

66. Arlow, M.; Traxler, G., "CO_2 Processing and O_2 Reclamation System Selection Process for Future European Space Programmes" *SAE Technical Paper Series No. 891548*, Warrendale, PA, Society of Automotive Engineers, (1989).

67. Luo, J.Z.; Gao, L.Z.; Leung, Y.L.; Au, C.T., "The Decomposition of NO on CNTs and 1 wt% Rh/CNTs" *Catal. Letts.* **66**, 91-97 (2000).

68. Giordano, R.; Serp, P.; Kalck, P.; Kihn, Y.; Schreiber, J.; Marhic, C.; Duvail, J., "Preparation of rhodium catalysts supported on carbon nanotubes by a surface mediated organometallic reaction" *Euro. J. Inorg. Chem.* **2003**, 610-617 (2003).

69. Serp, P.; Corrias, M.; Kalck, P., "Carbon nanotubes and nanofibers incatalysis" *Appl. Catal. A* **253**, 337-358, (2003).

70. Liu, Z.; Xu, Z.; Yuan Z.; Lu, D.; Chen, W.; Zhou, W., "Cyclohexanol dehydrogenation over Co/carbon nanotube catalysts and the effect of promoter K on performance" *Catal. Letts.* **72**, 203-206 (2001).

71. Iwamamoto, M.; Yahiro, H., “Novel catalytic decomposition and reduction of NO” *Catal. Today*, **22**, 5-18 (1994).

72. Winter, E.R.S., “The catalytic decomposition of nitric oxide by metallic oxides” *J. Catal.* **22**, 158-170 (1971).

73. Noronha, F.B.; Baldanza, M.A.S.; Monteiro, R. S.; Aranda, D.A.G.; Ordine, A.; Schmal, M., “The nature of metal oxide on adsorptive and catalytic properties of Pd/MeO_x/Al_2O_3 catalysts” *Appl. Catal. A* **210***,* 275-286 (2001).

74. Rodríguez-Reinoso, F. “The role of carbon materials in heterogeneous catalysis” *Carbon* **36**, 159-175 (1998).

75. Loiseau, A.; Demoncy, N.; Stéphan, O.; Colliex, C.; Pascard, H., In “*Science and application of nanotubes”*, Ed: Tománek and Enbody, *Kluwer Academic/ Plenum Publishers*, New York, (2000).

76. Mao, A.G.; Sinnott, S.B., “Molecular dynamics simulations of the filling and decorating of carbon nanotubes” *Nanotechnology* **10**, 273-277 (1999).

77. Muradov, N., “Catalysis of methane decomposition over elemental carbon” *Catal. Commun.* **2**, 89-94 (2001).

78. Mestl, G.; Maksimova, N.I.; Keller, N.; Roddatis, V.V.; Schlogl, R., “Carbon nanofilaments in heterogeneous catalysis: An industrial application for new carbon materials” *Ang. Chem. Internation. Ed. Eng.* **40***,* 2066-2068 (2001).

79. Dillon, A.C.; Jones, K.M.; Bekkedahl, T.A.; Kiang, C.H.; Bethune, D.S.; Heben, M.J., “Storage of hydrogen in single-walled carbon nanotubes” *Nature* **386**, 377-379 (1997).

80. Oku, T.; Narita, I., “Calculation of H_2 gas storage for boron nitride and carbon nanotubes studied from the cluster calculation” *Physica B* **323**, 216-218, (2002).

81. Dravid, V.P.; Lin, X.; Wang, Y.; Wang, X.K.; Yee, A.; Ketterson, J.B.; Chang, R.P.H., "Buckytubes and derivaties: their growth and implications for buckyball formation" *Science* **259**, 1601-1604 (1993).

82. Chen, P.; Wu, X.; Lin, J.; Tan., K.L., "High H_2 uptake by alkali-doped carbon nanotubes under ambient pressure and moderate temperatures" *Science*, **285**, 91-96 (1999).

83. Pinkerton, F.E.; Wicke, B.G.; Olk, C.H.; Tibbetts, G.G.; Meisner, G.P.; Meyer, M.S.; Herbst, J.F., "Thermogravimetric measurement of hydrogen absorption in alkali-modified carbon materials" *J. Phys. Chem.B* **104**, 9460-9467 (2000).

84. Ralph, T.Y., "Hydrogen storage by alkali-doped carbon nanotubes–revisited" *Carbon* **38**, 623-626 (2000).

85. Seung, M.L., "Hydrogen adsorption and storage in carbon nanotubes" *Syn. Metals* **113**, 209-216 (2000).

86. Shimoda, H., "Lithium intercalation into opened single-wall carbon nanotubes: storage capacity and electronic properties" *Phys. Rev. Lett.*, **88**, 015502[1]-[4] (2002).

87. Salomons, E., "On the lattice gas description of hydrogen in palladium: a molecular dynamics study" *J. Phys.:Condens. Matter* **2**, 845-855 (1990).

88. Graham, T., "On the absorption and dialytic separation of gases by colloid septa" *Phil. Mag.* **S 4**, **32**, 501-531 (1866).

89. Heinze, S.; Tersoff, J.; Martel, R. Derycke, V.; Appenzeller, J.; Avouris, P., "Carbon Nanotubes as Schottky Barrier Transistors" *Phys. Rev. Lett.* **89**, 106801[1]-[4] (2002).

90. Appenzeller, J.; Knoch, J.; Derycke, V.; Martel, R.; Wind, S. Avouris, Ph., "Field-Modulated Carrier Transport in Carbon Nanotube Transistors" *Phys. Rev. Lett.*, **89**, 126801[1]-[4] (2002).

91. Jamey, A.; Guo, J.; Wang, Q.; Lundstrom, M.; Dai, H., "Ballistic carbon nanotube field-effect transistors" *Nature* **424**, 654-657 (2003).

92. Ishigami, M.; Cumings, J.; Zettl, A.; Chen, S., "A Simple Method for the Continuous Production of Carbon Nanotubes" *Chem. Phys. Letts.* **319**, 457-459 (2000).

93. Li, X.; Zhu, H.; Jiang, B.; Ding, J.; Cailu, X.; Wu, D., "High-yield sythesis of multi-walled carbon nanotubes by water-protected arc discharge method" *Carbon* **41**, 1664 (2003).

94. Biró, L.P.; Horváth, Z.E.; Szalmás, L.; Kertész, K.; Wéber, F.; Juhász, G.; Radnóczi, G.; Gyulai, J., "Continuous Carbon Nanotube Production in Underwater AC Electric Arc" *Chem. Phys. Letts.* **372**, 399-402 (2003).

95. Sano, N.; Wang, H.; Chhowalla, M.; Alexandrou, I.; Amaratunga, G.A.J.; Naito, M.; Kanki, T., "Fabrication of inorganic molybdenum disulfide fullerenes by arc in water" *Chem. Phys. Lett.* **368**, 331-337 (2003).

96. Antisari, M.V.; Marazzi, R.; Krsmanovic, R., "Synthesis of multiwall carbon mamotubes by electric arc discharge in liqud environments" *Carbon* **41**, 2393-2401 (2003).

97. Lange, H.; Sioda, M.; Huczko, A.; Zhu, Y.Q.; Kroto, H.W.; Walton, D.R.M., "Nanocarbon production by arc discharge in water" *Carbon* **41**, 1617 (2003).

98. Qiu, J.; Li, Y.; Wang, Y.; Zhao, Z.; Zhou, Y.; Wang, Y., "Synthesis of carbon-encapsulated nickel nanocrystals by arc-discharge of coal-based carbons in water" *Fuel* **83**, 615-617 (2004).

99. Bera, D.; Kuiry, S.C.; McCutchen, M.; Kruize, A.; Heinrich, H.; Meyyappan, M.; Seal, S., "In-situ synthesis of palladium nanoparticles-filled carbon nanotubes using arc-discharge in solution" *Chem. Phys. Lett.* **386** 364-368, (2004).

100. Bera, D.; Kuiry, S.C., McCutchen, M.; Seal, S.; Heinrich, H.; Slane, G.D., "In situ synthesis of carbon nanotubes decorated with palladium nanoparticles using arc-discharge in solution method" *J. Appl. Phys.* **96**, 5152-5157 (2004).
101. Bera, D.; Brinley, E.; Kuiry, McCutten, M.; S.C.; Seal, S.; Heinrich, H.; Kabes, B., "Optoelectronically automated system for cabon nanotubes synthesis via arc-discharge in solution" *Rev. Sci. Instrum.* **76**, 033903-033909 (2005).
102. Bera, D.; Johnston, G.; Seal, S., "Parametric study for synthesis of carbon nanotubes using arc-discharge in solution" (*in preparation*).
103. Zhu, H.W.; Li, X.S.; Jiang, B.; Xu, C.L.; Zhu, Y.F.; Wu, D.H.; Chen, X.H., "Formation of carbon nanotubes in water by the electric-arc technique" *Chem. Phys. Lett.* **366**, 664-669 (2002).
104. Sano, N.; Naito, M.; Chhowalla, M.; Kikuchi, T.; Matsuda, S.; Iimura, K.; Wang. H.; Kanki, T.; Amartunga, G.A.J. "Pressure effects on nanotubes formation using the submerged arc in water method" *Chem. Phys. Letts*. **378**, 29-34 (2003).
105. Sano, N.; Nakano, J.; Kanki, T., "Synthesis of single-walled carbon nanotubes with nanohorns by arc in liquid nitrogen" *Carbon* **42**, 667-691 (2004).
106. Montoro, L.A.; Lofrano, R.C.Z.; Rosolen, J.M., "Synthesis of single-walled and multi-walled carbon nanotubes by arc-water method" *Carbon* **43**, 200-203 (2005).
107. de Heer, W. A., "Nanotubes and the pursuit of applications" *MRS Bull.* **29**, 281-285 (2004).
108. Liu, J.; Fan, S.; Dai, H., "Recent advances in methods of forming carbon nanotubes" *MRS Bull.* **29**, 244-249 (2004).

109. Lange, H.; Baranowski, P.; Huczko, A.; Byszewski, P., "An optoelectronic control of arc gap during formation of fullerenes and carbon nanotubes" *Rev. Sci. Instrum.* **68,** 3723-3727 (1997).

110. Barr, T.L.; Seal, S., "Nature of the use of adventitious carbon as a bonding energy standard" *J. Vacuum Sci. Technol.* ***A13***, 1239-1246 (1995).

111. Brunauer, S.; Emmett, P.H.; Teller. E., "Adsorption of gases in multimolecular layers" *J. Amer. Chem. Soc.* **60**, 309-319 (1930).

112. Mackeown, S.S., "The cathode drop in an electric arc" *Phys. Rev.* **34**, 611-614 (1929).

113. Waldoff, E.I.; Waas, A.M.; Friedmann, P.P.; Keider M., "Characterization of carbon nanotubes produced by arc discharge: Effect of the background pressure" *J. Appl. Phys.* **95**, 2749-2754 (2004).

114. Zhang, G.; Jiang, X.; Wang, E., "Tubular graphitic cones" *Science*, **300**, 472-474 (2003)

115. Saito, Y.; Yoshikawa, T.; Bandow, S.; Tomita, M.; Hayashi, T., "Interlayer spacing in carbon nanotubes" *Phy. Rev. B* **48**, 1907-1920 (1993).

116. Qin, L.-C., In "Electron microscopy of nanotubes" Ed. Wang, Z.; Hui, C., *Kluwer Academic Pub.* Boston, (2003).

117. Iijima, S.; Ichihashi, T.; Ando, Y., "Pentagons, heptagons and negative curvature in graphite microtubules growth" *Nature* **356**, 776-778 (1992).

118. Alexandrou, I.; Wang, H.; Sano, N.; Amaratunga, G.A.J., "Structure of carbon onions and nanotubes formed by arc in liquids" *J. Chem. Phys.* **120**, 1055-1058 (2004).

119. Cowley, J.M., In "Electron microscopy of nanotubes", Ed. Wang, Z.L.; Hui, C. *Kluwer Academic Pub.* Boston, 73-93 (2003).

120. Chen, P.; Wu, X.; Sun, X.; Lin, J.; Ji, W.; Tan, K.L. “Electronic structure and optical limiting behavior of carbon nanotubes” *Phy. Rev. Letts*. **82**, 2548-2551 (1999).

121. Tsang, S.C.; Harris, P.J.F.; Green, M.L.H., “Thinning and opening of carbon nanotubes by oxidation using carbon dioxide” *Nature* **362**, 520-522 (1993).

122. Sawada, S.; Hamada, N., “Energetics of carbon nanorubes” *Solid State Commun.* **83**, 917-919 (1992).

123. Ebbesen, T.W.; Ajayan, P.M., “Large scale synthesis of carbon nanotubes” *Nature* **358**, 220-222, (1992).

124. Yasuda, A.; Kawase, N.; Banhart, F.; Mizutani, W.; Shimizu, T.; Tokumoto, H., “Graphitization mechanism during the carbon-nanotube formation based on the in-situ HRTEM observation**”** *J. Phys. Chem. B.* **106**, 1849-1852 (2002).

125. Motojima, S.; Kawaguchi, M.; Nozaki, K.; Iwanaga, H., “Preparation of coiled fibers by catalytic pyrolysis of acetone and its morphology and extension characteristics” *Carbon* **29**, 379-385 (1991).

126. Mickelson, E.T., “Formation of single-wall carbon nanotubes” *Chem. Phys. Lett.* **296**, 188-194 (1998).

127. Luo, C.; Zhang, Y.; Wang, Y., “Palladium nanoparticles in poly9ethyleneglycol): the efficient recyclable catalyst for Heck reaction” *J. Molec. Catal. A* **229,** 7-12 (2005).

128. Moulder, J.F.; Stickle, W.F.; Sobol, P.E.; Bomben, K.D. In “Handbook of X-ray Photoelectron Spectroscopy” Ed. Chastain J., Physical Electronics Division, *Perkin-Elmer Corporation*, Eden Prairie, Minnesota, (1992).

129. Sundaram, A.K.; Sandell, E.B., “Chloro complexes of palladium (II) solution” *J. Am. Chem. Soc.* **77**, (855-857) 1955.

130. Bell, W.E.; Merten, U.; Tagami, M., "The palladium-chlorine system at high temperature" *J. Phys. Chem.* **65**, 510-517, (1961).

131. Krustinsons, J., "Über die thermische Dissoziation einiger Chloride" *Z. Elektrochem.* **44**, 537-539 (1938).

132. Saha, M.N., "Ionization in the chromospere" *Phil. M*ag. **S6**, **40**, 472-488 (1920).

133. Sellers, H., "On modeling chemisorption processes with metal cluster systems: H, O, N and S on the Pd(111) plane" *Chem. Phys. Letts.* **170**, 5-12 (1990).